Doctoral Dissertation

博士論文

Non-sphericities and alignments of clusters and central galaxies from cosmological hydrodynamical simulation: theoretical predictions and observational comparison

(宇宙流体シミュレーションを用いた銀河団・中心銀河の非球対称性と角度相関：理論予言および観測的検証)

A Dissertation Submitted for the Degree of Doctor of Philosophy

December 2019

令和元年 12 月 博士（理学）申請

Department of Physics, Graduate School of Science

The University of Tokyo

東京大学大学院理学系研究科物理学専攻

Taizo Okabe

岡部　泰三

Abstract

The standard cosmological model with cosmological constant Λ and cold dark matter model (the ΛCDM model), explains various observations such as the cosmic microwave background radiation, baryon acoustic oscillations, and relation between magnitude and redshift of type Ia supernovae, and its model parameters are determined with very good accuracy. The ΛCDM model under this parameter set explains well the observations at large scales, but there are many problems at small scales. However, these problems may be caused by lack of understanding of baryon physics at small scales, and it is too early to conclude that these observations are inconsistent with the ΛCDM model.

In this thesis, we focus on galaxy clusters, which are in the intermediate scales. Galaxy clusters are the largest self gravitational bounding objects in the universe and they retain the initial conditions of the primordial density fluctuations because their dynamical time scale is comparable to the age of the universe. Especially, we investigate the non-sphericities of galaxy clusters which are worth studying because they contain important information for both cosmology and astrophysics such as the initial conditions of the universe, cosmological parameters, and structure and galaxy formation histories. Furthermore, their characteristic quantities, ellipticities and orientations, can be used to validate the ΛCDM model complementary to other probes.

In particular, we focus on the correlation of ellipticities and orientations between galaxy clusters and their central galaxies (CGs). Since the CG has been formed by repeated mergers as well as galaxy clusters, the examination of these correlations will lead us to understand the structure formation history at different scales. Furthermore, since the correlation of the non-sphericity indirectly depends on cosmological parameters through the structure formation history, it can be used to validate the ΛCDM model. We conduct comprehensive study on three topics from both theoretical and observational perspectives, and obtain following results.

- We identify galaxy clusters and CGs formed in the latest cosmological hydrodynamical simulation incorporating baryon physics, the Horizon-AGN simulation, and make reliable theoretical predictions of the ΛCDM model. In particular, we measure the non-sphericities of galaxy clusters using mock observations in visible light, X-ray, and radio wavelength, and compare their orientations with those of CGs. According to the theoretical predictions of the ΛCDM model, orientations of galaxy clusters and those of their CGs are well aligned with each other and these results are marginally consistent with observations.

- We provide a new measurement of non-sphericities of 45 DM haloes in galaxy clusters using strong lensing for a large sample obtained by combining 3 different surveys selected based on the intensity of gravitational lensing, X-ray, and radio signals. We also measure non-sphericities of their brightest cluster galaxies (BCGs) from high angular resolution images taken by the Hubble Space Telescope. Our new observations show that galaxy clusters are on average more elongated than BCGs. On the other hand, we obtain theoretical predictions of the ΛCDM model from the Horizon simulation that ellipticity values of DM haloes and CGs are almost equal on average from galactic to cluster scales, but the slightly larger the mass, the greater the ellipticity differences such that DM haloes are elongated. The results implies that the discrepancy between theoretical predictions and the observations can be explained simply by the mass difference. In either case, our measurement gives a new observational constraint on theoretical predictions.
- We investigate the mechanism of alignment by following mass accretions and orientation changes of DM haloes and their CGs for *individual* galaxy clusters in the Horizon-AGN simulation. Even in the early stage of the universe, $t = 1.5$ Gyr, orientations of DM haloes and their CGs are weakly aligned statistically, and the alignments at each epoch become tighter with time. However, orientations of both DM haloes and CGs have significantly changed over the cosmic time. The changes of their orientations are mainly caused by mass accretion episodes along filaments whose directions are computed from the tidal fields, and their orientations are finally aligned with the filament directions.

In the future, our theoretical predictions will be validated with further accuracy thanks to large surveys such as the *Subaru* Hyper Suprime-Cam (HSC) and the Large Synoptic Survey Telescope (LSST). In particular, by exploring the alignments between orientations of galaxy clusters and those of their BCGs at higher redshifts beyond $z = 1$, the evolution scenario predicted by ΛCDM will be observationally tested. Furthermore, results of updated simulations will allow us to adopt non-sphericities of galaxy clusters to investigate various physics such as the structure formation history, AGN feedback, gravitational theories, and dark matter models. Our study in this thesis is expected to serve as a guideline for such future researches in terms of connecting observations and theories.

Contents

Chapter 1

Introduction

Galaxy clusters are the largest self-gravitational bounding objects in the universe and they are mainly composed of dark matter, hot gas, and $100-1000$ galaxies. The most energetic phenomena in the universe occur in galaxy clusters such as galaxy mergers accompanied with violent star formation and feedback from active galactic nuclei (AGN). In addition, they may retain the initial conditions of density fluctuations because their dynamical time scales are comparable to the age of the universe. At the same time, since their evolution is sensitive to cosmological parameters through the expansion of the universe, they have played a complementary role to other probes in validating the standard cosmological model, so-called the ΛCDM model (cosmological constant Λ + cold dark matter model). From these points of view, galaxy clusters are unique objects located at the crossroads of astrophysics and cosmology, and their evolution and properties may help us understand the structure formation in the universe.

Non-sphericity of galaxy clusters is an important concept that contains entangled information related to the initial conditions of the universe, structure and galaxy formation histories, and cosmological parameters. The non-sphericity is already imprinted in the early primordial fluctuations and galaxy clusters, which are young objects growing by repeated mergers, are naturally expected to have distorted shapes reflecting the direction of the latest merger. In addition, the non-sphericity of galaxy clusters indirectly depends on cosmological parameters through their formation epochs, and also contains information of past baryon activities within them such as AGN feedback and star formation. Furthermore, the non-sphericity itself can be used to test the ΛCDM model complementarily to previous probes.

In particular, in this thesis we focus on correlations of ellipticity and alignment between galaxy clusters and their central galaxies which are giant luminous galaxies at the cluster center. Since the central galaxies as well as galaxy clusters have been formed by repeated mergers, merger history of galaxy clusters at different scales may be understood by examining correlations between their orientations. Constraints on structure formation history can also be obtained by examining correlations of ellipticities between central part which is generally formed at early epoch and outer part which is still growing. Furthermore, since the correlations depend on cosmological parameters throughout their formation history, the complementary test of the ΛCDM model can be made by examining them.

The alignment of orientations of galaxy clusters and their central galaxies has been observed for a long time (e.g. Sastry, 1968; Binggeli, 1982), and more recently West *et al.* (2017) showed that the alignment already existed about 10 billion years ago. Theoretically, cosmological hydrodynamical simulations incorporating baryon physics are essential to study detailed properties of central galaxies. While such simulations have been difficult due to lack of understanding of baryon physics and computational limitations, only recently the reliable simulations which are consistent with various observations become available. In fact, some papers investigate the alignment between galaxy clusters and their central galaxies by using such simulations (Dong *et al.*, 2014; Tenneti *et al.*, 2014; Chisari *et al.*, 2017). However they focus on cosmological applications of the alignments and thus do not investigate the evolution of ellipticity and the alignments of galaxy clusters to understand structure formation history.

Observationally, most studies measured non-sphericity of galaxy clusters from member galaxy distributions and X-ray surface brightness (e.g. Niederste-Ostholt *et al.*, 2010; Kawahara, 2010) but assumptions in gas state or the relation between light and mass distributions are essential. Since about 80% of the mass of galaxy clusters is contributed by dark matter, the gravitational lensing should be used to directly measure their shapes. Although some previous studies measured the non-sphericity using gravitational lensing (e.g. Richard *et al.*, 2010; Oguri *et al.*, 2010; Shin *et al.*, 2018), their results are limited by small sample sizes, heterogeneities, and measurement uncertainties.

In response to the above problems of previous studies, we will conduct a comprehensive study about non-sphericity of galaxy clusters and central galaxies by approaching both theoretically and observationally. In the theoretical aspect, we will try to understand the structure formation history in the ΛCDM universe as well as the construction of theoretical predictions by carrying out mock observations of galaxy clusters in the latest cosmological hydrodynamical simulation. We will also provide a new observational constraint on the non-sphericity of galaxy clusters and validate the consistency of the ΛCDM model through comparison of these observations of the real Universe with the mock observations of the ΛCDM universe.

We address the remaining issues as follows. First, chapter 2 summarizes what has been studied in previous researches and what remains to be done. In chapter 3, we use the latest cosmological hydrodynamical simulation to develop theoretical predictions, in particular focusing on the correlation between orientations of galaxy clusters and those of central galaxies. The consistency of the ΛCDM model is briefly validated by comparing with observations. Next, in chapter 4, we provide a new observational constraint by measuring the non-sphericity using strong lensing for a cluster sample obtained by combining three different surveys. At the same time, the consistency with the ΛCDM model is validated by comparing the observed results with theoretical predictions of the cosmological hydrodynamical simulation. In chapter 5, we explore the origin of the alignment by examining mass accretions and orientation changes for each galaxy cluster. Finally, chapter 6 summarizes results and provides future prospects of this thesis.

Throughout this thesis, we adopt the cosmological parameters based on the seven-

year Wilkinson Microwave Anisotropy Probe (Komatsu *et al.*, 2011); $\Omega_{\mathrm{m},0} = 0.272$ (total matter density at present day), $\Omega_{\Lambda,0} = 0.728$ (dark energy density at the present time), $\Omega_{\mathrm{b},0} = 0.045$ (baryon density at present time), $\sigma_8 = 0.81$ (amplitude of the power spectrum of density fluctuations that are averaged on spheres of $8h^{-1}$ Mpc radius at present time), $\mathrm{H}_0 = 70.4$ km/s/Mpc (Hubble constant), and $n_s = 0.967$ (the power-law index of the primordial power spectrum).

Chapter 2

Non-sphericities of galaxy clusters from previous studies

2.1 Non-sphericities of galaxy clusters: observational measurements

This section reviews observational studies of the non-sphericity of galaxy clusters. Since galaxy clusters consist of three major components: stars, dark matter (DM), and gas, the following subsections summarize how the ellipticity of each component has been measured observationally. We also note how the observational evidence that orientations of galaxy clusters are aligned with those of their central galaxies (CGs) has been derived.

2.1.1 Member galaxy distributions

Galaxy clusters generally have member galaxies about 100 to more than 1000 and historically they are defined as the dense region of galaxies (e.g. Abell, 1958). Although it is difficult to identify the member galaxies without spectroscopic data due to the projection effect of background/foreground galaxies, the member galaxies can be identified by combining multi-band images. Member galaxies have characteristic color of red sequence, which is a specific region in color-magnitude diagram where passively evolved early type galaxies are located (e.g. Hogg *et al.*, 2004; Croton *et al.*, 2005). Recently, many galaxy clusters are identified with this characteristic color of the members (e.g. Koester *et al.*, 2007; Oguri, 2014; Oguri *et al.*, 2018). Since galaxies evolve in the potential of DM haloes, distributions of the member galaxies are expected to trace the DM distribution of their host clusters.

Sastry (1968) measured ellipticities of 9 galaxy clusters from member galaxy distributions and reported alignments between position angles of brightest cluster galaxies (BCGs) and those of their host clusters for the first time. Ellipticities and position angels of the distributions were determined basically by using the transparent celluloid such that the numbers in the four quadrants were almost the same by slowly moving and rotating the celluloid. They detected ellipticities larger than 0 for 5 clusters in 9 and found that the

position angles of the clusters with those of their BCGs are well aligned within less than 10°. While they reported ellipticities and alignments between clusters and BCGs, their result was statistically limited due to lack of sample size and methods.

Carter & Metcalfe (1980) measured the position angles and ellipticities from member galaxy distributions for the 22 richest clusters with the number of member galaxies of $100 - 3000$ by diagonalizing the inertia tensor of the member galaxy distribution defined as,

$$I_{\mathrm{mem},\alpha\beta} \equiv \sum_{i=1}^{N_{\mathrm{mem}}} \left[x^{(i)}_{\mathrm{mem},\alpha} - x^{\mathrm{C}}_{\mathrm{mem},\alpha}\right] \left[x^{(i)}_{\mathrm{mem},\beta} - x^{\mathrm{C}}_{\mathrm{mem},\beta}\right] \qquad (\alpha, \beta = 1, 2), \tag{2.1}$$

$$x^{\mathrm{C}}_{\mathrm{mem},\alpha} = \frac{1}{N_{\mathrm{mem}}} \sum_{i=1}^{N_{\mathrm{mem}}} x^{(i)}_{\mathrm{mem},\alpha}, \tag{2.2}$$

where N_{mem} and $x^{(i)}_{\mathrm{mem},\alpha} - x^{\mathrm{C}}_{\mathrm{mem},\alpha}$ are the total number of member galaxies and the projected position vector of the i-th member galaxies particle relative to the centre, $x^{\mathrm{C}}_{\mathrm{mem},\alpha}$. Once the eigen-values λ_1 and λ_2, $(\lambda_1 > \lambda_2)$ were obtained, they defined position angle of the semi-major axis, θ_{mem}, as,

$$\theta_{\mathrm{mem}} = \cot^{-1}\left(-\frac{I_{\mathrm{mem},22} - \lambda_1}{I_{\mathrm{mem},12}}\right) + \frac{\pi}{2}, \tag{2.3}$$

and ellipticities, e_{mem}, as,

$$e_{\mathrm{mem}} = 1 - \sqrt{\frac{\lambda_2}{\lambda_1}}. \tag{2.4}$$

They measured the ellipticities at the scale of $\sqrt{ab} = 1$ Mpc, where a and b denote the semi-major and -minor axes, respectively, and obtained a histogram of ellipticities for 21 clusters and the mean value of $e_{\mathrm{mem}} = 0.44 \pm 0.04$. The alignments between clusters and BCGs were derived for 14 clusters and the mean value was 15°. Carter & Metcalfe (1980) extended Sastry (1968) with relatively large statistics, and motivated a next study by Binggeli (1982).

As a pioneering work of this field, Binggeli (1982) analysed a homogenous and large sample of 44 galaxy clusters to investigate their ellipticities and alignments in detail. Only the 50 brightest member galaxies in each cluster were used to avoid the contamination from non-member galaxies and the simple method to compute ellipticities and position angles is adopted as follows. First, the centre was defined by the arithmetic mean of these galaxies, and then the major axis was computed such that the value of $\sum_{i=1}^{50} b_i$ becomes minimum, where b_i is the perpendicular distance from the major axis of i-th member galaxy. After the major axis was determined, the ellipticity was defined as

$$e_{\mathrm{mem}} = 1 - \sum_{i=1}^{50} b_i / \sum_{i=1}^{50} a_i, \tag{2.5}$$

where a_i is the perpendicular distance from the minor axis. The resulting distribution of ellipticities was peaked around 0.4 and marginally consistent with that of Carter &

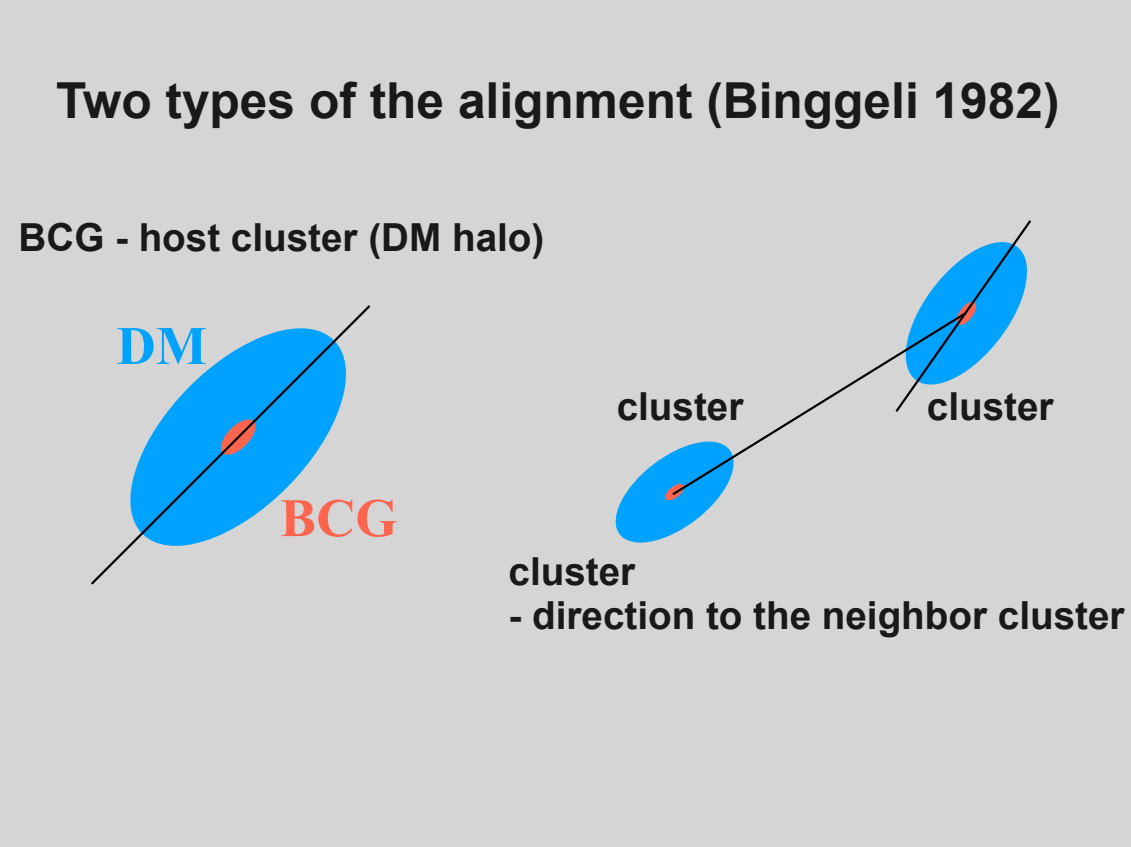

Figure 2.1. Schematic picture of two types of the alignment Binggeli (1982) found. Left: the alignment between orientations of clusters defined through their member galaxy distributions and those of their BCGs. Right: the position angles between major axes of galaxy clusters and the direction to the closest neighboring clusters tend to be correlated than the random distributions.

Metcalfe (1980) indicating that the clusters are more elongated than elliptical galaxies, peaked around 0 (Binggeli, 1980). The position angles computed by the member galaxy distributions relative to those of their BCGs were explored for 39 clusters, and they were well aligned with the mean value of $\sim 30°$. The mean value of the alignment angles was consistent with Carter & Metcalfe (1980).

Binggeli (1982) also reported another type of alignments between the relative orientations of clusters separated within 30 Mpc; the position angles between major axes of galaxy clusters and the direction to the closest neighboring clusters tend to be correlated than the random distributions. Both alignments have been studied further and were confirmed at different redshifts (see Figure 2.1 as a schematic picture of these alignments). After Binggeli (1982), the alignments have been studied in many papers and most of the results basically supported both the alignments (e.g. Argyres *et al.*, 1986; Rhee & Katgert, 1987; Tucker & Peterson, 1988; Lambas *et al.*, 1988; Struble, 1990; Trevese *et al.*, 1992; Plionis, 1994; Fuller *et al.*, 1999; Strazzullo *et al.*, 2005; Panko *et al.*, 2009; Niederste-Ostholt *et al.*, 2010). On the other hand, few studies reported the opposite result; consistent with

random distribution (e.g. Struble & Peebles, 1985).

While the redshifts of cluster sample in Binggeli (1982) were less than 0.1, the alignment between clusters and BCGs have been reported even at relatively high redshift, $z \leq 0.3$ (Kim *et al.*, 2002), $z \sim 0.5$ (Donoso *et al.*, 2006). Furthermore, the alignment was reported not only in galaxy clusters but also in galaxy groups with mass of host DM halo down to $\sim 10^{12}\ h^{-1}M_{\odot}$ (e.g. Wang *et al.*, 2008). Hao *et al.* (2011) investigated comprehensively the dependence of the alignment on the redshift, $z_{\rm photo}$, of $0.1 < z_{\rm photo} < 0.4$, stellar mass of BCGs, $M_{\rm BCG}$, of $10^{11.3}\ M_{\odot} < M_{\rm BCG} < 10^{11.9}\ M_{\odot}$, and richness of host galaxy clusters, $N_{\rm rich}$, of $20 < N_{\rm rich} < 80$. They found that the alignment becomes stronger as redshift decreases or stellar mass of BCGs increases while the alignment is independent of the richness of host clusters which is roughly corresponds to their masses.

More recently, West *et al.* (2017) measured the alignment between orientations of clusters and their BCGs, and obtained the mean value of about $\sim 30^{\circ}$ for 52 clusters. The most important finding of their work is that the alignment extends to $z > 1.3$ with high statistical significance. Their results suggest that the alignment was generated at such an early epoch, about ten billion years ago.

As described above, the ellipticities and alignments of member galaxy distributions have been examined by many previous studies. Previous studies assumed the relation between shapes of light and mass distributions to compare the shapes of them with N-body simulations. However, since it is unclear that the distributions of member galaxies follow those of DM, ellipticities and orientations inferred from them might be different from those of host DM haloes. Thus, hydrodynamical simulations are essential to explore the correlations between shapes of DM haloes and member galaxy distributions. In this thesis, we examine the ellipticities and orientations of stellar components in the Horizon-AGN simulation to interpret the observed non-sphericities inferred from the member galaxy distributions.

2.1.2 Gravitational lensing

The above studies used the distributions of member galaxies to estimate the ellipticities and orientations of galaxy clusters. While mass distributions of their host galaxy cluster can be inferred from the distributions of member galaxies, the estimated values depend on the assumptions between light and mass distributions.

Gravitational lensing is a unique tool to probe the mass distributions directly. Cypriano *et al.* (2004) measured the ellipticities of 24 X-ray selected galaxy clusters individually using weak lensing method. While they detected the non-zero ellipticities, these values were noisy due to quality of observations and shortage of lensed galaxies. Orientations of DM haloes, on the other hand, were determined robustly and found that they are well aligned with those of BCGs. Thus, they confirmed the alignment between orientations of galaxy clusters and CGs using mass distributions instead of those of member galaxies.

Evans & Bridle (2009) stacked the weak lensing signals of galaxy clusters such that the major axes of orientations of DM haloes are aligned with those determined by member galaxy distributions. They detected the mean ellipticity of DM haloes statistically and

ruled out spherical haloes. If either the mass distributions were spherical or the mutual angles between mass and light distributions were randomly distributed, the mean ellipticity would be 0. In the latter case, the spherical result is caused by the random orientations of DM haloes relative to the member galaxy distributions because the stacking processes smear out the individual elliptical distributions. Thus, their results detected simultaneously both ellipticities of DM haloes and alignments between mass and light distributions. They also found that ellipticities of DM haloes are consistent with those of member galaxy distributions.

Oguri *et al.* (2012) measured ellipticities and orientations of 28 galaxy clusters *individually* using strong lensing with Sloan Digital Sky Survey (SDSS). They detected the significant signals of ellipticities of galaxy clusters. In addition, they stacked weak lensing signals so that the major axes of shear maps are aligned with those inferred from strong lensing. The resulting mean value of ellipticities of stacked map is consistent with that estimated from strong lensing. Thus, they confirmed that both weak lensing and strong lensing are useful to measure the ellipticities and orientations of galaxy clusters.

van Uitert *et al.* (2017) measured the mean ellipticity of about 2600 galaxy clusters and groups observed from the Galaxy And Mass Assembly (GAMA) survey by using the weak lensing signal taken from the Kilo Degree Survey (KiDS). They showed that the BCGs and the lensing are well aligned on small scales, $\sim$ 200 kpc, while the member galaxy distribution and the lensing signal are well aligned on large scales, $\sim$ 500 kpc.

Shin *et al.* (2018) measured the mean ellipticities and position angles of member galaxy distributions and lensing signals by using staking method and found that they are well aligned with each other. They also stacked the member galaxy distributions and the lensing signals along the major-axis of the BCGs and inferred a mean alignment angle between BCGs and the mass distributions with a root-mean-square value of $30^\circ \pm 10^\circ$.

Three lensing methods described above have been used to measure shapes of galaxy clusters: weak lensing for individual halo (Oguri *et al.*, 2010; Umetsu *et al.*, 2018), stacking weak lensing signals (Clampitt & Jain, 2016; van Uitert *et al.*, 2017; Shin *et al.*, 2018), and strong lensing (Richard *et al.*, 2010; Oguri *et al.*, 2012). Weak lensing for individual haloes suffers from their large errors associated with shape measurement of lensed galaxies. Stacked signals of weak lensing underestimate the mean ellipticities due to mis-alignments between *a priori* directions in stacking and their true orientations. Strong lensing can evaluate the non-sphericities of DM haloes with much less errors than those estimated by weak lensing. Although there are several studies to measure the ellipticities of DM haloes of galaxy clusters and alignments of their orientations relative to BCGs by using strong lensing (Richard *et al.*, 2010; Oguri *et al.*, 2012), their sample size is relatively limited, $N = 20$. Thus, in this thesis we provide a new measurement ellipticities of DM haloes of galaxy clusters by using strong lensing for a large sample of $N = 45$.

2.1.3 Gas distribution: X-ray surface brightness and the Sunyaev-Zel'dovich effect

Most of baryons in galaxy clusters exist as gas and follow the gravitational potential of host DM haloes, and thus their distributions can be used to infer those of DM. In addition, since their observed properties such as X-ray luminosities or integrated Compton-y parameters of SZ effect can be used to constrain the cosmological parameters (e.g. Vikhlinin *et al.*, 2009; Reichardt *et al.*, 2013), to measure these observable accurately is important. Non-sphericities of the gas distributions reflecting those of DM haloes in galaxy clusters are possible bias in constraining the parameters. In fact, Buote & Humphrey (2012) showed that spherical averaging introduces an offset in the observed relation between X-ray luminosities and the Compton-y parameters. Thus it is important to measure shapes of the gas distributions both in inferring those of host DM haloes and in evaluating values relating to gas properties more accurately.

Since most of the gases in clusters emit X-ray, the X-ray observations is one of the most useful methods to measure shapes of clusters. Once it is assumed that the gas is in hydrostatic equilibrium and thus following the gravitational potential of host haloes, shapes of mass distributions can be inferred from the X-ray surface brightness. Jones *et al.* (1979) measured morphologies of X-ray surface brightness of 12 Abell clusters by using *Einstein* Observatory and found that several of them are elongated and cannot be approximated by a spherical shape. They simply used ratios of maximum and minimum extent of iso-intensity contours as axis ratios. While they evaluated ellipticities of the clusters, their observations were limited in both sample size and resolution.

McMillan *et al.* (1989) measured orientations and ellipticities of X-ray surface brightness for 49 Abell clusters and detected non-sphericities. After McMillan *et al.* (1989), many observational studies measured the ellipticities of the X-ray clusters by various observations such as *Einstein* observatory (e.g. Buote & Canizares, 1992; Mohr *et al.*, 1995), ROSAT observations (e.g. Allen *et al.*, 1995; Buote & Canizares, 1996; Wang & Ulmer, 1997; Kolokotronis *et al.*, 2001), Chandra (e.g. Hashimoto *et al.*, 2007; Lau *et al.*, 2012; Hashimoto *et al.*, 2014; Parekh *et al.*, 2015), and *XMM-Newton* (e.g. Kawahara, 2010; Lovisari *et al.*, 2017) They reported that ellipticities of X-ray surface brightness are rounder than those of DM haloes in N-body simulations or member galaxy distributions and consistent with N-body simulation predictions by assuming the hydrostatic equilibrium. In addition to the ellipticities, Hashimoto *et al.* (2008) measure the alignment angles between the orientations of BCGs and host cluster X-ray position angles. They detected a strong alignment signal while they did not see any clear trend that the degree of the alignments depends on the dynamical state of clusters.

Another option to measure shapes of gas distribution in galaxy clusters is the Sunyaev-Zeldovich effect which is observed through the inverse Compton scattering of cosmic microwave background photons by hot gases in galaxy clusters Sunyaev & Zeldovich (1972, 1980). While the X-ray surface brightness is sensitive to the number density of gases,

$n_{\rm gas}$, written as $\propto \int n_{\rm gas}^2 T_{\rm gas}^{1/2} {\rm d}l$, where $T_{\rm gas}$ denotes the gas temperature and $\int {\rm d}l$ is the integration along the line-of-sight, the Compton y-parameters of the SZ effect depends on these values as $\propto \int n_{\rm gas} T_{\rm gas} {\rm d}l$. Thus, the SZ observations give us a unique information different from X-ray observations.

AMI Consortium *et al.* (2012) measured shapes of the SZ images of 19 clusters selected from the Local Cluster Substructure Survey (LoCuSS) y using the Arcminute Microkelvin Imager (AMI) and detect the non-sphericities of them. Their result is consistent with the prediction of the ΛCDM, which suggests that ellipticities of SZ are expected to be similar to those from X-ray (e.g. Wang & Fan, 2004).

Donahue *et al.* (2016) systematically measured the ellipticities and position angles of lensing signals, X-ray emissions, BCGs, and Sunyaev-Zel'dovich effect. They found that the position angles of those components are well aligned. Since hot gases are collisional components, their distributions considerably depend on a dynamical state of the host galaxy cluster; while hot gas distributions fairly trace the mass distributions for relaxed clusters which is in dynamically equilibrium, hot gas distributions substantially depart from the mass distributions for merging or merged clusters. Actually Montes & Trujillo (2019) showed that the distribution of X-ray emission does not trace the mass distribution at all for merging clusters, while it traces the mass distribution for relaxed clusters.

As described above, shapes of gas distributions in galaxy clusters have been measured by many observational studies. However, there is few studies to examine the ellipticities of gas distributions in hydrodynamical simulations. While Suto *et al.* (2017) measured the shapes of X-ray surface brightness of galaxy clusters in the Horizon-AGN simulation, they only focused on the ellipticities. Thus, in this thesis, we measure ellipticities and orientations of gas distributions to compare the previous observations described above and theoretical predictions of the ΛCDM model.

2.1.4 Intracluster light

The brightest cluster galaxy (BCG) generally has a very extended, $\sim$ 500 kpc, stellar halo called intracluster light (ICL) which is first discovered by Matthews *et al.* (1964) and confirmed by later studies (e.g. Oemler, 1973, 1976; Schombert, 1986, 1987, 1988). Since hot gases are collisional components while DM and stars are collisionless particles, the ICL is expected to trace mass distributions independent of the dynamical state.

Gonzalez *et al.* (2005) measured the ellipticities of ICL distributions and found clear non-sphericities of them. They measured the radial dependence of the ellipticities and confirmed that the values in the inner regions are similar to those of elliptical galaxies and thus are associated with the BCG. The ellipticities in outer regions are more elongated than inner regions and are consistent with those of member galaxy distributions implying that ICL traces the host cluster haloes rather than the BCGs. The position angles of outer regions and inner regions are well aligned with each other indicating the alignments between clusters and BCGs.

Montes & Trujillo (2019) estimated the distribution of the mass, ICL, and X-ray emission for massive 6 clusters and compared them by using the Modified Hausdorff distance

(MHD) as a method of quantifying the similarities. They found that ICL distributions are quite similar with mass distributions with the mean value of MHD$\sim$ 25 kpc independent of the dynamical state of clusters. Their result suggests that the ICL can be used as a new luminous tracer of mass distributions.

In this thesis, we do not focus on the shapes of ICL in the hydrodynamical simulation. However, the shapes of ICL can be examined in the simulations and the relation between shapes of ICL and host DM haloes can be checked by observations when more observations will measure the both shapes of ICL and host DM haloes in the future.

2.2 Non-sphericities of galaxy clusters: numerical simulations in ΛCDM universe

Numerical simulations provide various theoretical predictions of cosmological models which they adopt, and thus are a powerful tool to test the models by comparing the predictions with observations. Many studies using N-body simulations also suggest that the non-sphericities of DM haloes are ubiquitous in the ΛCDM universe as well as observations. In fact, early studies using numerical simulations showed that the non-sphericities of galaxy clusters provide constraints on cosmological models (e.g. Evrard *et al.*, 1993; Jing *et al.*, 1995; Splinter *et al.*, 1997; Suwa *et al.*, 2003).

Jing & Suto (2002) presented a systematic and statistical study to model shapes of DM haloes by analysing cluster-, group-, and galaxy-sized haloes in N-body cosmological simulations. They computed axis ratios of iso-density surfaces at different scales of each DM halo by diagonalizing the inertia tensor of particles within each surface. They showed that shapes of DM haloes are well approximated by triaxial and cluster-sized haloes are more elongated than galaxy-sized haloes. They also found that inner regions are more elongated than outer regions, and DM haloes at different scales are well aligned with each other at galaxy cluster scales. Thus, numerical simulation based on the ΛCDM model predicts the alignments between DM haloes in inner and outer regions, which is qualitatively consistent with the observed alignments between BCGs and host clusters.

After Jing & Suto (2002), a number of studies investigated the non-sphericities of galaxy cluster-sized DM haloes in N-body simulations with higher resolutions and larger box sizes. In this period, since the ΛCDM model has been considered as the most likely cosmological model, most of the simulations are based on the ΛCDM. The main interests of them are on a dependence of non-sphericities on radial distance from the centre, mass, and redshift. For the radial dependence, most studies suggested that inner regions of cluster scale DM haloes are more elongated than outer regions for fixed masses and redshifts (e.g. Bailin & Steinmetz, 2005; Allgood *et al.*, 2006; Faltenbacher *et al.*, 2008; Schneider *et al.*, 2012; Despali *et al.*, 2014) while other studies showed the opposite results (e.g. Hopkins *et al.*, 2005). For the mass dependence, all the studies suggested that more massive DM haloes have more elongated shapes than lighter haloes for fixed redshifts and radial scales (e.g. Kasun & Evrard, 2005; Hopkins *et al.*, 2005; Allgood *et al.*, 2006; Schneider *et al.*,

2012; Despali *et al.*, 2014). For the redshift dependence, all the studies suggested that DM halo shapes become more elongated toward higher redshifts for fixed masses and radial scales (e.g. Kasun & Evrard, 2005; Hopkins *et al.*, 2005; Bailin & Steinmetz, 2005; Ho *et al.*, 2006; Allgood *et al.*, 2006; Schneider *et al.*, 2012; Despali *et al.*, 2014).

The mass dependence and the redshift dependence can be understood under the bottom-up structure formation scenario predicted by the ΛCDM model as follows. In the early stages of halo formation, DM haloes are elongated due to mergers, and as time passes, they approach equilibrium and become round. The heavier haloes are, the more elongated they are because they are young objects formed at late epoch. Therefore, the ellipticities of observed galaxy clusters can be used to as cosmological probes to constrain on the model parameters. In fact, several studies argued that values of axis ratios and degrees of their redshift dependences are depend on the cosmological parameters, especially σ_8 (e.g. Ho *et al.*, 2006; Allgood *et al.*, 2006). The lower values of the σ_8 made halo formation epochs later, and thus the shapes of them become more elongated.

To explain the observed alignments between BCGs and galaxy clusters have been also one of the main subjects in this research field. Although BCGs do not exist in DM only N-body simulations, the observed alignments are considered as alignments between inner and outer regions of DM haloes if BCGs and member galaxy distributions trace orientations of inner and outer regions of DM haloes, respectively. Thus, many studies investigate the alignments (e.g. Song & Lee, 2012; Schneider *et al.*, 2012; Despali *et al.*, 2016). Their results suggest the inner and outer regions are well aligned, and thus qualitatively confirm the observed alignments

However, a direct comparison with observations requires baryon components such as BCGs or member galaxies which are not included in DM only N-body simulations. It should be assumed that BCGs and member galaxy distributions trace orientations of inner and outer regions of DM haloes, respectively to compare the results from DM only simulations with observations. Thus, interpretations of the results depend on the validity of the assumption.

In fact, Kang *et al.* (2007) showed that orientations of galaxies and their host DM haloes are fairly misaligned with each other. If we assume that orientations of galaxies and those of their host DM haloes are perfectly aligned with each other, central-satellite alignment signals of theoretical predictions are too strong to explain the observed ones The orientations should be misaligned to reproduce the observation, and they estimated the mean misalignment angle about $\sim 40°$. Therefore, hydrodynamical cosmological simulations are essential for fair comparisons of theoretical predictions of the ΛCDM model with observations directly.

Early studies using simulations with baryon physics found that cooling and star formation make DM halo shapes substantially rounder, especially at inner regions (e.g. Kazantzidis *et al.*, 2004; Springel *et al.*, 2004). These simulations overestimated the inner density profiles of DM haloes. The rounding shapes and the overestimates are ascribed to over cooling at inner regions. Additional heating sources such as AGN feedback should be implemented to reproduce various observational properties. Recently, many studies

investigate non-sphericities and alignments of galaxy clusters using hydrodynamical simulations with AGN feedback (e.g. Tenneti *et al.*, 2014; Dong *et al.*, 2014; Velliscig *et al.*, 2015a; Chisari *et al.*, 2017).

Tenneti *et al.* (2014) analysed non-sphericities and alignments between galaxies and DM haloes with masses of $10^{10}h^{-1}M_{\odot} < M_{\rm halo} < 10^{14}h^{-1}M_{\odot}$ (where $M_{\rm halo}$ denotes the mass of DM haloes) in the MassiveBlack-II (MBII) cosmological hydrodynamical simulation. The resulting axis ratios were more elongated with higher redshifts, higher masses, and thus qualitatively consistent with DM only simulations. The mean alignment angle were also computed and found that they depends on the halo mass such as $\sim 30^{\circ}$ to $\sim 10^{\circ}$ for $M_{\rm halo} \sim 10^{10} - 10^{14}\ h^{-1}M_{\odot}$.

Dong *et al.* (2014) analysed DM haloes with mass of $10^{12}h^{-1}M_{\odot} < M_{\rm halo} < 10^{14}h^{-1}M_{\odot}$ in a cosmological hydrodynamical simulation and investigated dependences of alignments between DM haloes CGs on various properties such as CG colours, CG stellar masses, CG metallicities, host halo masses, and distances from CGs. They reproduced observed CG color dependence of alignments: redder galaxies are aligned with host DM haloes tighter than blue ones. They predicted that alignments depend more strongly on metallicity at small scales. This prediction could be testable in future observations.

Velliscig *et al.* (2015a) reported the alignments and non-sphericities of stellar and hot gas distributions as well as DM haloes, in the Evolution and Assembly of GaLaxies and their Environments (EAGLE) and OverWhelmingly Large Simulations (cosmo-OWLS) simulations, which include AGN feedbacks. The mass range is $10^{11}h^{-1}M_{\odot} < M_{\rm halo} < 10^{15}h^{-1}M_{\odot}$. Their results showed that DM halo shapes become more elongated with increasing radii, redshifts, and halo masses. Only the radial dependence is different from most of DM only simulations, which suggests that baryon implementation changes ellipticities of DM haloes. They also found that CGs and hot gases are well aligned with the entire DM distributions, and the alignments are strongest for galaxy clusters.

Chisari *et al.* (2017) investigated shapes and alignments of DM haloes in the Horizon-AGN simulation with mass range of $3 \times 10^{10}h^{-1}M_{\odot} < M_{\rm halo} < 5 \times 10^{14}h^{-1}M_{\odot}h^{-1}M_{\odot}$. Their results showed that more massive and high redshift haloes are more elongated, which is qualitatively consistent with DM only simulations. The alignment angles are also stronger for more massive and higher redshift haloes.

While many studies investigated the non-sphericities and alignments of DM haloes in hydrodynamical simulations with AGN feedback, most of the above studies are motivated by the galaxy-halo alignments, in the context of intrinsic alignments. Only a few studies explored the shapes and alignments of galaxy clusters in the simulations. Suto *et al.* (2017) measured the projected shapes of 40 galaxy clusters in the Horizon-AGN simulation. They found that projected ellipticities of X-ray surface brightness in the simulation give a better prediction of X-ray observations in Kawahara (2010) than those of iso-potential of DM haloes in DM only simulation in Jing & Suto (2002). This result indicates that the assumption of hydrostatic equilibrium cannot be always adopted, and thus hydrodynamical simulations are essential for direct comparisons with observations. Although they focused on galaxy clusters in the hydrodynamical simulations, they did

not investigate the alignments in the clusters. Thus, in this thesis we investigate both the ellipticities and alignments of galaxy clusters in the latest hydrodynamical simulation.

2.3 Connection of cluster non-sphericities to surrounding matter distributions

In previous sections, we summarized results of numerical studies concerning alignments between galaxy clusters and their BCGs. Binggeli (1982) reported that orientations of galaxy clusters tend to be aligned with the direction to the closest neighboring clusters and the alignments are found with separation of ~ 30 Mpc. The alignment can be considered as the alignment between orientations of galaxy clusters and those of their surrounding matter distributions.

West *et al.* (1989) tested cosmological models by comparing observed alignments between orientations of galaxy clusters and those of surrounding galaxy distributions with the alignments in N-body simulations. Their study was motivated by the finding of Binggeli (1982), cluster-cluster alignments, and thus they explored the orientations of galaxy clusters relative to their large scale environments ~ 10 Mpc. Their results suggested that the alignments provide a very useful probe to test the models. By comparing the simulations with observations, they concluded that the CDM model is confronted with the alignments at such large scales. Although their study showed that the alignments can be used as a powerful tool to constrain cosmological models, the simulations were quite limited by a numerical resolution.

This is naturally understood in the ΛCDM model because it predicts galaxy clusters are located at intersection points of filaments and grow by mergers or mass accretion episodes along the filaments resulting in elongated along the directions. Thus, the alignment between orientations of clusters and directions of surrounding filaments are a general consequence of structure formation scenarios of the ΛCDM model. In addition, alignments between orientations of galaxies and the filaments have been studied intensively because they can be possible contamination of weak lensing signals which are derived based on the assumption that background galaxies are randomly oriented (e.g. Hirata *et al.*, 2007; Joachimi *et al.*, 2011; Krolewski *et al.*, 2017). Some observations detected the alignments (intrinsic alignments) (e.g. Mandelbaum *et al.*, 2006; Singh *et al.*, 2015; Huang *et al.*, 2018; Chen *et al.*, 2019), which support the structure formation scenarios of the ΛCDM model.

The alignments relative to surrounding matter distributions were also detected in observed clusters as well as galaxies. Durret *et al.* (2019) detected the alignments between orientations of BCGs and their surrounding matter distribution defined by the galaxy distribution by using SDSS DR 8 data, indicating that clusters and BCGs are coherently aligned relative to their surrounding matter distributions. Their result implies that major mergers and smooth accretions along the filaments contribute to determine their orientations, given that they grow by these mergers and accretions. Wittman *et al.* (2019) explored the alignments between orientations of a BCG and the other BCG in merging

galaxy clusters and showed that the BCGs are aligned with each other. This result implies that BCGs are initially aligned to their surrounding matter distributions independent of mergers or such alignment processes happen very quickly, within ~ 1 Gyr after mergers. Considering that the mergers occur preferentially along the filaments, both results of these two papers suggest that the surrounding matter distributions plays an important role in alignments of galaxy clusters.

Numerical simulations also investigated the alignments between orientations of galaxy clusters and their surrounding matter distributions. Lee (2019) used DM distributions in DM only simulation and computed the tidal field tensor defined as,

$$\boldsymbol{T}(x) \propto \frac{\partial^2}{\partial_i \partial_j} \int \mathrm{d}\boldsymbol{x}' \Phi(\boldsymbol{x}') W(|\boldsymbol{x} - \boldsymbol{x}'|; R_f), \tag{2.6}$$

where $\Phi(\boldsymbol{x})$ is the gravitational potential at $\boldsymbol{x}$ and $W(|\boldsymbol{x} - \boldsymbol{x}'|; R_f)$ is a Gaussian window function with a smoothing scale R_f. If the smoothing scale is sufficiently large, eigenvectors of the tidal field represent the preferred directions of surrounding matter distributions. The major axes of DM haloes with galactic mass scale of $0.5 \leq M_{\rm halo}/10^{11} h^{-1} M_\odot \leq 50$ are aligned with the eigenvector of the least eigenvalue of the tidal field with smoothing length of $\sim 30 h^{-1}$ Mpc. This result suggests that shapes of DM haloes with galactic mass scales are determined by the large scale as predicted by the first order Lagrangian perturbation theory (Zel'Dovich, 1970; Buchert, 1992), which is consistent with other DM only simulations (e.g. Hahn *et al.*, 2007; Zhang *et al.*, 2009; Joachimi *et al.*, 2013; Chen *et al.*, 2016; Xia *et al.*, 2017; Piras *et al.*, 2018), and observations (e.g. Zhang *et al.*, 2013; Chen *et al.*, 2019).

The surrounding matter distributions may play an important role to generate the observed alignments between galaxy clusters and BCGs because it changes orientations of both DM haloes and BCGs coherently. Especially, galaxy clusters generally reside at intersection of filaments, their orientations are affected by the anisotropic mergers or mass accretion episodes along the filaments. Thus, in this thesis, we explore the relation between orientations of clusters and the directions of filaments in order to understand the origin of the observed alignments.

Chapter 3

Projected non-sphericities and alignments of stellar, gas, and dark matter distributions in simulated clusters

Many observations have measured ellipticities of galaxy clusters and shown that their orientations are well aligned with those of their central galaxies. Since to construct analytical models for the ellipticities and alignments is a tough task and most of past theoretical studies made predictions based on numerical simulations. Jing & Suto (2002) performed the pioneering work in constructing the theoretical predictions about the non-sphericities of galaxy clusters. They characterized ellipticities of galaxy cluster sized dark matter (DM) haloes and showed that inner part and outer part of DM haloes are well aligned with each other.

However, since their theoretical predictions were based on DM only N-body simulations, their results cannot be directly compared with observations in visible light, X-rays, and radio wavelengths. Furthermore, their shapes also depend on baryon physics such as AGN feedback and star formation, so even if we are interested in only DM shapes, theories should be updated. Therefore, cosmological hydrodynamical simulations incorporating baryon physics are essential to construct reliable theoretical predictions for the results of such multi-wavelength observations.

Although such simulations have been difficult for a long time due to lack of understanding of baryon physics and computational limitations, only recently reliable simulation results have become available, which are consistent with a number of observations. Suto *et al.* (2017) used one of the latest simulations, the Horizon-AGN simulation, to construct theoretical predictions of the non-sphericities of galaxy clusters that can be directly observed by X-ray and visible light. However, they focused only on the ellipticities of the entire cluster, and they did not investigate the alignments between galaxy clusters and central galaxies.

Therefore, in this chapter we also use the results of one of the latest simulations incorporating baryon physics, the Horizon-AGN simulation. We identify galaxy clusters and their central galaxies formed in the simulation, and make reliable theoretical predictions of the ΛCDM model. In particular, we measure the non-sphericities of galaxy clusters directly observed in visible light, X-rays, and radio wavelengths, and compare the alignments between their orientations and those of CGs. Furthermore, we check the validation of the ΛCDM model by comparing the theoretical predictions from the simulation with the currently available observations. See Appendix A for a detailed description of the Horizon-AGN simulation.

3.1 Identifying galaxies and clusters in the Horizon-AGN simulation

Following Suto *et al.* (2017), we identify dark matter haloes using the ADAPTAHOP halo finder (Aubert *et al.*, 2004; Tweed *et al.*, 2009). ADAPTAHOP is a subhalo finder that separates multiple subhaloes while comparing the relative heights of peaks and saddle points of the smoothed density field. After we obtain the halo catalogue, we pick up all DM haloes with masses larger than $5 \times 10^{13} M_{\odot}$, which are defined by those within spherical average density larger than 200 times the critical density of the Universe. Since the mass scale roughly corresponds to that of observed galaxy clusters, it is reasonable that we regard these haloes as galaxy clusters. The total number of these cluster-sized haloes is 40 in the Horizon-AGN simulation, which are the same haloes examined by Suto *et al.* (2017). For the each cluster-sized haloes, stellar haloes are also identified with the ADAPTAHOP finder applying to stellar particles and the haloes with more than 50 stellar particles are regarded as galaxies. Since each stellar particle has the mass of about $2 \times 10^6\ M_{\odot}$, this criterion corresponds to the minimum stellar mass of about $10^8\ M_{\odot}$ in our final galaxy catalogue.

The definition of the centre of each cluster needs to be considered carefully as well. One reasonable option is to compute the centre-of-mass for each cluster from their dark matter, star and gas components. This is a straightforward procedure in simulation data, but is difficult to apply in observations. In reality, the centre of observed galaxy clusters is often defined as the location of its brightest cluster galaxy (BCG). While we can compute the luminosity of each galaxy in principle (Dubois *et al.*, 2014), it is complicated and also subject to uncertainty of the star formation history. Therefore we decide to adopt the position of the most *massive* galaxy (within 1 Mpc from the most bound DM particle of each halo) as the centre of cluster. In this thesis, we call such a galaxy as central galaxy (CG) so as to distinguish it from BCG. In practice, however, they are supposed to be almost identical to the observed BCGs. Thus we identify these two populations when we compare our results with the observation in section 3.5.

Since observational data provide only projected images, we focus on projected alignments between CGs and other components in our simulation. First we determine position

angles and ellipticities of projected CGs. Following Suto *et al.* (2017), we use the mass tensor to estimate ellipticities and position angles:

$$I_{\mathrm{CG},\alpha\beta} \equiv \sum_{i=1}^{N_{\mathrm{CG}}} m_{\mathrm{CG}}^{(i)} \left[x_{\mathrm{CG},\alpha}^{(i)} - x_{\mathrm{CG},\alpha}^{\mathrm{CM}}\right] \left[x_{\mathrm{CG},\beta}^{(i)} - x_{\mathrm{CG},\beta}^{\mathrm{CM}}\right] \qquad (\alpha, \beta = 1, 2), \tag{3.1}$$

where $m_{\mathrm{CG}}^{(i)}$ and $x_{\mathrm{CG},\alpha}^{(i)} - x_{\mathrm{CG},\alpha}^{\mathrm{CM}}$ are the mass and the projected position vector of the i-th CG particle relative to the centre of mass, respectively. The summation runs over the N_{CG} star particles within the ellipse whose size is $\sqrt{ab} = 20\,\mathrm{kpc}$, where a and b are the semi-major and semi-minor axes, respectively. We diagonalize the mass tensor to obtain semi-major axis a, semi-minor axis b, and position angle θ. We start from a circle with radius of $r = 20\,\mathrm{kpc}$ centred at the centre of mass of CG particles. Then we reset the centre of mass of particles within the new ellipse and compute the tensor iteratively until both eigenvalues of the tensor are converged within 10^{-8}. The bottom panels in Fig. 3.1, 3.2, and 3.3 show examples of resulting ellipses for three galaxy clusters.

When both eigenvalues converge, we obtain values of semi-major axis a_{CG}, semi-minor axis b_{CG}, the centre of mass $x_{\mathrm{CG},\alpha}^{\mathrm{CM}}$, and position angle θ_{CG} of the CG. We define the ellipticity of the CG as:

$$\epsilon_{\mathrm{CG}} = 1 - \frac{b_{\mathrm{CG}}}{a_{\mathrm{CG}}}. \tag{3.2}$$

For each cluster, we consider three different projection directions assuming x-, y-, and z-axes as line-of-sight directions. We regard these three projections as independent so that we effectively have $N_{\mathrm{cl}} \equiv 120$ galaxy clusters for our analysis. Although the three different projection directions are not independent, we confirmed that our results such as mean ellipticities and the rms of position angle differences between various components shown in section 3.4.2 are not significantly changed even if we do not combine results with these three different projection directions.

3.2 Ellipticity and position angle from projected images of the clusters

In the Horizon-AGN simulation, dark matter and star are defined by particles but gas is computed in the adaptive mesh. Each dark matter particle has the same mass and has the position, whereas each star particle has both a position and mass. Each adaptive mesh contains position, mass, metallicity, temperature, and size of the mesh.

In this chapter, we compare the ellipticity and position angle for projected images of X-ray surface brightness (XSB), Compton $y-$parameter (SZ), total surface mass density (tot), dark matter surface mass density (DM), star surface mass density (star), and gas surface mass density (gas) of galaxy clusters in the Horizon-AGN simulation. To create these projected images, we first define a cube with a size of $(4.24\,\mathrm{Mpc})^3$ centred at the CG. Note that the position of the CG is defined as the center of mass $x_{\mathrm{CG},\alpha}^{\mathrm{CM}}$ computed in section 3.1. Then, we divide the cube into $(4001)^3$ meshes with a size of $(1.06\,\mathrm{kpc})^3$, which

corresponds to the minimum size of the adaptive mesh in the Horizon-AGN simulation. Mass densities of dark matter, star and gas, metallicity, and temperature, are assigned to each mesh. For dark matter and star, mass densities are simply computed by the nearest grid point method, in which mass of each particle is assigned to the nearest mesh in a projected plane. Since the gas property is computed in the adaptive mesh, we divide all meshes into the smallest meshes of $(\Delta = 1.06\,\mathrm{kpc})^3$ with the same values of temperature, metallicity, and mass density. For these projected images, ellipticity and position angle are estimated by using a tensor weighted by projected values such as surface mass density, XSB, and y-parameter as described in the following subsections.

3.2.1 Surface densities of different components

Projected images are created as follows:

(I) surface mass density (DM, star, gas, and tot):
We compute the mass density of the mesh

$$\rho_A(i,j,k) = m_A(i,j,k)/\Delta^3, \tag{3.3}$$

where $0 \leq i,j,k \leq 4000$ are indices specifying the mesh, and $m_A(i,j,k)$ and $\rho_A(i,j,k)$ are mass and mass density of A component (A = DM or star or gas) in (i,j,k) mesh, respectively. The surface mass density is calculated by integrating the mass density along the line of sight:

$$\Sigma_A(i,j) = \Delta \sum_{k=0}^{4000} \rho_A(i,j,k). \tag{3.4}$$

The total mass density is simply computed by the summation of all these components,

$$\Sigma_{\mathrm{tot}}(i,j) = \Sigma_{\mathrm{DM}}(i,j) + \Sigma_{\mathrm{star}}(i,j) + \Sigma_{\mathrm{gas}}(i,j). \tag{3.5}$$

(II) X-ray Surface Brightness (XSB):
The X-ray Surface Brightness (XSB) is calculated as

$$\Sigma_{\mathrm{XSB}}(i,j) \propto \sum_{k=0}^{4000} n_{\mathrm{gas}}^2(i,j,k)\Lambda(T,Z), \tag{3.6}$$

where $n_{\mathrm{gas}}(i,j,k)$, $\Lambda(T,Z)$, $T = T(i,j,k)$, and $Z = Z(i,j,k)$ denote the number density, cooling function, temperature, and metallicity of the gas in a mesh specified by (i,j,k), respectively. We use the package SPEX to derive the cooling function, Λ, for the photon energy band, $0.5\,\mathrm{keV} < E < 10\,\mathrm{keV}$.
The molecular number density of the gas is computed from the mass density:

$$n_{\mathrm{gas}}(i,j,k) = \frac{\rho_{\mathrm{gas}}(i,j,k)}{\mu m_{\mathrm{p}}} \tag{3.7}$$

where μ and m_{p} represent the mean molecular weight and mass of proton, respectively. We confirmed the mean molecular weight is almost constant independent

of the position of meshes within the range of our interest. Since we are interested in only the shape of each component, the normalization does not affect our results and exact value of μ is not important.

(III) Compton y-parameter of the Sunyaev-Zel'dovich effect (SZ) :
The thermal Sunyaev-Zel'dovich effect is characterized by the Compton y-parameter. We calculate the y-parameter in the Horizon simulation as follows:

$$\Sigma_{\rm SZ}(i,j) \propto \sum_{k=0}^{4000} n_{\rm gas}(i,j,k)T(i,j,k). \tag{3.8}$$

Fig. 3.4 plots an example of the images projected to the z-direction for one cluster in our sample. The further detail of this cluster is described in section 3.2.3.

3.2.2 Procedure of ellipse fit

In order to estimate the ellipticity of each component described in section 3.2.1, we use surface density weighted tensor:

$$I_{A,\alpha\beta} = \sum_{i,j} \Sigma_A(i,j) \left[x_\alpha(i,j) - x^{\rm CM}_{{\rm CG},\alpha}\right] \left[x_\beta(i,j) - x^{\rm CM}_{{\rm CG},\beta}\right] \tag{3.9}$$

where $x_\alpha(i,j) - x^{\rm CM}_{{\rm CG},\alpha}$ and $\Sigma_A(i,j)$ denote the projected position relative to centre of mass and value of (i,j) cell, respectively. The summation runs over cells within a given enclosed ellipse region.

We basically follow Suto *et al.* (2016, 2017) to estimate ellipticities and position angles. However, we fix the centre of the ellipse to that of CG, $x^{\rm CM}_{{\rm CG},\alpha}$ derived in section 3.1, unlike those papers where they set the centre to the centre of mass since we are especially interested in the ellipticity and position angle that can be directly compared with observations.

We diagonalize the tensor to obtain values of axis ratio $b/a(<1)$ and position angle. We define the ellipticity as $\epsilon \equiv 1-b/a$. Starting from a circle with radius r, the above process is iterated changing the axis ratio b/a until both two eigenvalues of the tensor converge within 10^{-8}. We confirm that both values of ellipticity and position angle converge well by this convergence criteria. When both eigenvalues converge, we obtain the final values of ellipticities ϵ_A, and position angles θ_A. Finally, we repeat the same analysis for each galaxy cluster with different sizes of the ellipse, $\sqrt{ab} = 0.1,\ 0.2,\ \cdots,\ 1.0$ Mpc.

3.2.3 Examples of the ellipse fit

In this section, we discuss the resulting images and ellipses derived by the above procedure for clusters as examples. First, we show three representative galaxy clusters just to show morphological diversity of galaxy clusters that we analysed in this thesis. Fig. 3.1 shows projected images of DM, star, gas, and CG distributions of the cluster described in Fig. 3 of Suto *et al.* (2017), which is the most massive single-core dominated cluster with mass of $M_{200} = 6.2\times10^{14}M_\odot$. Since we are interested only in the shape of cluster, the absolute

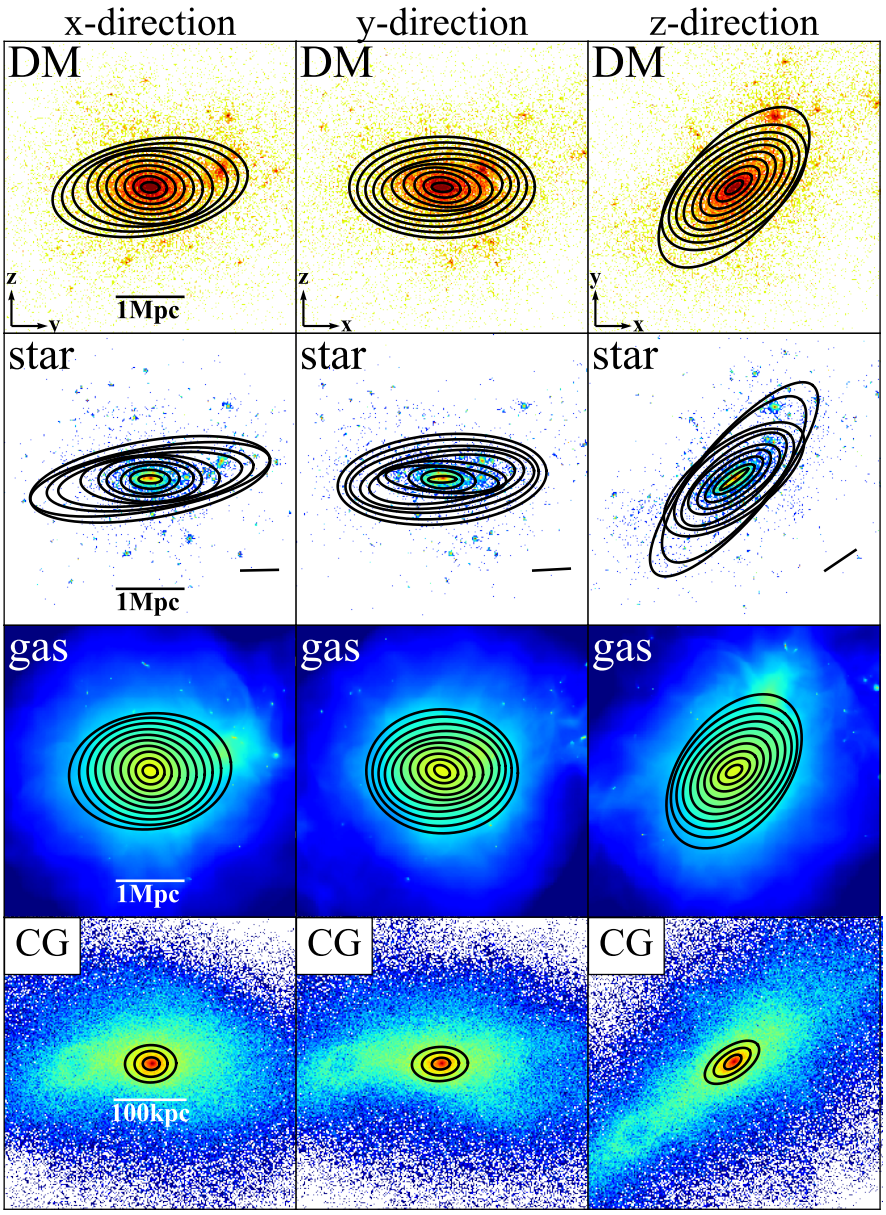

Figure 3.1. Projected distributions of dark matter, star, gas, and the CG from top to bottom of a galaxy cluster. The sizes of the panels are 4.24 Mpc×4.24 Mpc for dark matter, star, and gas distributions and 400 kpc×400 kpc for the CG distributions. Left, centre, and right panels show images projected along x-, y-, and z-directions, respectively. Bars at right bottom in the star panels indicate the direction of the major-axis of the CG.

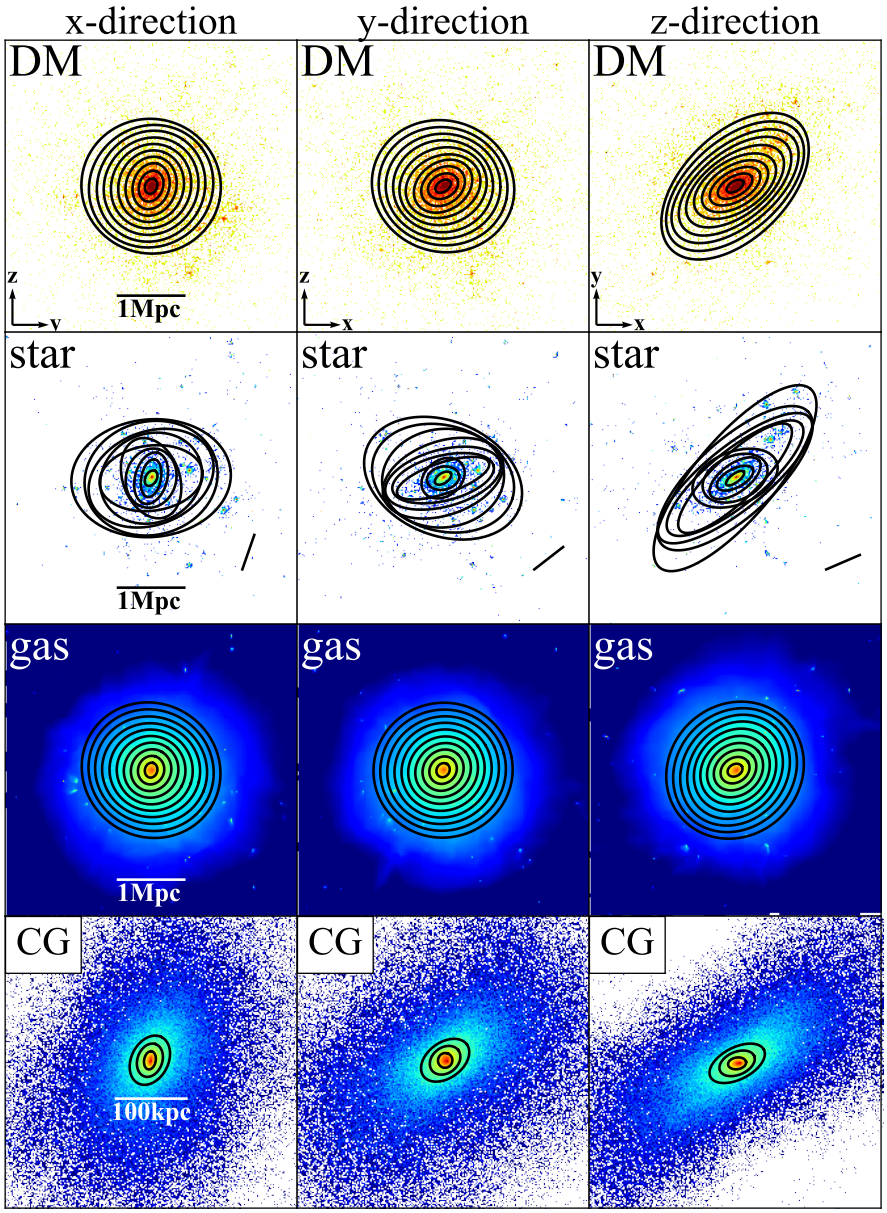

Figure 3.2. The same images as Fig. 3.1 but for an example of clusters having rounder shapes in projected images.

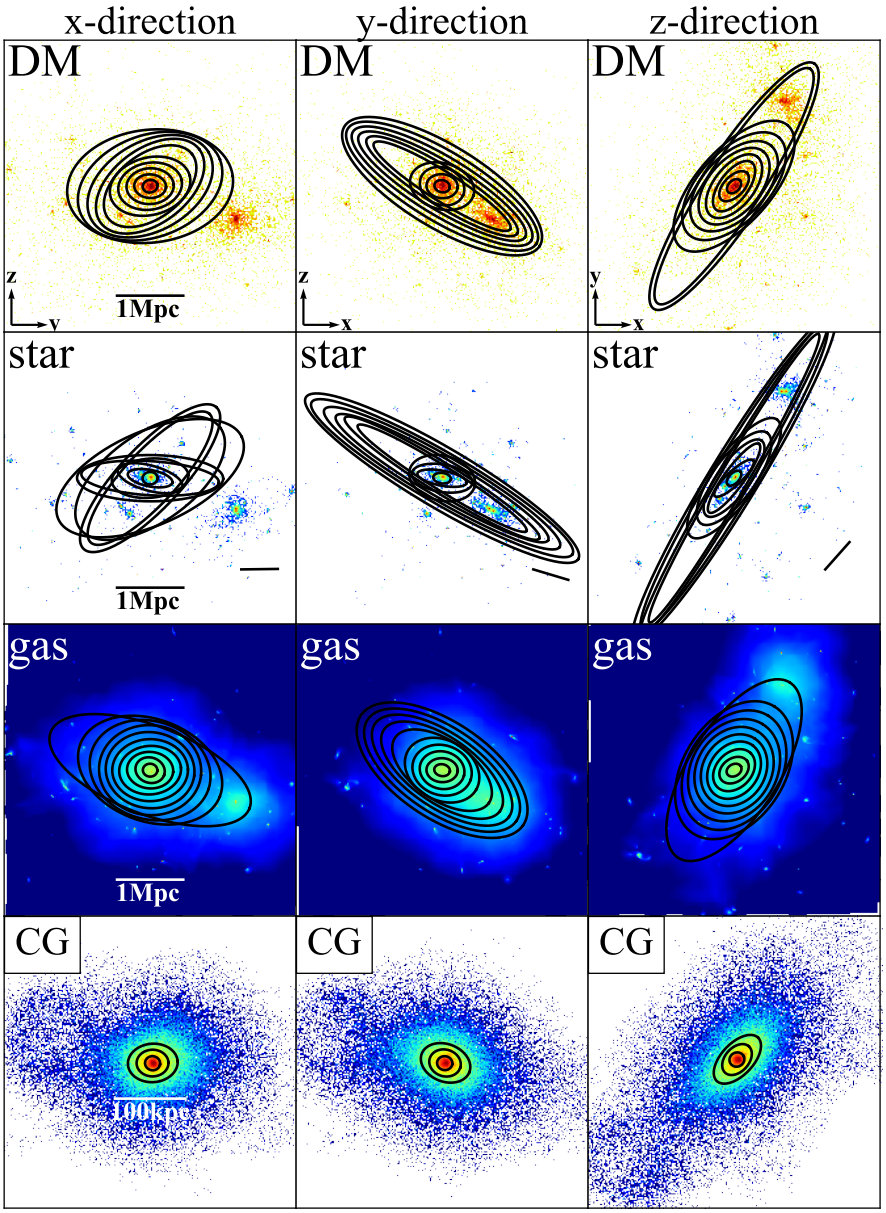

Figure 3.3. The same images as Fig. 3.1 but for an example of clusters having dominant substructures that significantly affect the ellipse fit.

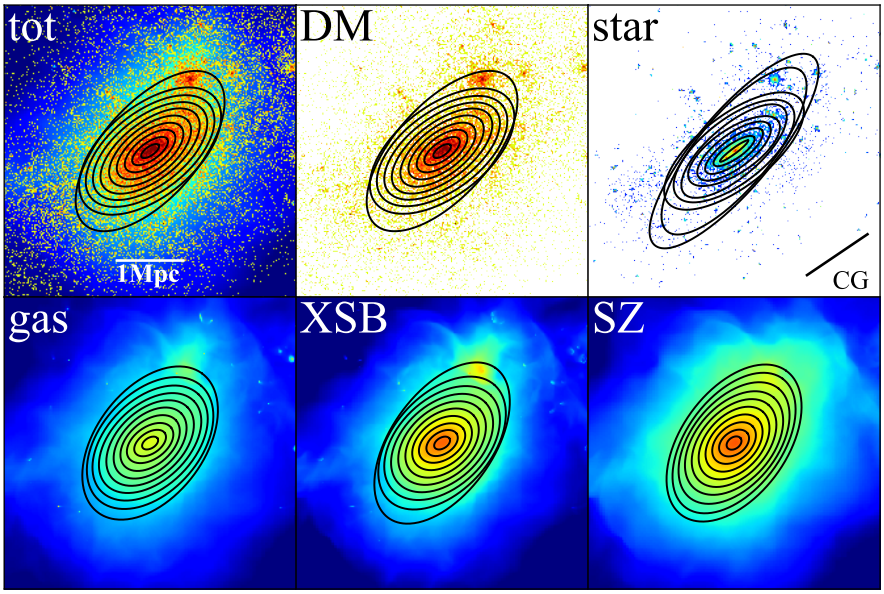

Figure 3.4. An example of projected images of a cluster over 4.24 Mpc×4.24 Mpc for different components (integrated over 4.24Mpc along the z-direction of simulation); total density (*upper-left*), dark matter density (*upper-centre*), star density (*upper-right*), gas density (*lower-left*), X-ray surface brightness (*lower-centre*), and y-parameter from the SZ effect (*lower-right*). Those quantities are sampled in 1.06 kpc×1.06 kpc pixels before integrated along the line-of-sight. Colour-coded according to their absolute values. Solid curves indicate to ellipses computed by the tensor method described in section 3.2.2, corresponding to $\sqrt{ab} = 0.1, 0.2, \cdots, 1.0$ Mpc (i.e., the area of each ellipse is πab) The direction of the major-axis of CG is also shown at the lower right in star image.

values of colour scales are not shown. The dark matter halo looks elliptical for all three line of sights, indicating that their three dimensional shape is triaxial. Fig. 3.2 shows another example, which has relatively rounder shape of the dark matter halo. Such a round cluster may be a relaxed cluster that have experienced the major-merger in the past. In spite of such a round shape of dark matter halo, the star distribution is elliptical due to sub-structures. While dark matter distributions projected along x- and y-directions are circular, that projected toward z-direction is elliptical, clearly demonstrating that circular distributions in projected space do not necessarily indicate spherically symmetric distributions in three dimensional space. Fig. 3.3 shows an example of clusters which have dominant substructures in dark matter distributions. There is a dominant sub-halo in the dark matter distribution, which significantly distort the ellipses for all the projected images that are used to derive ellipticities and position angles. We find that about one

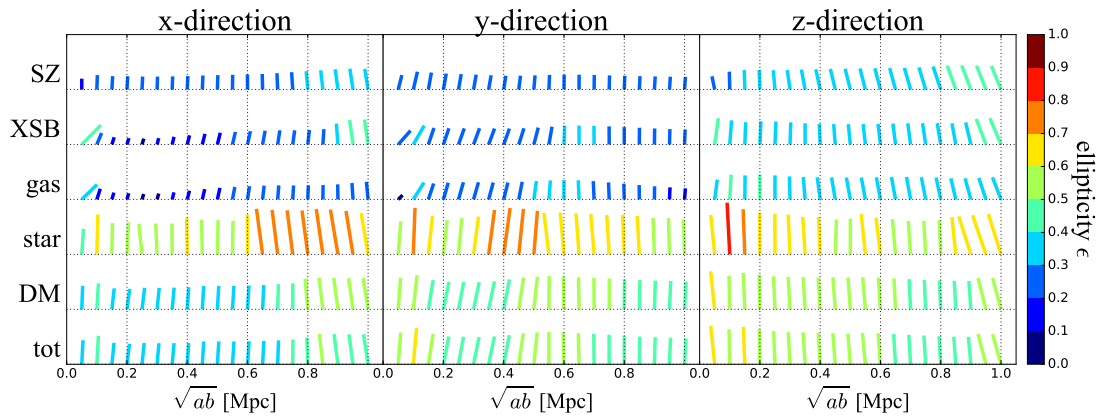

Figure 3.5. Projected position angles of each component of a cluster plotted in Fig.3.4. The inclination of the bar with respect to the vertical direction indicates the position angle, i.e., the direction of the major axis of the ellipse of each component relative to that of CG. The length and colour of bars denote to the value of the ellipticity $\epsilon = 1 - b/a$. Left, middle, and right panels show the result for thee projection along x-, y-, and z-directions of the simulation, respectively.

third of clusters we analysed have such dominant substructures.

Next, we focus on the cluster illustrated in Figure fig:im2 and show images projected along the z-direction of the simulation box for six components (tot, DM, star, gas, XSB, and SZ). Position angles for the six components at all scales are roughly aligned relative to that of CG. This is one of our main results, which will be discussed more statistically in sections 3.3 and 3.4. Comparing the ellipses for the six components, the stellar density distribution is more elongated, while those of gas components (gas, XSB, and SZ) are more spherical than that of DM. The former is because stellar components suffer from strong radiative cooling. The latter is because the gas distribution follows the gravitational potential of the host cluster that is rounder than the matter distribution. Total matter density distribution is almost the same as that of dark matter, simply because total matter density is dominated by dark matter.

We also evaluate the differences among different projection directions. Fig. 3.5 simultaneously plots ellipticity and position angle for each component as a function of scale $\sqrt{ab}$. The above statements for z-direction hold also for the other projections, x-, and y-directions; the position angles are clearly aligned with respect to the CG at almost all scales, gas components are more circular and stellar components are more elongated than that of dark matter, and finally the density distribution of total matter is quite similar to that of dark matter. The ellipticity does not change substantially against the scales except for that of stellar distribution which is sensitive to the presence of substructures. Since these results are just derived one cluster, we examine these features more statistically using all the 40 clusters in the next section.

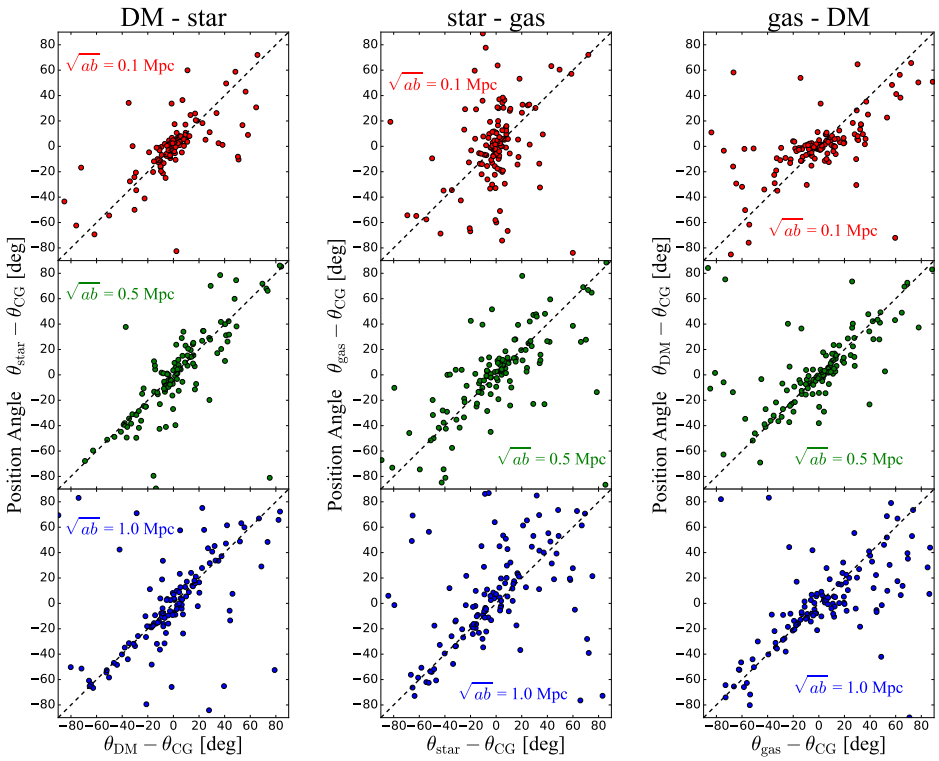

Figure 3.6. Correlation of position angles relative to the CG for different components evaluated at $\sqrt{ab} = 0.1$ (*top*), 0.5 (*middle*), and 1.0 Mpc (*bottom*). Left, middle, and right panels show the correlations between DM and star, star and gas, and gas and DM, respectively.

3.3 Correlation of ellipticities and position angles among different components

3.3.1 Alignment of position angles

We pay particular attention to position angles with respect to the CG and among components to understand the correlation of matter density distributions. Fig. 3.6 plots the correlations of position angles relative to the CG for different components evaluated at $\sqrt{ab} = 0.1$, 0.5, and 1.0 Mpc. If density distributions are aligned with the CG, symbols are expected to be clustered around the origin $(0, 0)$. For all the three components, the position angles are clustered at the origin indicating that these density distributions are well aligned with the major-axis of the CG. At $\sqrt{ab} = 0.1$ Mpc, symbols are more clustered around the origin than at other scales, which indicates that all the components are relatively well aligned in the inner region. The distributions of the alignments relative to

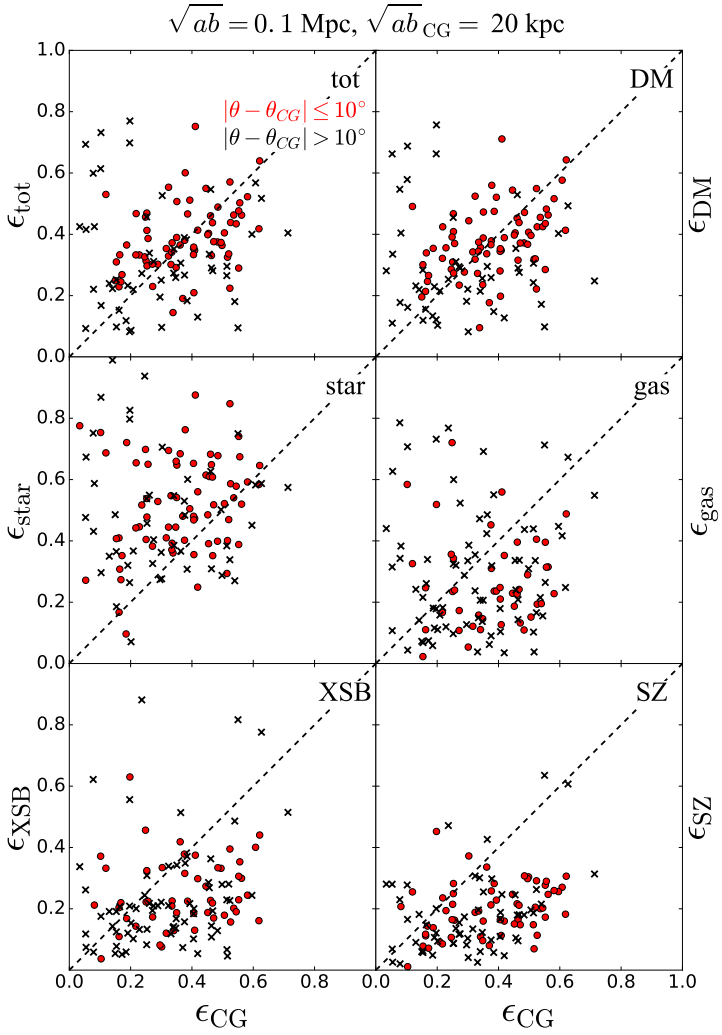

Figure 3.7. Correlation of ellipticities of different components evaluated at $\sqrt{ab} = 0.1$ Mpc against that of the CG. Red and black symbols indicate those with the position angle relative to the CG of $\Delta\theta < 10^\circ$ and $> 10^\circ$, respectively.

the CG is consistent with the result for the cluster described in section 3.2.3. Incidentally, Fig. 3.6 also indicates the alignment of position angles among different components even if outer region where the alignments of position angles relative to the CG are worse. We discuss this point more detail below in section 3.4.2.

3.3.2 Correlation of ellipticities

Since inferring the density distribution of gas from observational data is generally difficult, we also consider XSB and SZ, which are directly observable. For the similar reason, we

also consider total matter density, which can be estimated from lensing analysis.

Fig. 3.7 shows scatter plots for different components evaluated at $\sqrt{ab} = 0.1\,\mathrm{Mpc}$ with that of the CG. There are no tight correlations of ellipticities between these components and the CG. Neither the ellipticities of matter density distribution (DM, star, tot) nor those of gravitational potential shape (gas, XSB, SZ) correlate with that of the CG. This result is inconsistent with a previous work by Soucail *et al.* (2015), they reported tight correlation between ellipticities of BCG and those of light distributions. This discrepancy might be due to difference of method used to estimate ellipticities. They created the light map of galaxy clusters by smoothing light distributions of each member galaxy. Thus, their ellipses are not affected by each galaxy whereas those derived from our tensor method are affected by each galaxy as illustrated in Fig. 3.3.

Ellipticities of stellar components are systematically higher than those of the CG. This is simply due to the other galaxy near the CG. In fact, an ellipse of $\sqrt{ab} = 0.1\,\mathrm{Mpc}$ (the most inner one) in stellar image of Fig. 3.4 is elongated toward a nearby galaxy (bottom left from the CG), which is located along the major-axis of the CG. Fig. 3.6 also indicates that the position angles of stellar component are well aligned with major-axis of the CG in spite of no tight correlation of ellipticities between stellar components and the CG. The alignment suggests member galaxies are preferentially distributed along major-axis of the CG, which is consistent with previous findings (e.g. West, 1994; West *et al.*, 1995; West & Blakeslee, 2000; Brainerd, 2005; Yang *et al.*, 2006; Kang *et al.*, 2007; Azzaro *et al.*, 2007; Faltenbacher *et al.*, 2007; Li *et al.*, 2013; Velliscig *et al.*, 2015b; Huang *et al.*, 2016; L'Huillier *et al.*, 2017; Foëx *et al.*, 2017).

Ellipticities of dark matter and total matter distributions are located around the diagonal line despite with large scatters. The correlations might be affected by two dominant effects; one is the projection effect, and the other is the effect of substructure. The projection effect is explained as follows. While dark matter and total matter distributions are projected by a length of 4.24 Mpc, ellipticities of CG are computed by using only CG particles that extend only $\sim 100\,\mathrm{kpc}$ along the line-of-sight. The projections of such a wide length scale for dark matter and total matter make their shapes of surface densities rounder than those projected only inner part. On the other hand, the existence of substructures, which are located preferentially along the major-axis of the CG, enhances ellipticities as discussed above. As a result of these two competitive effects, ellipticities of dark matter and total matter distributions may be comparable with those of the CG.

Fig. 3.8 plots the correlations among ellipticities of different components evaluated at $\sqrt{ab} = 0.1$, 0.5, and 1.0 Mpc. We find that ellipticities of stellar density distributions are higher, and those of gas are lower than those of dark matter. This result is consistent with that for the cluster explained in section 3.2.3.

The strong correlation between DM and star is simply because each dark matter substructure contains stellar components that correspond to member galaxies in observations. In fact, Fig. 3.4 indicates that there is a substructure both in DM and star at upper right from the centre, and the ellipse is elongated toward the substructure.

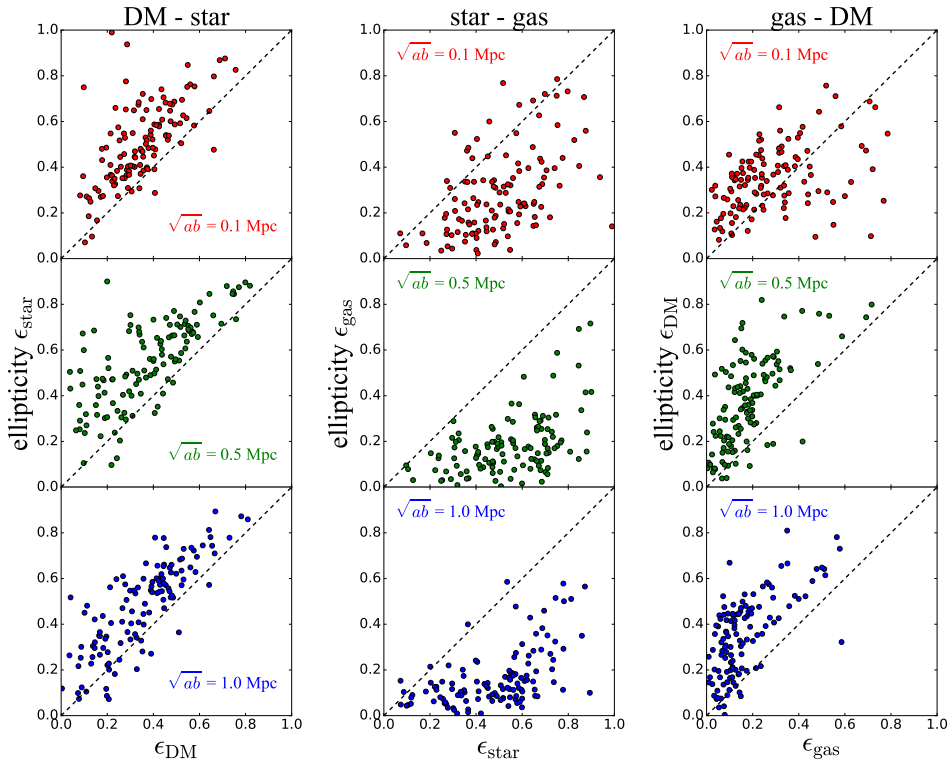

Figure 3.8. Correlations among ellipticities of different components evaluated at $\sqrt{ab} =$ 0.1 (*top*), 0.5 (*middle*), and 1.0 Mpc (*bottom*). Left, middle, and right panels show the correlations between DM and star, star and gas, and gas and DM, respectively.

3.4 Statistics of cluster shape

3.4.1 Histograms of ellipticity and position angle

Fig. 3.9 shows normalized histograms of the ellipticities and position angles relative to the CG. Note that these histograms are computed from $N_{\rm cl} = 120$ clusters (40 different clusters projected along three directions). Clearly the mean value of ellipticity of stellar (gas) distribution is higher (lower) than that of dark matter at all scales. Histograms of ellipticities for XSB and SZ are quite similar to that of gas. This result is consistent with that of Suto *et al.* (2017), although the direct comparison is difficult because of slightly different method used for ellipse fitting. The histograms of position angles are peaked at $\Delta\theta \equiv |\theta - \theta_{\rm CG}| = 0$, implying that all the components are well aligned with the CG as described in section 3.3. The alignments become weaker at large scales. The shape of the histograms is quite similar among all the components, implying that they are aligned

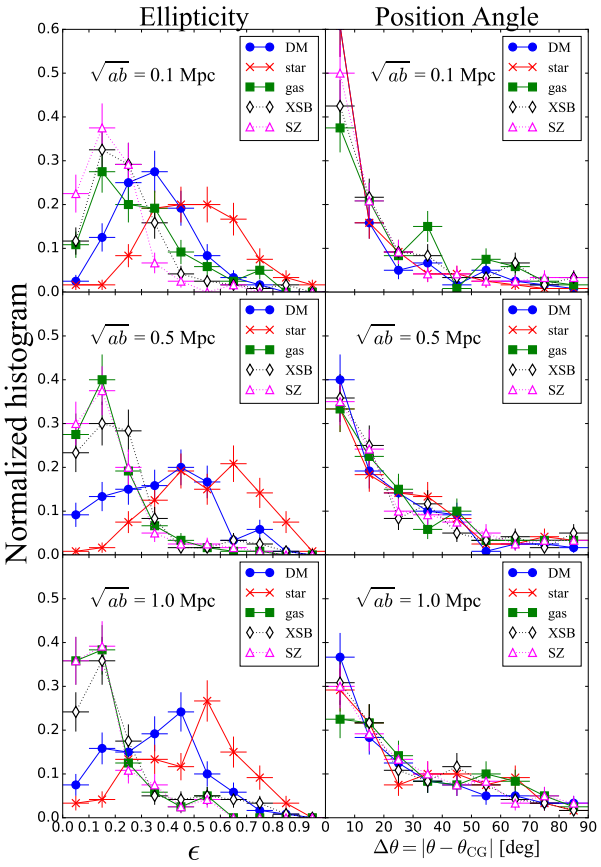

Figure 3.9. Normalized binned distribution functions of ellipticities (*Left*) and position angles relative to the CG (*Right*) for different components, which is computed by dividing the number of clusters in each bin by the total number of clusters $N_{\rm cl} = 120$. Top-, middle-, and bottom panels indicate the results evaluated at $\sqrt{ab} = 0.1$, 0.5, and 1.0 Mpc of the fitted ellipses, respectively. The vertical and horizontal bars associated with each symbol indicate the size of bin and the square root of the number of clusters in each bin (40 different clusters projected along 3 directions).

with each other.

3.4.2 Radial dependence

Fig. 3.10 plots the mean ellipticities of different components against the ellipse scale $\sqrt{ab}$. Ellipticities for each component are almost constant at all scales except for that of gas density distribution, which systematically decreases with increasing $\sqrt{ab}$. This is partly because the position of the CG is sometimes offset from the potential minimum which corresponds to the density peak of gas components. Since we fix the centre to the centre

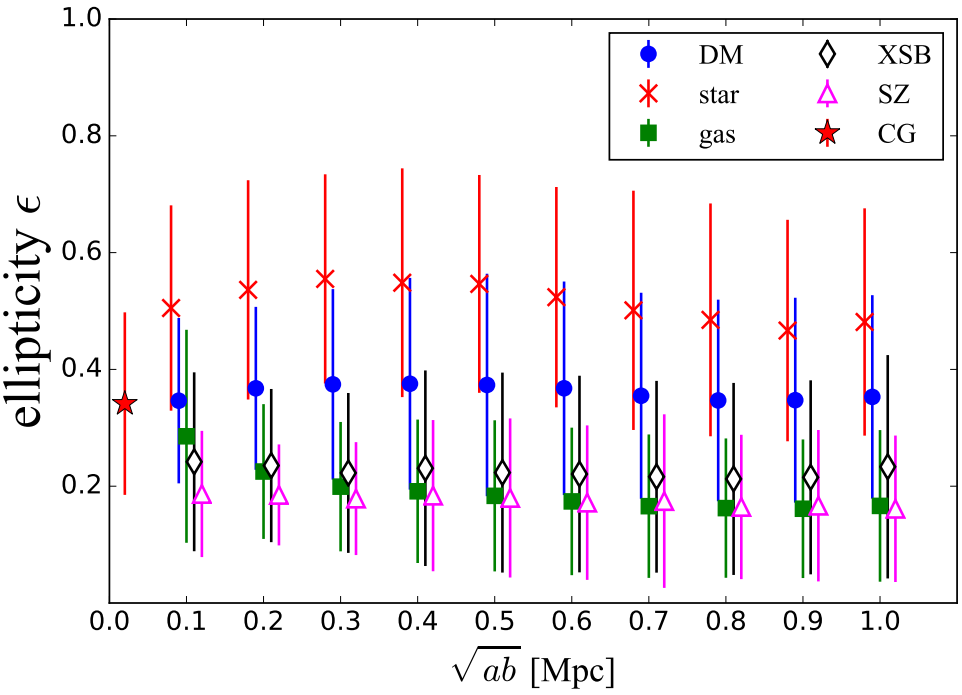

Figure 3.10. The mean ellipticities of different components against $\sqrt{ab}$ of the fitted ellipses. The quoted error-bars indicate the corresponding standard deviation. Symbols of DM (filled circles), star (crosses), XSB (diamonds), and SZ (open triangles) are shifted horizontally by -0.01, -0.02, 0.01, and 0.02 Mpc, respectively just for illustration purpose. A red star symbol at $\sqrt{ab} = 20$ kpc represents a mean value of the ellipticity of the CG.

Table 3.1. Values of mean ellipticities and their errors at $\sqrt{ab} = 0.1$, 0.5, and 1.0 Mpc.

$\sqrt{ab}$	0.1 Mpc	0.5 Mpc	1.0 Mpc
tot	0.36 ± 0.01	0.36 ± 0.02	0.33 ± 0.02
DM	0.35 ± 0.01	0.37 ± 0.02	0.36 ± 0.02
star	0.50 ± 0.02	0.54 ± 0.02	0.48 ± 0.02
gas	0.29 ± 0.02	0.18 ± 0.01	0.17 ± 0.01
XSB	0.23 ± 0.02	0.23 ± 0.02	0.24 ± 0.02
SZ	0.19 ± 0.01	0.18 ± 0.01	0.16 ± 0.01

of mass of the CG, this mis-centring effect causes the elongation of the gas density ellipse at the most inner part toward the direction of gas density peak, resulting in relatively high ellipticities. Nevertheless, we fix the centre to the CG instead of the potential minimum to make it easier to compare our results to those from observations in which the potential minimum is not readily obtained.

In the outer region, ellipticities of XSB are systematically higher than those of gas and SZ. XSB is expressed as the integral of the square of the gas number density, $\int n_{\rm gas}^2 {\rm d}l$,

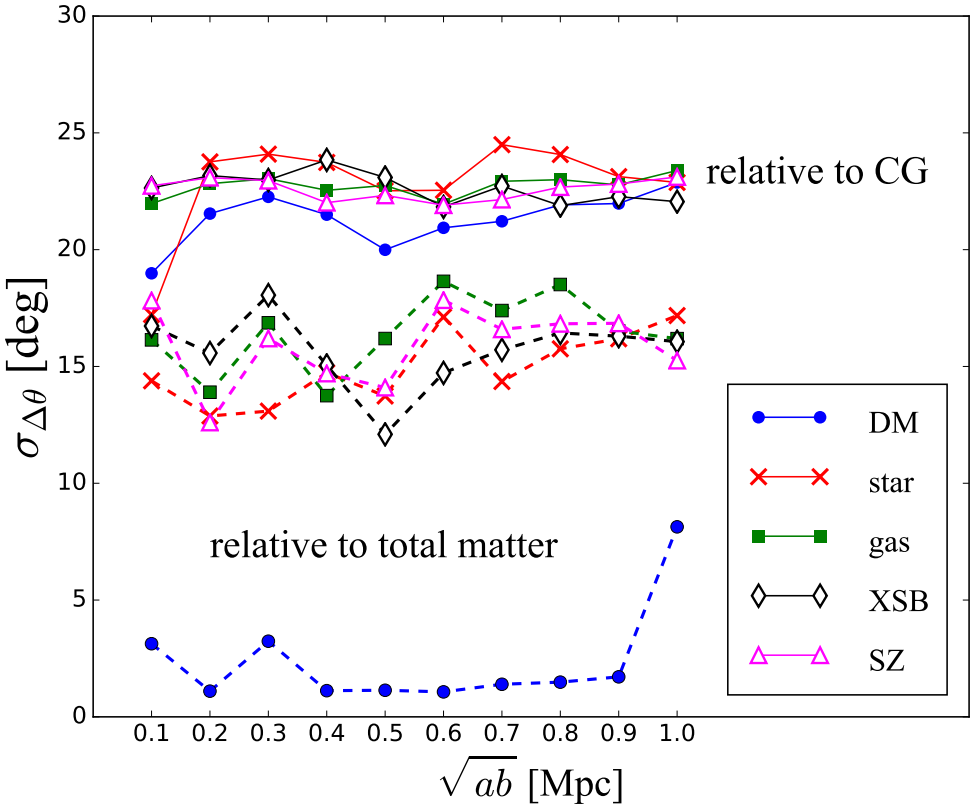

Figure 3.11. The rms of the position angle difference for different components against $\sqrt{ab}$ of the fitted ellipses. Filled circles, crosses, filled squares, open diamonds, and open triangles correspond to the rms values of DM, star, gas, XSB, and SZ, respectively. Solid and dashed lines indicate the rms of position angle relative to the CG and total surface matter density, respectively.

whereas SZ is computed as $\int n_{\rm gas} T_{\rm gas} {\rm d}l$. Since mean ellipticities of gas and SZ are similar to each other for outer regions ($\sqrt{ab} > 0.3\,{\rm Mpc}$), the temperature distribution is not substantially inhomogeneous. Thus, the relatively higher values of XSB ellipticities might be caused by the inhomogeneity of the gas density.

Table 3.1 shows mean values of ellipticities and their errors for DM, star, and XSB. While the quoted error-bars in Fig. 3.10 indicate the standard deviations of ellipticities, the errors in Table 3.1 indicate errors of mean values of ellipticities, which is simply computed by dividing the standard deviations by square root of $N_{\rm cl} = 120$. These values are consistent with those of Suto *et al.* (2017) within error-bars despite the different method to fit the ellipses (see right panel of Fig. 8 in Suto *et al.* 2017). We will compare these values with observations in section 3.5.

Fig. 3.11 shows the rms of position angles relative to the CG computed as

$$\sigma^2_{\Delta\theta,A} \equiv \frac{1}{N_{\rm cl}} \sum_{i=1}^{N_{\rm cl}} (\theta_{A,i} - \theta_{{\rm CG},i})^2. \tag{3.10}$$

If the distribution of position angles relative to the CG is perfectly random, the value of rms is expected to be:

$$\sigma^2_{\Delta\theta,{\rm random}} = \frac{\displaystyle\int_0^{90} \theta^2 {\rm d}\theta}{\displaystyle\int_0^{90} {\rm d}\theta} = \left(90/\sqrt{3}\right)^2 \sim (52^\circ)^2. \tag{3.11}$$

The values of rms for all the components are $20^\circ \leq \sigma_{\Delta\theta} \leq 25^\circ$ and are smaller than 52° at all ellipse scales, indicating that they are well aligned with the major-axis of the CG. For comparison, Schneider *et al.* (2012) studied position angles between the major-axes of dark matter haloes for inner region and outer region based on N-body simulations. They showed the position angles between those computed from the innermost region, 0.1 times virial radius of the host halo $r_{\rm vir}$ and those computed from different scales. A mean value of the position angle is $\sim 20^\circ$ at $r_{\rm vir}$ (see their Fig. 7), which is consistent with our result.

Solid lines in Fig. 3.11 suggest that position angles of the CG are mis-aligned with the other components. Fig. 3.11 also plots the rms of position angles relative to the total matter density distribution by dashed lines. The density distribution of dark matter is very significantly aligned with that of total matter, simply because total matter density distribution is dominated by dark matter distribution. The rms values for the other components are $10^\circ \leq \sigma_{\Delta\theta} \leq 20^\circ$, which are systematically smaller than those relative to the CG. This result indicates that the alignment with the total matter distribution is better than that with the major-axis of the CG.

Stacking analysis is often used to estimate ellipticities of galaxy clusters from weak lensing. In the stacking analysis, a prior information of position angles of matter density distribution is important to reconstruct the shape of clusters. There are two proxies of position angles of matter distributions that are adopted in the literature. One is that of the major-axis of the BCG, and the other is that of the satellite galaxy distribution. Assuming that (i) the CG in the current simulation can be regarded as the BCG in observations, and (ii) stellar mass density distribution in the current simulation matches luminosity distribution of satellite galaxies, our result suggests that the satellite galaxy distribution is a better prior for the stacking analysis than the BCG, at all scales. Although the satellite distribution is a better prior than the BCG, one should keep in mind that there is a non-negligible scatter between position angles of stellar components and total matter distribution, $\sigma_{\Delta\theta} \sim 15^\circ$, which must be taken into account when interpreting the stacking analysis results.

3.5 Comparison with previous observational studies

In this section, we compare the results of the Horizon-AGN with previous observations. While member galaxy distributions are the simplest tracers to estimate the non-sphericities of host DM haloes (e.g. Binggeli, 1982), it is unclear whether they trace well the background DM distributions. The X-ray surface brightness and SZ effect are also used to estimate the non-sphericities of DM haloes (e.g. Hashimoto *et al.*, 2008; Kawahara, 2010). Since some assumptions related to gas state such as hydrostatic equilibrium are adopted, the estimated values depend on the assumptions. We measured the ellipticities and orientations of them in simulated galaxy clusters in previous sections, thus we can directly compare them with observations.

Table 3.2. Values of mean ellipticities and their errors in various observations. SL and WL denotes strong and weak lensing, respectively. For weak lensing, a prior information for the major-axis of a cluster is shown if a stacking analysis is used. $N_{\rm obs}$ denotes the number of galaxy clusters used to estimate values of ellipticities. We also show the range of radii (scale) used to derive the ellipticities for reference.

Reference	Component (prior)	data set	$N_{\rm obs}$	scale	ellipticity
Kawahara (2010)	XSB	XMM-Newton	61	$0.1 - 0.4\ r_{200}$	0.21 ± 0.004
Lau *et al.* (2012)	XSB	Chandra and ROSAT	31	$0.04 - 1\ r_{500}$	0.18 ± 0.05
Evans & Bridle (2009)	WL (member galaxies)	SDSS	4281	$0.5 - 5h^{-1}\,{\rm Mpc}$	$0.52^{+0.09}_{-0.14}$
Richard *et al.* (2010)	SL	HST/Keck	18	$< 250\,{\rm kpc}$	0.30 ± 0.13
Oguri *et al.* (2010)	WL	Subaru/Supreme-Cam	18	$0.1 - 1.5h^{-1}\,{\rm Mpc}$	0.46 ± 0.04
Oguri *et al.* (2012)	SL	SDSS/Subaru	25	$< 100\,{\rm kpc}$	0.38 ± 0.05
Oguri *et al.* (2012)	WL	SDSS/Subaru	25	$0.1 - 3h^{-1}\,{\rm Mpc}$	0.47 ± 0.06
Clampitt & Jain (2016)	WL (BCG)	SDSS	2700	$0.1 - 4h^{-1}\,{\rm Mpc}$	0.19 ± 0.05
Donahue *et al.* (2016)	XSB	Chandra	25	$500\,{\rm kpc}$	0.12 ± 0.06
Donahue *et al.* (2016)	SZ	Bolocam	20	$500\,{\rm kpc}$	0.10 ± 0.06
Donahue *et al.* (2016)	SL/WL	HST	25	$500\,{\rm kpc}$	0.20 ± 0.08
van Uitert *et al.* (2017)	WL (BCG)	GAMA/KiDS	2355	$40 - 250\,{\rm kpc}$	0.55 ± 0.21
van Uitert *et al.* (2017)	WL (BCG)	GAMA/KiDS	2355	$250 - 750\,{\rm kpc}$	0.10 ± 0.23
van Uitert *et al.* (2017)	WL (member galaxies)	GAMA/KiDS	2672	$40 - 250\,{\rm kpc}$	-0.08 ± 0.20
van Uitert *et al.* (2017)	WL (member galaxies)	GAMA/KiDS	2672	$250 - 750\,{\rm kpc}$	0.66 ± 0.23
Shin *et al.* (2018)	star	SDSS	10428	$< 1\,{\rm Mpc}/h$	0.42 ± 0.04
Shin *et al.* (2018)	WL (member galaxies)	SDSS	10428	$0.1 - 2\,{\rm Mpc}/h$	0.45 ± 0.09
Shin *et al.* (2018)	WL (BCG)	SDSS	6681	$0.1 - 2\,{\rm Mpc}/h$	0.23 ± 0.03

3.5.1 Comparison with observations of cluster ellipticities

Table 3.2 summarizes various observations of cluster ellipticities, which should be compared with our results shown in Figure 3.10 and Table 3.1. Below we discuss individual observations listed in Table 3.2.

Kawahara (2010) measured the axis ratios of X-ray surface brightness in the XMM-Newton cluster catalogue compiled by Snowden *et al.* (2008). Note that the method to fit the ellipse for X-ray image is based on Jedrzejewski (1987) and is different from our method. The mean values of axis ratios are 0.78, 0.81, 0.79, and 0.78 at $R = 0.1$, 0.2, 0.3, $0.4r_{200}$, respectively, where R is semi-major axis of ellipses. The mean value of ellipticities $\epsilon = 0.21$ is consistent our result $\epsilon = 0.23 \pm 0.02$ (Table 3.1) within the error-bar.

Lau *et al.* (2012) used clusters observed by Chandra and ROSAT and measured their ellipticities by the tensor method that is similar to our method described in section 3.2.2. They obtained a mean value of ellipticities, $\epsilon = 0.18 \pm 0.05$, for the local relaxed clusters. This value is also consistent with our result $\epsilon = 0.23 \pm 0.02$.

Gravitational lensing is a powerful tool to probe the mass distribution of clusters. The ellipticity has been measured in various studies through both strong and weak lensing methods. Evans & Bridle (2009) analysed 4281 clusters from the catalogue of Koester *et al.* (2007) created from Sloan Digital Sky Survey (SDSS) data. They stacked the weak lensing signals of individual clusters by rotating a cluster to align the major axis of the satellite galaxy distribution. They corrected systematic effects from anisotropic point spread function (PSF) following Bernstein & Jarvis (2002) and Hirata & Seljak (2003). The errors on the shear map were taken into account by

$$\sigma^2_{\gamma_{\rm T}} = \sigma^2_i + \sigma^2_{\rm SN} \tag{3.12}$$

where σ_i includes the shot noise due to the finite number of photons and detector noise, and $\sigma_{\rm SN}$ denotes the shape noise coming from intrinsic variance of galaxy shapes (see their equation 12)

They fitted the stacked signals by an elliptical Navarro *et al.* (1997a) profile and obtain the axis ratio $b/a = 0.48^{+0.14}_{-0.09}$ that corresponds to $\epsilon = 0.52^{+0.09}_{-0.14}$. This ellipticity should be regarded as a lower limit because in stacking they implicitly assumed the perfect alignment between major axis of cluster mass distribution and that of satellite galaxy distribution, which is not the case in our result (see Figure 3.11). Since this misalignment smears out the stacked ellipticity signal, the real value would be slightly larger. Assuming our result $\sigma_{\Delta\theta} = 15^\circ$ as the rms, the ellipticity is expected to be higher by a few percent. Nevertheless, their value of mean ellipticity is consistent with our result $\epsilon = 0.36 \pm 0.02$ (Table 3.1) within an error-bar even if the effect of the misalignment is taken into account.

Richard *et al.* (2010) measured the ellipticities of clusters taken from Local Cluster Structure Survey. They fitted strong lensing data with the elliptical mass distribution using LENSTOOL (Jullo *et al.*, 2007), and obtained averaged ellipticity $\langle \epsilon_{\rm 2D} \rangle = 0.34 \pm 0.14$ in the inner region ($< 250\,$kpc). This value is consistent with our result $\epsilon = 0.36 \pm 0.01$ (Table 3.1), which may imply that the bias described in the paper that strong lensing

clusters are expected to be rounder in the sky is not very strong.

Oguri *et al.* (2010) reported one of the most significant detections of the cluster ellipticity with gravitational lensing at 7σ confidence level. They used weak lensing signals of X-ray luminous clusters from Subaru/Suprime-Cam imaging data (Okabe *et al.*, 2010). They corrected anisotropic PSF following Kaiser *et al.* (1995). They considered both the intrinsic shape noise of galaxies and cosmic shear due to large scale structure. They measured ellipticities for individual clusters without any prior by directly comparing the lensing shear map with elliptical model predictions, and obtained the mean ellipticity $\langle\epsilon\rangle = 0.46 \pm 0.04$. This value is higher than our result of $\epsilon = 0.36 \pm 0.02$, presumably because of the higher cluster masses ($M \sim 10^{15} M_{\odot}$) of these clusters. Many studies suggested that DM haloes with higher masses have higher ellipticities (e.g. Kasun & Evrard, 2005; Paz *et al.*, 2006; Gottlöber & Yepes, 2007; Flores *et al.*, 2007; Despali *et al.*, 2014)

Oguri *et al.* (2012) obtained the similar value of ellipticity $\langle\epsilon\rangle = 0.47 \pm 0.06$ for strong lensing galaxy clusters from SDSS. They took into account anisotropic PSF and noise following Oguri *et al.* (2010). They analysed their weak lensing signals through the stacking analysis by using position angles derived from strong lensing analysis as a prior information. They claimed that this prior enables much more robust stacking analysis than using other priors. This prior is however only available for the strong lensing clusters. They also modeled these clusters by using strong lensing method described in Oguri *et al.* (2009) and Oguri (2010), and found noisy but slightly lower mean ellipticity $\langle\epsilon\rangle = 0.38 \pm 0.05$.

Clampitt & Jain (2016) used the technique to measure the quadrupole weak lensing signal, and applied it to a sample of SDSS clusters. They corrected anisotropic PSF following Reyes *et al.* (2012) and Huff *et al.* (2014). They considered the noise from the intrinsic shape of galaxies and measurement on each background galaxy following Mandelbaum *et al.* (2013) and Sheldon *et al.* (2012). They obtained the best fit value of the mean ellipticity of $\epsilon = 0.19$ with 1σ uncertainty of ~ 0.05. They ascribed this smaller value to the misalignment between major axis of the BCG and that of cluster halo which is implicitly assumed to be aligned. Given the large uncertainty, their result is broadly consistent with our result.

Shin *et al.* (2018) applied the quadrupole technique to SDSS clusters. They estimated anisotropic PSF, measurement noise and noise from the intrinsic shape following Clampitt & Jain (2016). The resulting mean ellipticity value with a prior of the satellite galaxy distribution is $\langle\epsilon\rangle = 0.45 \pm 0.09$ after correcting for Poisson sampling. They also measured the ellipticity of satellite galaxy distribution as $\langle\epsilon\rangle = 0.42 \pm 0.04$, and that derived from stacked weak lensing with a prior of the CG major axis as $\langle\epsilon\rangle = 0.25 \pm 0.06$. By comparing these ellipticity values, they also estimated the rms misalignment angle of 30° between the CG and DM halo and 18° between satellite galaxies and DM halo. These misalignment values are in good agreement with our result (see also section 3.5.2).

van Uitert *et al.* (2017) used an estimator similar to Clampitt & Jain (2016) and constrained the average ellipticity of galaxy groups obtained from Galaxy And Mass Assembly (GAMA) survey combined with the weak lensing signal measured by Hildebrandt *et al.* (2017) from the Kilo Degree Survey (KiDS). They did not consider anisotropic PSF but

consider the intrinsic shape noise. They compared different priors for stacking analysis of weak lensing signals at different scales. Their resulting values of the mean ellipticity are $\epsilon = 0.38 \pm 0.12$ ($40\,\mathrm{kpc} < R < 250\,\mathrm{kpc}$) and $\epsilon = 0.05 \pm 0.13$ ($250\,\mathrm{kpc} < R < 750\,\mathrm{kpc}$) for the BCG prior, whereas $\epsilon = -0.04 \pm 0.11$ and $\epsilon = 0.349 \pm 0.13$, respectively for the prior of the satellite galaxy distribution. They concluded that the BCG major-axis (satellite galaxy distribution) is aligned (misaligned) with the DM halo orientation on small scales ($< 250\,\mathrm{kpc}$) whereas the BCG major-axis (satellite galaxy distribution) is misaligned (aligned) with DM on large scales ($> 250\,\mathrm{kpc}$). This result appears to be inconsistent with our result which indicates that the distribution of satellite galaxies is aligned better than the major-axis of the CG at *all* scales, $100 - 1000\,\mathrm{kpc}$. This discrepancies are partly because they use galaxy groups with $M_{200} \sim 10^{13} M_{\odot}$ rather than cluster-sized haloes in the Horizon-AGN simulation, $M_{200} \sim 10^{14} M_{\odot}$. Nevertheless, further work is needed to explain this inconsistency, for example by analyzing the galaxy groups with masses of $M_{200} \sim 10^{13} M_{\odot}$ in the Horizon-AGN simulation.

Umetsu *et al.* (2018) estimates the median projected axis ratio of 0.67 ± 0.07, corresponding $\epsilon = 0.33 \pm 0.07$. The median value is lower than our resulting value $\epsilon = 0.36 \pm 0.02$ (see Table 3.1) due to selection effect. This result is not unnatural because they select the CLASH clusters which have circular shapes in X-ray as also discussed in section 3.5.1. They also evaluate the misalignment angles of baryonic components (X-ray, thermal Sunyaev-Zel'dovich effect, brightest cluster galaxy) with respect to the weak lensing. They conclude that the major-axis of X-ray shows best aligned with mass distribution derived from weak lensing with a median misalignment angle of $21^{\circ} \pm 7^{\circ}$ (see their Fig. 6). This result is quantitatively consistent with our result which indicates X-ray is aligned better than brightest cluster galaxy with respect to total mass distribution. The worse alignment of thermal SZ effect with respect to the total mass distribution might be due to large PSF of Bolocam images.

Donahue *et al.* (2016) systematically measured the ellipticities of X-ray surface brightness, Sunyaev-Zel'dovich effect (SZE), gravitational lensing map, and the BCG for clusters from Cluster Lensing and Supernova survey with Hubble Space Telescope (CLASH). They used X-ray data from *Chandra X-ray Observatory* and measured the axis ratio based on the procedure described in Donahue *et al.* (2015). The method is almost the same as the one we used (see section 3.2.2). The same procedure was applied to the SZ Compton y-parameter map obtained from the Bolocam SZ images (see Sayers *et al.*, 2013; Czakon *et al.*, 2015). They found the mean axis ratios 0.09 ± 0.05 and 0.1 ± 0.06 for XSB and SZ, respectively at scales of $500\,\mathrm{kpc}$. These values are much lower than our results, which is not surprising because their clusters were selected to be nearly circular in X-ray. They also measured the ellipticity of gravitational lensing surface mass density map created from both strong and weak lensing. The detail of the lensing analysis is described in Zitrin *et al.* (2015). The resulting mean ellipticity value is 0.2 ± 0.08 at $500\,\mathrm{kpc}$, and is also lower than our result ($\epsilon = 0.36 \pm 0.02$) probably due to the selection effect.

Strictly speaking, the observational ellipticities derived from lensing analysis are not exactly the same as those of total matter distributions in the simulation since observable

in the lensing is shear signals whereas the total matter distributions correspond to the convergence signals. In addition, observations have various systematics such as Poisson noise of background galaxies, intrinsic alignment, and contamination of point spread function. The most straightforward way to compare our results with these observations is to create mock shear catalogue and evaluate the ellipticities by adopting the same lensing method. Such analysis is beyond the scope of this thesis, and will be presented elsewhere.

3.5.2 Comparison with observed position angle distributions

In this subsection, we regard the CG of the simulation as the BCG in observations, since the CG is supposed to be almost identical to the observed BCG as described in section 3.1.

Figure 3.12 compares normalized histograms of position angles between two components from the Horizon-AGN simulation with observations. The observational data are based on position angles of the BCG from Donahue *et al.* (2015), those of XSB, SZ, and tot from Donahue *et al.* (2016), and those of stellar distribution from West *et al.* (2017). We choose 25 clusters in Donahue *et al.* (2016) (see their Table 1 and Figure 1). Twenty of these clusters were selected based on their relatively round X-ray shape and with prominent BCG at their centre being well aligned with X-ray. For these 20 clusters, Donahue *et al.* (2015) measured the position angles of BCGs by using the surface brightness weighted tensor method. They obtained the position angles for both ultraviolet and near-infrared data. We use those derived from near-infrared data because near-infrared light is dominated by old stars which is expected to dominate the mass in the centre of BCG. The values are summarized in Table 3 in Donahue *et al.* (2015). Donahue *et al.* (2016) measured the position angles of XSB and SZ by using the same method as Donahue *et al.* (2015), and those of total matter distributions by utilizing the otherwise identical procedures for lensing-based surface mass density maps. We use their values estimated within 500 kpc. The values for XSB, SZ, and tot are summarized in Table 3, 6, and 5 in Donahue *et al.* (2016), respectively. West *et al.* (2017) measured position angles of the member galaxy distribution by computing the moments of inertia of the red sequence galaxy distribution. Table 1 in West *et al.* (2017) summarizes the resulting values.

We compare position angle between these components (10 combinations for 5 different components mentioned above) with our result shown in Figure 3.9. We use our measurement at 500 kpc following Donahue *et al.* (2016). Figure 3.12 shows the resulting p-values of the Kolmogorov-Smirnov test. We find that histograms from the simulation generally agree well with observations, except for those related to SZ. One of the reason of the low p-values related to the SZ is the poor angular resolution of Bolocam with a full width half maximum of $58''$, which makes measurement of the position angles for the SZ maps very noisy. The observed distribution would be more consistent with our simulation result once the measurement errors of the position angles are taken into account.

The relatively lower p-values related to the stellar distributions are partly because there are not sufficient numbers of member galaxies, and therefore Poisson noise affects the position angle measurement. To draw more robust conclusion, we have to take into account of selection effects and differences in measurement methods. Nevertheless, broad agree-

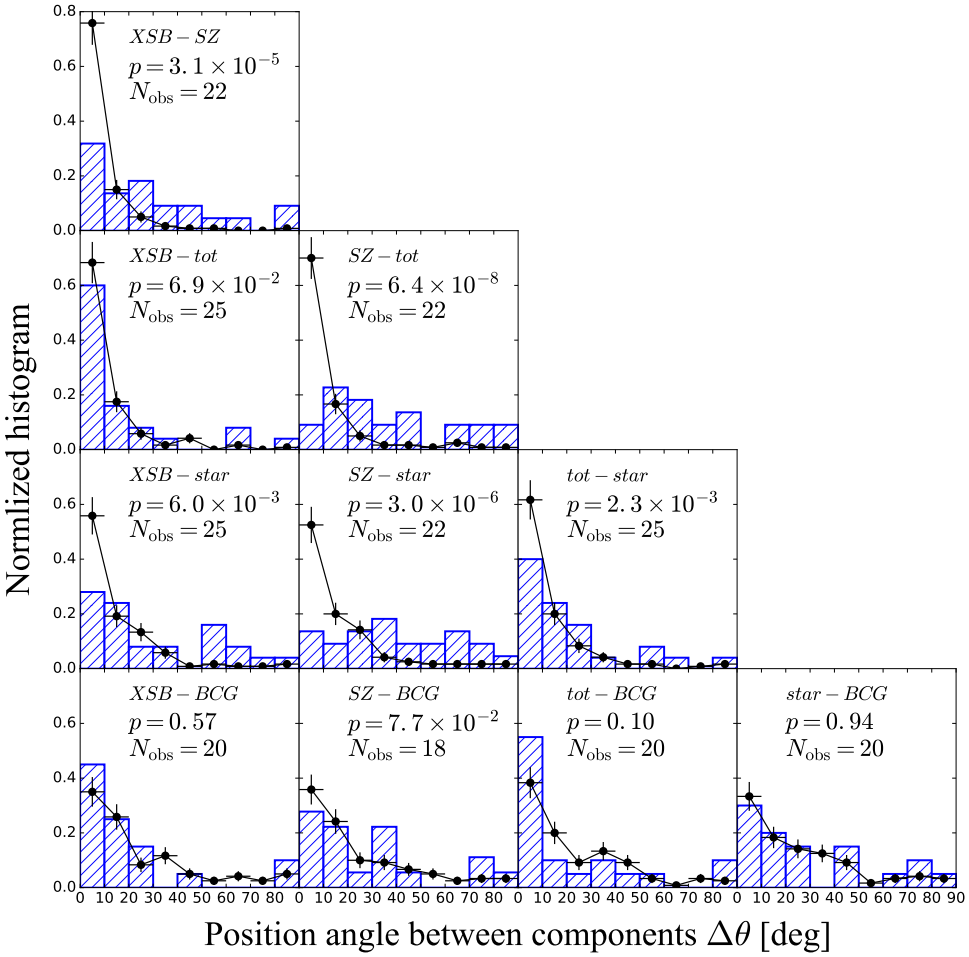

Figure 3.12. Comparison of observed distribution of relative position angles of different components against our simulated data. Blue hatched histograms and black symbols are normalized histograms of relative position angles in observations and our simulation, respectively. $N_{\rm obs}$ indicates number of galaxy clusters which both components are available to estimate position angles, and p denotes p-values of the Kolmogorov-Smirnov test.

ments between the simulation and the observations are encouraging, which invites more careful analysis of observational data based on our simulation results.

3.5.3 Comparison with other simulations

While Chisari *et al.* (2017) focused on the three-dimensional alignment angle between galaxies and their host DM haloes, they also calculated projected shapes for galaxies in Horizon-AGN simulation and matched DM haloes in Horizon-DM simulation. They

compared the major axises of galaxies in Horizon-AGN simulation and those of matched DM haloes in Horizon-DM simulation and derived the alignment angle distribution (see their Figure B1). They obtained a mean alignment angle and dispersion of $-2^\circ \pm 48^\circ$, which is marginally consistent with our result of $5^\circ \pm 30^\circ$ (Figure 3.9) though both galaxies and host DM haloes in our analysis are in Horizon-AGN simulation. Tenneti *et al.* (2015) analysed the shapes and position angles of stellar and DM haloes in the MassiveBlack-II simulation, which is a cosmological hydrodynamical simulation including stellar and AGN feedback in a volume of $(100h^{-1}\mathrm{Mpc})^3$ comparable to that of the current Horizon simulation. They obtained a mean projected position angle between galaxies and DM haloes of 11° (see their Table 2), which is smaller than our result of 21° (Figure 3.9). The detailed comparison, however, is difficult since different method is used to derive the position angles. Velliscig *et al.* (2015a) reported the shapes and position angles of dark matter, stellar, and gas components in the EAGLE (Schaye *et al.*, 2015) and cosmo-OWLS (Le Brun *et al.*, 2014) simulations, which are smoothed particle hydrodynamics simulations (Monaghan, 1992). They obtained median position angles between stellar and total matter components of $10^\circ - 25^\circ$ (see their Figure 13), which is consistent with our result of 10° (Figure 3.9).

3.6 Summary

In this chapter, we characterize the projected non-sphericities and orientations of dark matter (DM), stellar, and gas, mass distributions, X-ray surface brightness, and Sunyaev-Zel'dovich (SZ) effect in 40 cluster-sized haloes with mass larger than $5\times10^{13}M_\odot$ extracted from the cosmological hydrodynamical simulation, the Horizon-AGN simulation. Since high resolution of the Horizon-AGN simulation enables us to identify galaxies, we also evaluate the non-sphericities and orientations of central galaxies (CGs), which can be regarded as brightest cluster galaxies in observations. We fit shapes of the projected images at different scales as ellipses, with two parameters of ellipticity $e \equiv 1 - b/a$ and position angle θ, where a and b denote the semi-major and -minor axes, respectively.

We first compare the ellipticities of mass distributions of DM, stellar, and gas which are fundamental components of the simulation. Mean values of ellipticities are 0.37 ± 0.02 (DM), 0.54 ± 0.02 (star), 0.18 ± 0.01 (gas) at a fiducial ellipse scale of $\sqrt{ab} = 0.5$ Mpc, and 0.34 ± 0.01 (CGs) at $\sqrt{ab} = 20$ kpc. The mean values of each component are almost independent of the scales from 0.1 to 1 Mpc, except for the most inner regions of gas components, which is simply due to miscentring from the CGs.

We check the correlations between ellipticities of distributions of DM, stellar, and gas components relative to those of CGs and find that ellipticities of all the three components are not correlated with those of CGs even if the position angles are fairly aligned with each other $|\theta - \theta_{\mathrm{CG}}| \leq 10$ deg, where θ and θ_{CG} are position angles of each component and CGs, respectively. We then compute the ellipticities of X-ray surface brightness and SZ effect, and obtain mean values of 0.23 ± 0.02 and 0.18 ± 0.01, respectively at the fiducial scale of $\sqrt{ab} = 0.5$ Mpc.

We measure the position angels of those components relative to those of CGs, obtain the root mean square (rms) values of, $\sigma_{\Delta\theta} \equiv (\langle|\theta - \theta_{\rm CG}|^2\rangle)^{1/2} = 20 - 25$ deg, for all the components and all the scales. We also compare the position angles of those components relative to total matter distributions instead of CGs, and find tighter correlations with the rms values of $1 - 2$ deg for DM, and $10 - 20$ deg for other components.

The rounder shapes of gas distributions than DM and stellar components are qualitatively consistent with the theoretical predictions with the assumption that gases are in hydrostatic equilibrium (e.g. Lee & Suto, 2003). The distributions of stellar components are more elongated than those of DM in galaxy cluster scales ~ 1 Mpc in the simulation. This result calls to caution that ellipticities estimated by the distributions of member galaxies may overestimate those of DM haloes. This prediction of the ΛCDM model can be tested by comparing ellipticities of member galaxy distributions with those of DM haloes measured by gravitational lensing. The similar mean ellipticity values of CGs and DM distributions despite the no correlation between them are also consequence of the ΛCDM model, and further discussions by comparing with observations are given in chapter 4.

The tighter alignments between distributions of stellar or gas components and those of total matter than those of CGs indicate that major-axes of the member galaxy distributions, and those of X-ray surface brightness or SZ effect if available, can be better priors for the stacking analysis of weak lensing than those of CGs. Our result indicates that alignments are never perfect, and thus the differences between orientations of these priors and DM haloes should be taken into account to correctly interpret the elliptical signals of weak lensing from stacking analysis.

The result that orientations of stellar components show tighter alignments than those of CGs relative to total mass distributions at *all* scales, $100 - 1000$ kpc, appears to be inconsistent with the result of observation by van Uitert *et al.* (2017). They found that the CGs are aligned tighter with mass distributions in the inner regions, < 250 kpc, while member galaxy distributions show tighter alignments in the outer regions, > 250 kpc. Since this discrepancy might be simply due to differences of mass scales or adopted methodologies, further improvements in both observation and simulations are required.

In section 3.5, we compare ellipticities of cluster sized haloes in the Horizon-AGN simulation with those of observed values. The mean values of ellipticities of DM distribution in the simulation are marginally consistent with those of galaxy clusters measured by the lensing method within the standard deviation. However, the mean values of the observed ellipticities are slightly higher than those in the simulation. This might be due to the difference of mass scales between observed clusters and our halo sample, bias in methodology we adopt, or sample selection bias in the observations. We will discuss the mass dependence of ellipticities in chapter 4

Since the baryon components are fully implemented in the Horizon-AGN simulation, we can directly compare various tracers such as member galaxy distribution, X-ray surface brightness, and the Compton y-parameter of Sunyaev-Zel'dovich effect as well as the DM distribution with observations. The resulting values in the simulation show good

agreement with observed values.

In addition to the ellipticities, we compare alignment angels among DM, stellar, and gas component in the clusters with observations. We use observed position angles measured by Donahue *et al.* (2015) for BCGs, Donahue *et al.* (2016) for XSB, SZ, and lensing, and West *et al.* (2017) for member galaxy distributions. We compare them with our results to find that alignment angles among those are in good agreement with those in the simulation except for the angles related to the SZ whose angular resolution is very poor. Both ellipticities and alignment angles in the simulation show good agreement with those of observations, supporting the ΛCDM model.

Chapter 4

New observations from strong lensing clusters and comparisons with simulations

Gravitational lensing is a powerful tool to measure shapes of mass distributions directly. In fact, a number of studies measured the non-sphericities by using weak lensing method both for individual haloes (e.g. Oguri *et al.*, 2010; Umetsu *et al.*, 2018) and for stacked lensing signals (e.g. van Uitert *et al.*, 2017; Shin *et al.*, 2018). However, weak lensing for individual haloes suffers from their large errors due to intrinsic galaxy shapes, and that for stacked signals underestimate the mean ellipticities due to mis-alignments between *a priori* directions in stacking and their true orientations.

Strong lensing can evaluate the non-sphericities of DM haloes with much less errors than those estimated by weak lensing. Oguri *et al.* (2012) actually measure the ellipticities of galaxy clusters and show that their errors are considerably small, but their sample size is relatively limited, $N = 20$.

Although some studies measure the shape of mass distribution of individual galaxy clusters by using weak or strong lensing method (e.g. Richard *et al.*, 2010; Oguri *et al.*, 2010, 2012; Umetsu *et al.*, 2018), their results are somewhat noisy or insufficient in sample sizes. Thus, we provide a new measurement of shapes and orientations of galaxy clusters by strong lensing. Since recently three survey data of Hubble Space Telescope are available, we extend Oguri *et al.* (2012) to measure the ellipticities of 45 cluster-sized haloes by strong lensing. In addition, we also measure the shapes of their BCGs to compare the ellipticities and orientations of them with those of host haloes. In this chapter, we show results of these measurements and compare them with the Horizon-AGN simulation.

4.1 Cluster sample: HFF, CLASH, and RELICS

In this section, we describe how to measure ellipticities and orientations of galaxy clusters, all of which are observed with the Hubble Space Telescope (HST). We use three survey

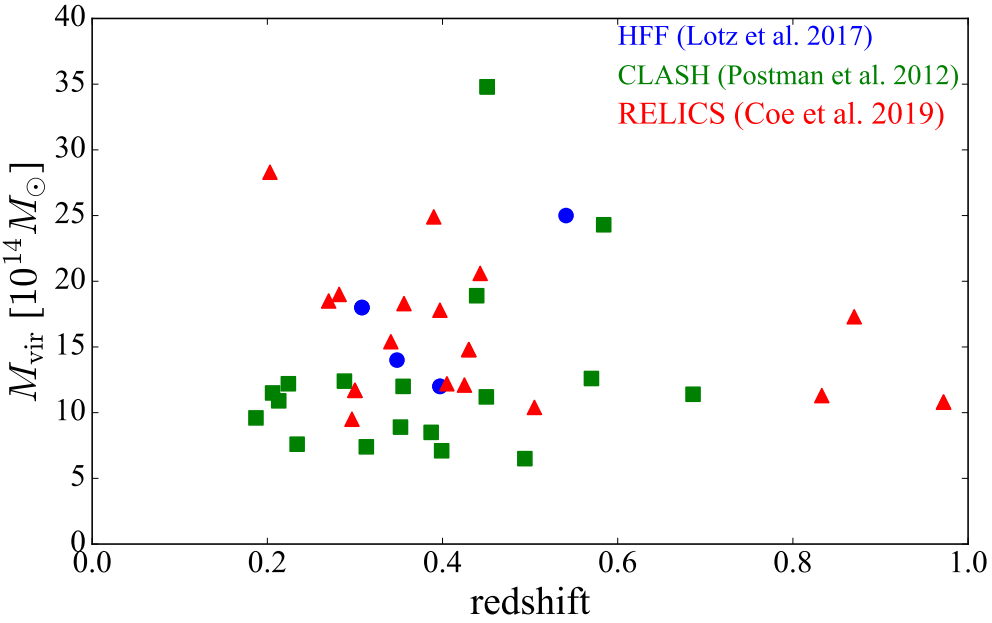

Figure 4.1. Virial masses and redshifts of clusters in our sample. Blue circles, green squares, and red triangles show clusters observed by HFF, CLASH, and RELICS, respectively.

data to construct our galaxy cluster sample: Hubble Frontier Field [*1] (HFF), Cluster Lensing And Supernova survey with Hubble [*2] (CLASH), and Reionization Lensing Cluster Survey [*3] (RELICS). From the three survey data, we select 39 galaxy clusters whose shapes are measured by strong lensing.

Table 4.1 summarizes properties of the galaxy cluster sample. The M_{14} means virial mass divided by $1 \times 10^{14} M_\odot$. The cluster names and cluster redshifts are shown following their overview papers; HFF (Lotz *et al.*, 2017), CLASH (Postman *et al.*, 2012), and RELICS Coe *et al.* (2019). We compute their virial masses as follows. For HFF, we use $M_{\rm vir}$ shown in Table 2 of Lotz *et al.* (2017). For CLASH, first we convert the X-ray temperature shown in Table 4 of Postman *et al.* (2012) to M_{500} by using an empirical relation (Arnaud *et al.*, 2007). We then obtain $M_{\rm vir}$ from M_{500} by assuming the NFW profile and assuming the concentration parameter of $c_{500} = 2.5$. For RELICS, we use Planck SZ inferred mass M_{500} shown in Table 2 of Coe *et al.* (2019) and convert them to $M_{\rm vir}$ by assuming the NFW profile and $c_{500} = 2.5$. Figure 4.1 summarizes virial masses and redshifts of galaxy clusters in our sample.

[*1] https://archive.stsci.edu/prepds/frontier/
[*2] https://archive.stsci.edu/prepds/clash/
[*3] https://archive.stsci.edu/prepds/relics/

4.2 Ellipticities and position angles of DM halo by strong lensing

We compare shapes of BCGs with those of dark matter distributions measured with strong lensing. Short descriptions of strong lens mass modeling for our cluster sample are given in Appendix B. In short, we use the software GLAFIC (Oguri, 2010) for mass modeling, and reconstruct the mass distribution of each cluster assuming a parametric mass model that includes dark matter halo components modeled by an elliptical Navarro *et al.* (1997b, hereafter NFW) profile as well as cluster member galaxy components modeled by an elliptical pseudo-Jaffe profile. More specifically, we introduce an ellipticity $e_{\rm SL}$ to the NFW profile simply by defining the convergence κ as

$$\kappa(x,y) = \kappa_{\rm NFW}\left(r = \sqrt{\frac{x^2}{1-e_{\rm SL}} + (1-e_{\rm SL})y^2}\right), \tag{4.1}$$

where $\kappa_{\rm NFW}$ is the convergence profile of a spherical NFW profile (e.g., Bartelmann, 1996) and x and y are coordinates aligned with minor and major axes of the ellipse. Therefore our definition of the ellipticity is $e = 1 - a/b$, where a and b are minor and major axis lengths of the ellipse. An additional model parameter for the elliptical NFW profile is the position angle $\theta_{\rm SL}$. In what follows we refer to the position angle as the polar angle of the major axis measured East of North.

The precision and accuracy of strong lens mass modeling depends on the quality of strong lensing data, such as the number of multiple images and the availability of spectroscopic redshifts for them. In order to obtain reliable measurements, we limit our analysis to clusters with three or more sets of multiple images. Since we are interested in comparing shapes of dark matter distributions with those of BCGs, for each halo component we need to identify the corresponding BCG, which we define as a bright cluster member galaxy located near the center of a halo component. We remove clusters if identifications of BCGs are not secure due to e.g., large offsets between halo components and putative BCGs or no obvious bright galaxies near halo centers. Such situation can be seen in complex merging clusters such as MACSJ0717.5+3745 in HFF. Clusters listed in Table 4.1 and Appendix B are those after these selections are applied.

In some of the 39 clusters in our cluster sample, there are more than one prominent halo components. If their model parameters are well constrained by strong lensing data and bright central galaxies are securely identified for them, we include multiple halo components from a single cluster separately in our analysis. Since there are 6 clusters with two massive haloes, we measure the shape of 45 haloes in total.

4.3 Ellipticities and position angles of BCGs

We measure shapes of 45 BCGs at the center of DM haloes whose shapes are measured by strong lensing. For all the BCGs, we use HST images in F814W band to measure their shapes. We calculate ellipticities and position angles by using tensor method described in

section 3.2. We use surface brightness as weight of the tensor and fit the ellipse at $\sqrt{ab} =$ 10, 20, and 30 pkpc. The choice of the $\sqrt{ab}$ is somewhat arbitrary but corresponding to typical scales of BCGs. While we measure ellipticities at the three scales in order to discuss the effect of satellite galaxies around the BCGs because we do not remove them in the ellipse fit procedure, we adopt 20 pkpc as a fiducial scale according to section 3.2. The average size of point spread function (PSF) of the HST images $\sim$ 97 milliarcseconds (e.g. Scoville *et al.*, 2007; Koekemoer *et al.*, 2007), corresponding to physical scale of $\sim$ 500 pc at the mean redshift of clusters $\langle z \rangle \sim 0.4$, are much smaller than the ellipse scales, and thus the effect PSF can be safely ignored in the ellipse fit procedure.

Figure 4.2 shows the HST images of F814W band and fitted ellipse shapes for examples of single peak and double peak clusters. The ellipse scales of DM haloes in the figures are Einstein radii computed by assuming the source redshift $z_s = 3.0$ which roughly corresponds to the typical scale probed by strong lensing method. Table 4.2 and 4.3 summarize the derived ellipticities and position angles of DM haloes and BCGs.

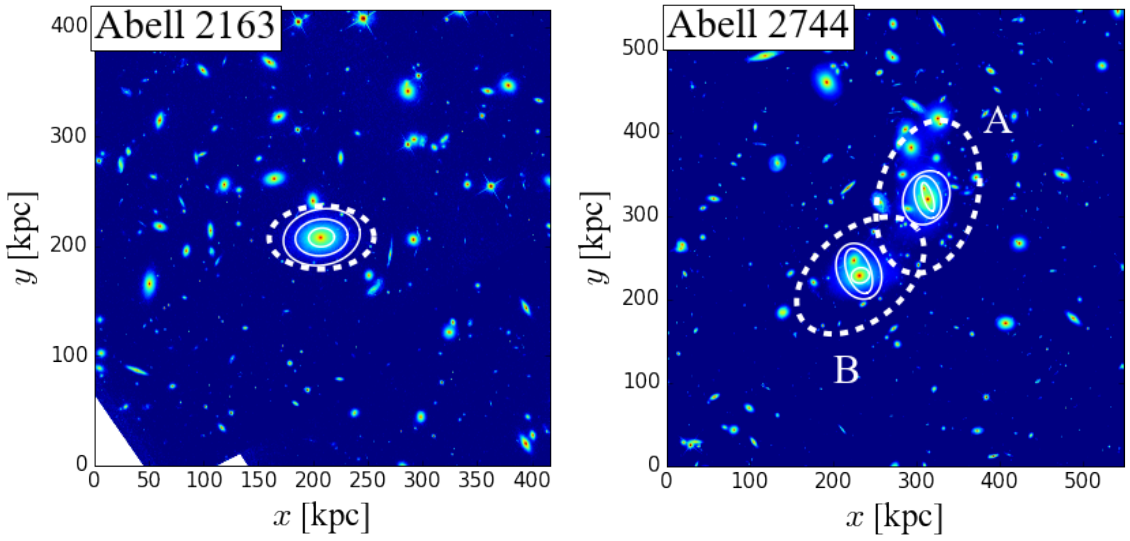

Figure 4.2. Left: An HST image of Abell 2163 in F814W band. Black and white lines correspond to fitted ellipses of BCGs at $R_{ab} = 10$, 20, and 30 pkpc and that of DM halo derived by strong lensing, respectively. The scale of DM halo is the Einstein radius with source redshift $z_s = 3.0$. Right: Similar to left panel, but for the double peak cluster Abell 2744.

Table 4.1. Properties of our cluster sample. M_{14} means virial mass of each cluster divided by $1 \times 10^{14} M_{\odot}$.

survey	cluster name	z	M_{14}
HFF	Abell 2744	0.308	18.0
HFF	MACS0416.1−2403	0.3971	12.0
HFF	MACS1149.5+2223	0.541	25.0
HFF	Abell S1063	0.348	14.0
CLASH	Abell 209	0.206	11.5
CLASH	Abell 383	0.187	9.6
CLASH	MACS0329.7−0211	0.45	11.2
CLASH	MACS0429.6−0253	0.399	7.1
CLASH	MACS0744.9+3927	0.686	11.4
CLASH	Abell 611	0.288	12.4
CLASH	MACS1115.9+0129	0.355	12.0
CLASH	Abell 1423	0.213	10.9
CLASH	MACS1206.2−0847	0.439	18.9
CLASH	MACS1311.0−0310	0.494	6.5
CLASH	RXJ1347.5−1145	0.451	34.8
CLASH	MACS1720.3+3536	0.387	8.5
CLASH	Abell 2261	0.224	12.2
CLASH	MACS1931.8−2635	0.352	8.9
CLASH	RXJ2129.7+0005	0.234	7.6
CLASH	MS 2137−2353	0.313	7.4
CLASH	MACS0647.7+7015	0.584	24.3
CLASH	MACS2129.4−0741	0.57	12.6
RELICS	Abell 2163	0.203	28.3
RELICS	Abell 2537	0.2966	9.5
RELICS	Abell 3192	0.425	12.1
RELICS	Abell 697	0.282	19.0
RELICS	Abell S295	0.3	11.7
RELICS	ACT-CL J0102-49151	0.87	17.3
RELICS	CL J0152.7-1357	0.833	11.3
RELICS	MACS J0159.8-0849	0.405	12.2
RELICS	MACS J0257.1-2325	0.5049	10.4
RELICS	MACS J0308.9+2645	0.356	18.3
RELICS	MACSJ0417.5-1154	0.443	20.6
RELICS	MACS J0553.4-3342	0.43	14.8
RELICS	PLCK G171.9-40.7	0.27	18.5
RELICS	PLCK G287.0+32.9	0.39	24.9
RELICS	RXC J0142.9+4438	0.341	15.4
RELICS	RXC J2211.7-0350	0.397	17.8
RELICS	SPT-CL J0615-5746	0.972	10.8

Table 4.2. Properties of BCGs and measured value of ellipticities and position angles of BCGs and their host DM haloes. The symbols $e_{\rm BCG}^{R_{ab}}$ and $\theta_{\rm BCG}^{R_{ab}}$ denote the ellipticities and position angles of BCGs at scale of R_{ab}, and $e_{\rm SL}$ and $\theta_{\rm SL}$ are those of DM haloes.

survey	BCG name	ra	dec	$e_{\rm BCG}^{10}$	$\theta_{\rm BCG}^{10}$	$e_{\rm BCG}^{20}$	$\theta_{\rm BCG}^{20}$	$e_{\rm BCG}^{30}$	$\theta_{\rm BCG}^{30}$	$e_{\rm SL}$	$\theta_{\rm SL}$
HFF	Abell 2744 A	3.5862553	−30.4001723	0.686	18.1	0.404	14.52	0.193	−25.93	$0.365^{+0.031}_{-0.028}$	$-14.95^{+4.04}_{-2.88}$
HFF	Abell 2744 B	3.5920369	−30.405741	0.165	−76.09	0.498	20.54	0.252	23.31	$0.379^{+0.021}_{-0.024}$	$-50.58^{+1.79}_{-2.02}$
HFF	MACS0416.1−2403 A	64.0380978	−24.0674837	0.214	55.66	0.339	52.15	0.409	37.03	$0.661^{+0.009}_{-0.01}$	$60.58^{+0.65}_{-1.07}$
HFF	MACS0416.1−2403 B	64.0436968	−24.0729844	0.214	76.19	0.494	40.31	0.415	40.61	$0.693^{+0.017}_{-0.017}$	$42.92^{+0.97}_{-1.1}$
HFF	MACS1149.5+2223	177.3987502	22.3985322	0.256	7.94	0.303	−52.27	0.657	−42.83	$0.493^{+0.021}_{-0.018}$	$-53.63^{+1.3}_{-1.28}$
HFF	Abell S1063	342.1832095	−44.5308829	0.204	−13.69	0.297	30.9	0.27	47.1	$0.454^{+0.011}_{-0.011}$	$53.38^{+0.33}_{-0.35}$
CLASH	Abell 209	22.9689565	−13.6112333	0.203	−43.94	0.361	−28.08	0.227	−38.59	$0.71^{+0.063}_{-0.159}$	$309.5^{+3.69}_{-4.11}$
CLASH	Abell 383	42.0140947	−3.5292113	0.128	13.43	0.105	16.51	0.319	74.11	$0.216^{+0.059}_{-0.039}$	$13.8^{+2.42}_{-3.78}$
CLASH	MACS0329.7−0211	52.4232222	−2.1962171	0.175	−49.94	0.184	−28.5	0.226	−37.02	$0.25^{+0.051}_{-0.044}$	$-17.35^{+10.59}_{-6.71}$
CLASH	MACS0429.6−0253	67.4000333	−2.8851685	0.274	8.55	0.316	−5.0	0.367	0.92	$0.462^{+0.055}_{-0.062}$	$-9.72^{+0.64}_{-0.62}$
CLASH	MACS0744.9+3927	116.2199938	39.4574046	0.161	15.79	0.331	21.01	0.274	19.14	$0.073^{+0.063}_{-0.042}$	$-47.64^{+18.88}_{-18.75}$
CLASH	Abell 611	120.2367241	36.0565643	0.174	40.54	0.291	31.97	0.56	21.21	$0.257^{+0.025}_{-0.023}$	$41.06^{+0.92}_{-1.08}$
CLASH	MACS1115.9+0129	168.9662572	1.4986333	0.256	−35.92	0.381	−35.21	0.318	−39.44	$0.607^{+0.066}_{-0.073}$	$142.51^{+1.17}_{-1.32}$
CLASH	Abell 1423	179.322349	33.6109896	0.288	59.48	0.364	59.53	0.424	59.16	$0.233^{+0.206}_{-0.114}$	$47.17^{+23.91}_{-25.98}$
CLASH	MACS1206.2−0847	181.5506031	−8.80093	0.422	−75.41	0.523	−75.07	0.294	88.52	$0.536^{+0.018}_{-0.017}$	$109.15^{+0.61}_{-0.56}$
CLASH	MACS1311.0−0310	197.7575102	−3.1777062	0.133	−43.7	0.2	−49.03	0.347	−69.66	$0.421^{+0.076}_{-0.075}$	$10.92^{+2.04}_{-2.22}$
CLASH	RXJ1347.5−1145 A	206.8775419	−11.7526347	0.17	−4.98	0.149	−14.96	0.239	−3.28	$0.432^{+0.048}_{-0.042}$	$13.79^{+5.78}_{-4.59}$
CLASH	RXJ1347.5−1145 B	206.8825922	−11.7531986	0.376	33.57	0.358	30.0	0.429	16.06	$0.696^{+0.071}_{-0.115}$	$29.01^{+2.07}_{-1.97}$
CLASH	MACS1720.3+3536	260.0697955	35.6073118	0.19	−1.31	0.191	−9.27	0.396	−2.12	$0.272^{+0.042}_{-0.052}$	$5.2^{+2.24}_{-4.36}$
CLASH	Abell 2261	260.6130615	32.1326534	0.061	−18.87	0.147	−6.03	0.112	−7.0	$0.2^{+0.027}_{-0.028}$	$46.36^{+2.33}_{-3.46}$
CLASH	MACS1931.8−2635	292.9567874	−26.575729	0.162	−24.71	0.467	−25.8	0.448	−26.85	$0.459^{+0.017}_{-0.022}$	$-5.03^{+1.03}_{-0.88}$
CLASH	RXJ2129.7+0005	322.4164769	0.0892336	0.405	68.4	0.476	55.15	0.454	66.89	$0.547^{+0.045}_{-0.036}$	$67.51^{+0.88}_{-0.74}$

Table 4.3. Continuation of Table 4.2.

survey	BCG name	ra	dec	$e^{10}_{\rm BCG}$	$\theta^{10}_{\rm BCG}$	$e^{20}_{\rm BCG}$	$\theta^{20}_{\rm BCG}$	$e^{30}_{\rm BCG}$	$\theta^{30}_{\rm BCG}$	$e_{\rm SL}$	$\theta_{\rm SL}$
CLASH	MS 2137−2353	325.0631662	−23.6611459	0.099	62.61	0.183	−30.62	0.068	−84.57	$0.204^{+0.055}_{-0.05}$	$60.52^{+3.43}_{-2.36}$
CLASH	MACS0647.7+7015	101.9610124	70.2483297	0.414	−71.06	0.778	−71.88	0.694	−72.56	$0.787^{+0.009}_{-0.018}$	$104.91^{+0.41}_{-0.45}$
CLASH	MACS2129.4−0741	322.3587881	−7.6910536	0.401	80.12	0.759	76.21	0.663	79.4	$0.576^{+0.041}_{-0.047}$	$81.2^{+1.34}_{-1.24}$
RELICS	Abell 2163	243.9539405	−6.1448406	0.271	−85.83	0.307	−83.8	0.278	−78.32	$0.398^{+0.057}_{-0.061}$	$91.04^{+1.92}_{-2.09}$
RELICS	Abell 2537	347.0925316	−2.1920915	0.235	−53.04	0.51	−53.46	0.433	−55.26	$0.391^{+0.049}_{-0.048}$	$-57.48^{+2.03}_{-1.18}$
RELICS	Abell 3192	59.7253299	−29.9252985	0.654	61.49	0.557	59.16	0.572	54.43	$0.557^{+0.112}_{-0.096}$	$71.87^{+7.56}_{-9.16}$
RELICS	Abell 697	130.7398208	36.3664976	0.513	22.0	0.277	13.39	0.236	−4.84	$0.516^{+0.153}_{-0.132}$	$-25.61^{+2.71}_{-1.91}$
RELICS	Abell S295 A	41.3533874	−53.0293239	0.244	−54.89	0.369	−57.57	0.671	73.81	$0.668^{+0.076}_{-0.11}$	$-51.58^{+2.99}_{-3.05}$
RELICS	Abell S295 B	41.3956943	−53.048456	0.021	84.56	0.641	20.31	0.488	18.58	$0.732^{+0.045}_{-0.079}$	$-27.57^{+1.97}_{-1.86}$
RELICS	ACT-CL J0102-49151	15.7406954	−49.2720008	0.479	−48.66	0.429	−46.5	0.493	−45.9	$0.637^{+0.052}_{-0.039}$	$-61.95^{+2.62}_{-4.55}$
RELICS	CL J0152.7-1357	28.1824343	−13.955155	0.66	−60.18	0.372	−68.61	0.43	−69.49	$0.683^{+0.07}_{-0.098}$	$37.2^{+2.08}_{-4.79}$
RELICS	MACS J0159.8-0849	29.9554505	−8.8329993	0.45	−73.03	0.133	−46.31	0.151	88.02	$0.345^{+0.108}_{-0.085}$	$66.19^{+3.77}_{-4.38}$
RELICS	MACS J0257.1-2325	44.2864412	−23.4346896	0.273	86.84	0.383	82.99	0.456	81.37	$0.773^{+0.017}_{-0.023}$	$88.23^{+1.08}_{-1.14}$
RELICS	MACS J0308.9+2645	47.2331706	26.760531	0.676	−16.35	0.454	65.47	0.323	63.51	$0.191^{+0.03}_{-0.036}$	$60.29^{+0.94}_{-0.9}$
RELICS	MACSJ0417.5-1154	64.3945535	−11.9088405	0.533	−31.88	0.462	−31.04	0.491	−12.17	$0.667^{+0.02}_{-0.03}$	$-33.87^{+0.56}_{-0.5}$
RELICS	MACS J0553.4-3342 A	88.357296	−33.7076965	0.175	−85.07	0.292	−83.51	0.652	−83.0	$0.696^{+0.04}_{-0.055}$	$93.58^{+0.7}_{-0.6}$
RELICS	MACS J0553.4-3342 B	88.3306883	−33.7075393	0.747	−28.01	0.609	−40.65	0.508	−54.07	$0.414^{+0.22}_{-0.158}$	$111.16^{+17.06}_{-13.3}$
RELICS	PLCK G171.9-40.7	48.2394369	8.369767	0.133	−55.4	0.293	−54.83	0.679	−51.3	$0.692^{+0.031}_{-0.031}$	$-35.91^{+1.32}_{-1.72}$
RELICS	PLCK G287.0+32.9	177.7089998	−28.0821435	0.185	−29.57	0.282	−36.87	0.693	−65.23	$0.577^{+0.054}_{-0.078}$	$-35.51^{+2.96}_{-1.59}$
RELICS	RXC J0142.9+4438	25.7300898	44.6346655	0.388	−25.64	0.342	−24.02	0.507	−47.01	$0.233^{+0.025}_{-0.027}$	$-19.54^{+0.46}_{-0.45}$
RELICS	RXC J2211.7-0350	332.9413416	−3.8289814	0.224	8.36	0.273	12.72	0.321	17.8	$0.469^{+0.047}_{-0.049}$	$8.41^{+2.07}_{-1.05}$
RELICS	SPT-CL J0615-5746 A	93.9654777	−57.7801148	0.388	27.37	0.67	18.65	0.703	23.67	$0.539^{+0.091}_{-0.104}$	$14.24^{+8.22}_{-7.75}$
RELICS	SPT-CL J0615-5746 B	93.9703845	−57.7753024	0.368	81.72	0.119	−64.51	0.798	84.73	$0.524^{+0.082}_{-0.116}$	$25.55^{+4.84}_{-4.55}$

4.4 Ellipticities and alignment angles between DM haloes and BCGs in the HST cluster sample

Figure 4.3 shows the correlation between ellipticities of DM haloes that are derived from strong lensing method and those of BCGs. We find that DM haloes are on average more elliptical than their BCGs. Specifically, the mean value of difference of ellipticities is found to $\langle e_{\rm SL} - e_{\rm BCG} \rangle = 0.11 \pm 0.03$, where $e_{\rm SL}$ and $e_{\rm BCG}$ denote ellipticities of DM haloes measured by strong lensing and those of BCGs at the fiducial scale $R_{ab} = 20$ pkpc, respectively. This result appears to be inconsistent with our result shown in section 3.3, in which ellipticities of DM distribution and those of CGs of cluster-sized haloes are found to be similar in the Horizon-AGN simulation despite with large scatters. We will make more direct comparison in section 4.5.

Our result also indicates that the correlation between $e_{\rm SL}$ and $e_{\rm BCG}$ is not tight. Hashimoto *et al.* (2008) measured the shapes of BCGs and X-ray surface brightness of their host clusters and found that these ellipticity values are not strongly correlated. Given that the X-ray emitting hot gas distribution in galaxy clusters follows the potential of host halo (e.g. Donahue *et al.*, 2016), our result is qualitatively consistent with Hashimoto *et al.* (2008).

Figure 4.4 plots the correlation between position angles of DM haloes derived by strong lensing method and those of BCGs. We find that both the position angles are well aligned with each other. This result is qualitatively consistent with those of cluster-sized haloes in Horizon-AGN simulation (see Figure 3.6).

Figures 4.5 and 4.6 show the redshift dependence of ellipticities of DM haloes and BCGs, respectively. Both the ellipticities do not show strong dependence on redshift. Figure 4.7 shows that the difference of ellipticities, $e_{\rm SL} - e^{20}_{\rm BCG}$, which also does not strongly depend on redshift.

Figure 4.8 shows the redshift dependence of alignment angles between DM haloes measured by strong lensing and BCGs fitted at the fiducial scale $R_{ab} = 20$ pkpc. We find that the alignment angles do not depend on redshift strongly. Since we do not find significant redshift dependence for any observed quantities, we ignore the redshift dependence in the following analysis shown below.

4.5 Comparison with Horizon-AGN simulation

In previous section, we find that ellipticity values of DM haloes are on average larger than those of BCGs in galaxy clusters. In contrast, these values are similar in the Horizon-AGN simulation (see chapter 3). One possible explanation comes from the difference of mass scales between observations ($\sim 10^{15} M_{\odot}$) and cluster-sized haloes in the Horizon-AGN simulation ($\sim 10^{14} M_{\odot}$). In order to check this possibility, in this section we explore the mass dependence of DM haloes and CGs in the Horizon-AGN simulation. Unfortunately,

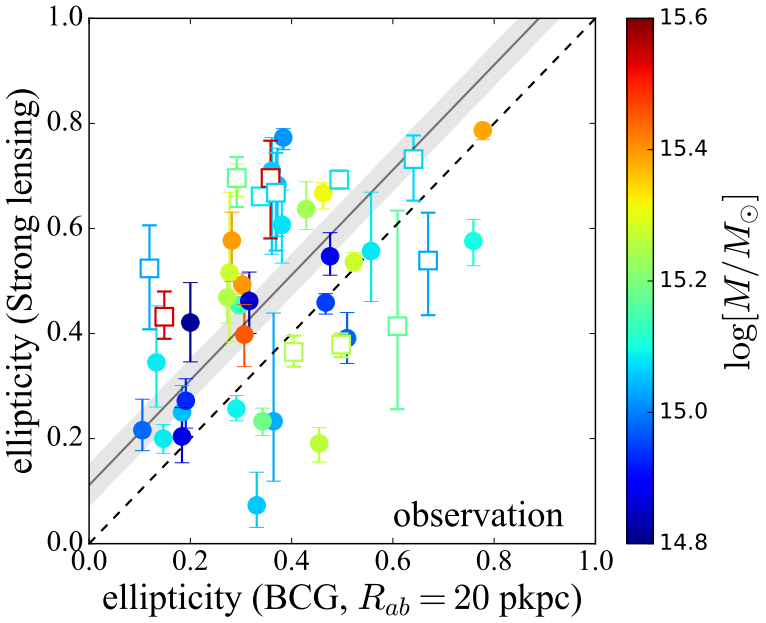

Figure 4.3. Ellipticities of DM haloes against those of BCGs fitted at the fiducial scale $R_{ab} = 20$ pkpc. Color corresponds to cluster mass. Filled circles and open squares indicate single and double peak clusters, respectively. Dashed line indicates that the ellipticity of DM haloes and BCGs are the same. Solid line with shading region shows the mean values and its error of the difference between $e_{\rm SL}$ and $e^{20}_{\rm BCG}$.

since there is no DM halo in the Horizon-AGN simulation whose mass is comparable to the observed galaxy clusters, we cannot directly compare the observation with the simulation. Nevertheless, we expect that the analysis of the mass dependence in the Horizon-AGN simulation may provide a clue to the origin of the difference.

Following section 3.1, we identify DM haloes using the ADAPTAHOP halo finder (Aubert *et al.*, 2004; Tweed *et al.*, 2009) and select all DM haloes with masses higher than $10^{12.5} M_\odot$, which roughly corresponds to massive galaxies. The masses of these haloes are defined by the FOF mass which roughly corresponds to the virial mass. We choose the snapshot at redshift $z = 0.39$ that is close to the mean value of redshifts of observed clusters, $\langle z \rangle = 0.43$. This is justified because in previous section we show that the redshift dependence of observed values is weak if exist. In addition, we checked that the redshift dependence of ellipticities and alignments between DM haloes and CGs is weak in the Horizon-AGN simulation, if we compare haloes with similar masses at different redshifts. The total number of DM haloes used for the analysis is 1265. In order to make a fair comparison with observations, we create projected particle distributions for each haloes following section 3.1. We consider three different projection directions assuming x-, y-, and z-axes as line-of-sight directions and regard these three projections as independent so that we effectively have $N_{\rm cl} \equiv 3795$ DM haloes for our analysis.

Following section 3.1, we use the mass tensor similar to equation (3.1) to fit the ellipse to

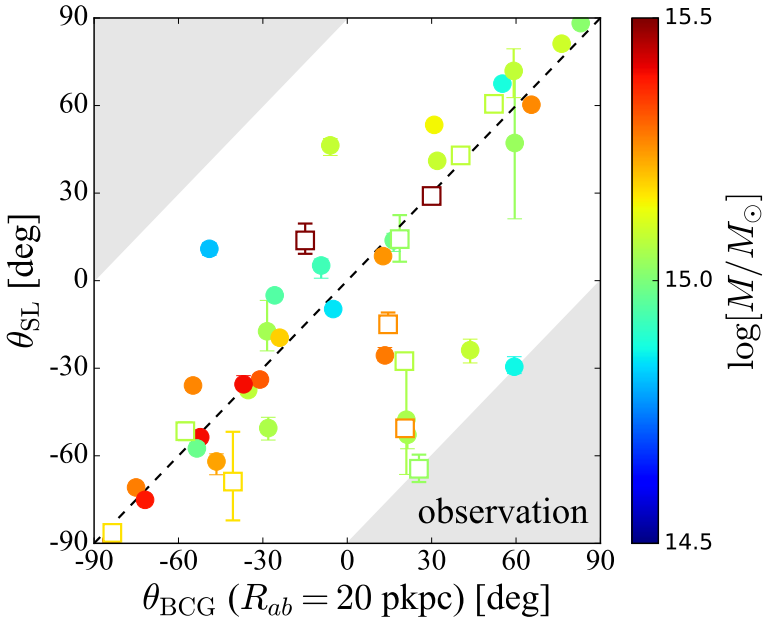

Figure 4.4. Position angles of DM haloes against those of BCGs fitted at the fiducial scale $R_{ab} = 20$ pkpc. Symbols are same as in Figure 4.3. Dashed line indicates the case of the perfect alignment, $\theta_{\rm SL} = \theta_{\rm BCG}$. The shaded regions have misalignment angles larger than 90°, $|\theta_{\rm SL} - \theta_{BCG}| > 90°$, and thus position angles of clusters in this regions are shifted by 90° to locate them in the proper position.

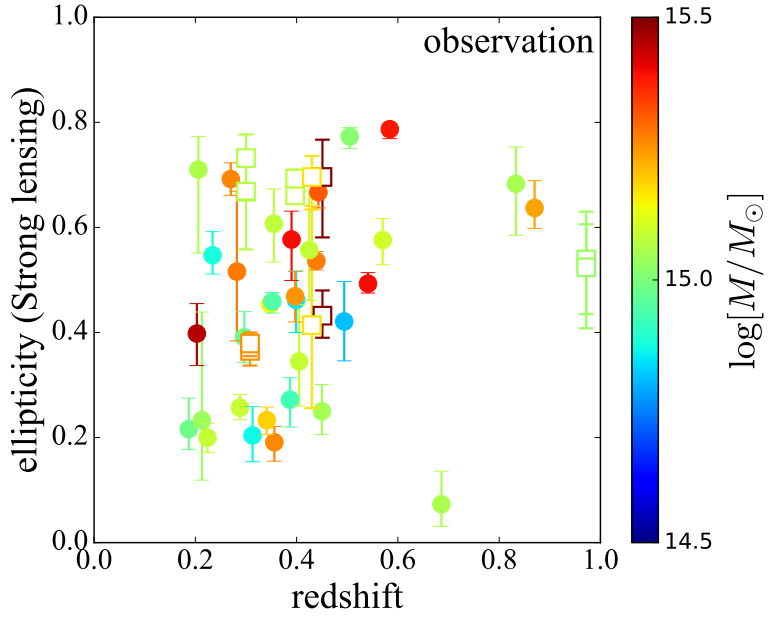

Figure 4.5. Ellipticities of DM haloes measured by strong lensing as a function of redshift. Symbols are same as in Figure 4.3.

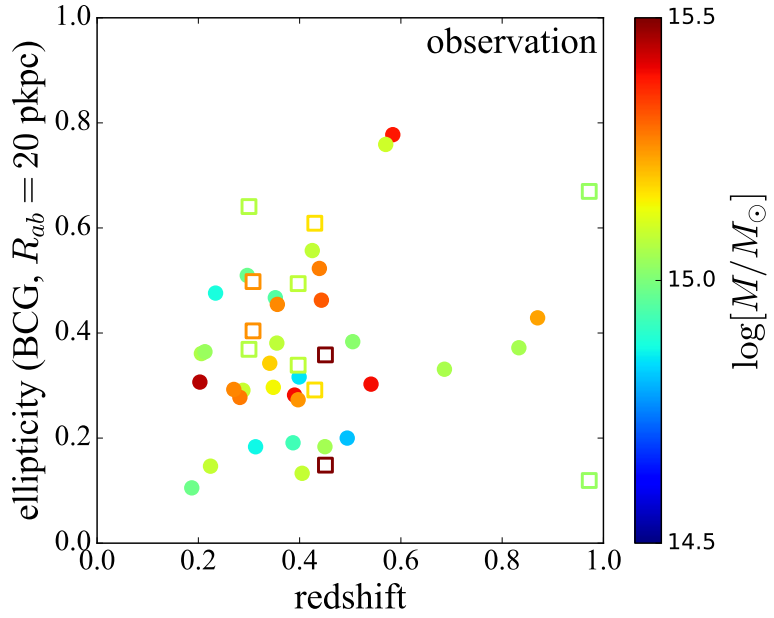

Figure 4.6. Ellipticities of BCGs fitted at the fiducial scale $R_{ab} = 20$ pkpc for as a function of redshift. Symbols are same as in Figure 4.3.

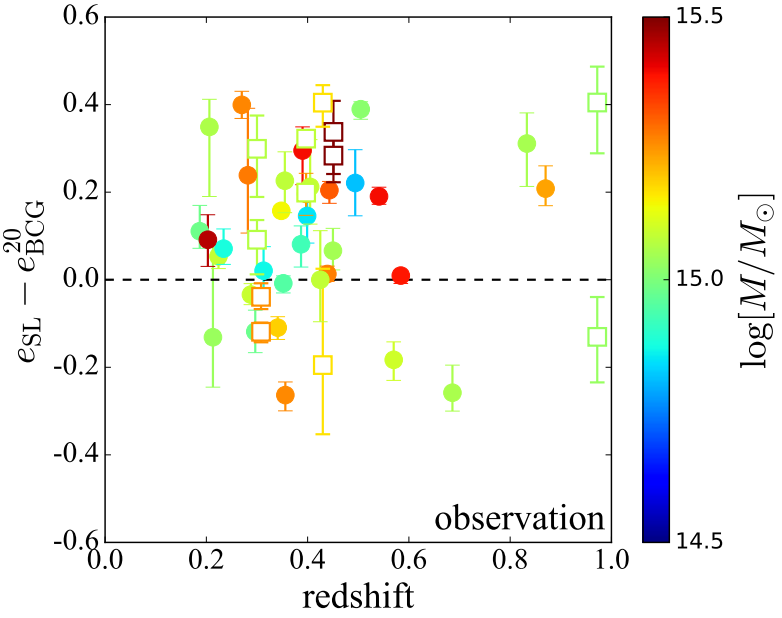

Figure 4.7. Difference of ellipticities between DM haloes measured by strong lensing and BCGs fitted at the fiducial scale $R_{ab} = 20$ pkpc as a function of redshift. Symbols are same as in Figure 4.3.

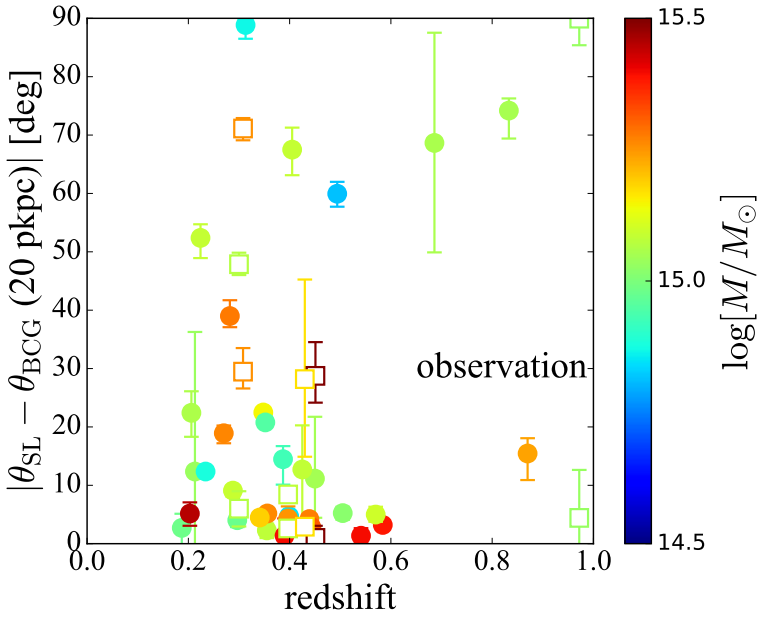

Figure 4.8. Alignment angles between DM haloes measured by strong lensing and BCGs fitted at the fiducial scale $R_{ab} = 20$ pkpc as a function of redshift. Symbols are same as in Figure 4.3.

both the DM haloes and CGs. For DM haloes, we use only particles belonging to the most *massive* structure in the halo, where substructures are eliminated by ADAPTAHOP finder. This is because the strong lensing observation separates substructures and measures the shape of only the smooth part of the DM distribution in the cluster (see section 4.2). In contrast, for the CGs in the simulation, we use all the stellar particles around the central region of the halo in projection because we do not exclude substructures in ellipse fit for observed BCGs (see section 4.3). For the CGs, we extract all the stellar particles in a cube with size of (500 pkpc)^3, create project images to use these particles, and compute the ellipse fit in the same manner for ellipses of CGs in section 3.1. We adopt 10, 20, and 30 pkpc for CGs in the same manner as in observation and 100 pkpc for DM haloes that matches the typical Einstein radii of the observed clusters. Since the spatial resolution of the Horizon-AGN simulation of ~ 1 kpc is sufficiently small compared with the ellipse scales, we can safely ignore the effect in our analysis.

After we fit the ellipses for each halo in the simulation by the above procedure, we divide the haloes in to 6 mass bins according to their DM halo masses, $M < 5 \times 10^{12} M_\odot$, $5 \times 10^{12} M_\odot \leq M < 10^{13.0} M_\odot$, $10^{13.0} M_\odot \leq M < 2 \times 10^{13} M_\odot$, $2 \times 10^{13} M_\odot \leq M < 5 \times 10^{13.0} M_\odot$, $5 \times 10^{13} M_\odot \leq M < 10^{14.0} M_\odot$, and $10^{14} M_\odot \leq M$. We then compute mean values of ellipticities and alignment angles between DM haloes and CGs for each mass bin. Figure 4.9 shows mean values of ellipticities of DM haloes as a function of DM halo mass. We can see a clear trend that shapes of DM haloes with higher mass are on average more elliptical than those with smaller masses. This result is qualitatively consistent with the result in e.g. Despali *et al.* (2014), who analysed three different cosmological simulations

Table 4.4. Mean values and their errors of ellipticities of DM haloes. The errors are defined as standard deviation divided by the square root of number of DM haloes in each bin.

		$\log[\langle M_{\rm DM}\rangle/M_\odot]$	$\langle e_{\rm DM}\rangle$
observation	all	15.14	0.482 ± 0.028
	single peak	15.12	0.451 ± 0.033
	double peak	15.19	0.567 ± 0.04
	HFF	15.20	0.507 ± 0.05
	CLASH	15.08	0.418 ± 0.046
	RELICS	15.17	0.535 ± 0.036
simulation		12.6	0.233 ± 0.003
		12.8	0.252 ± 0.004
		13.1	0.27 ± 0.005
		13.5	0.3 ± 0.008
		13.8	0.324 ± 0.015
		14.3	0.374 ± 0.026

and investigated mass dependence of halo shapes. While their shape measurement is based on the three dimensional triaxial fitting and thus cannot be directly compared with our results, these DM only cosmological simulations also indicate that haloes with higher masses have more triaxial shapes (see their Figure 4). This can be interpreted as follows. In general, more massive DM haloes are dynamically young and still experiencing major mergers or smooth mass accretions along filaments, whereas less massive ones are formed at the earlier epoch and thus they have enough time to reach a relaxation. Therefore, it is reasonable that more massive DM haloes tend to be more elliptical while less massive ones tend to be more spherical.

The mean value of ellipticities of observed clusters is also plotted in Figure 4.9. As expected, the mean value is higher than those of DM haloes in the simulation. suggesting that the mass dependence of ellipticities might be the reason of $e_{\rm DM} > e_{\rm BCG}$ for the observed clusters. Table 4.4 shows mean values of ellipticities of DM haloes. We also compute mean values of ellipticities for single and double peak clusters. We find that double peak clusters are more elongated than single peak clusters, which is naturally understood because double peak clusters are dynamically younger than single peak clusters.

Figure 4.10 plots the mean values of ellipticities of BCGs in observations and CGs in the simulation as a function of DM halo mass. For the scales of $R_{ab} = 20$ and 30 pkpc, we can find the trend similar to DM haloes, whereas for 10 pkpc, the mean values of ellipticities are almost constant against the halo mass in the simulation. For lower halo mass, the CG shapes are rounder at larger scales, whereas for higher mass, these are more elongated at larger scales. One possible reason of this result is that inner regions formed at the earlier epoch and have enough time to relax, and thus they forget the information of accretion or formation history and are independent of the host halo mass. Another possibility is the

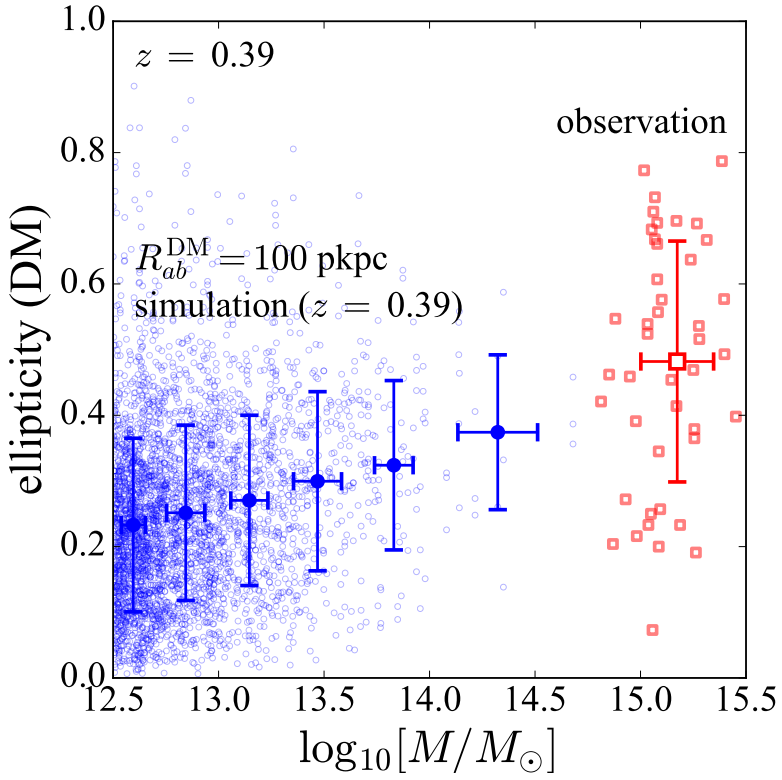

Figure 4.9. Blue large filled circles and red open square show mean values of ellipticities of DM haloes derived from the Horizon-AGN simulation and strong lensing observations, respectively. We adopt redshift $z = 0.39$ and fitted ellipse scale $R_{ab} = 100$ pkpc in the Horizon-AGN simulation. Error-bars of x- and y-axis directions denote the standard deviation of DM halo mass and ellipticities, respectively. Small circles and squares show individual values of ellipticities in the Horizon-AGN simulation and observations, respectively.

effect of substructures that tend to exist at larger scales and make ellipse more elongate.

Since we adopt the same tensor method for ellipse fit of observed BCGs and the CGs in the simulation, ellipticity values of BCGs can be directly compared with those of CGs in the simulation unlike DM haloes. Figure 4.10 suggests that observed values could be explained by the extrapolation of the simulation. Table 4.4 shows mean values of ellipticities of observed BCGs and CGs in the simulation. While double peak clusters are more elongated than single peak clusters in the outer region, 30 pkpc, their values are similar at 10 pkpc. This is presumably because stellar components in the inner region are tightly bound with each other, and thus their distributions are not affected by external phenomena such as major mergers or mass accretions.

Figure 4.11 plots mean values of differences between ellipticities of DM haloes and those of (B)CGs. While the mean values are closer to 0 in the simulation, those of observed values are higher, $0.1 - 0.2$. We confirmed that these values are almost the same for the different three surveys (see Tables 4.4, 4.5). As we discussed in section 4.4, this difference might be due to the difference of mass scales between observations and the simulation.

Table 4.5. Mean values and their errors of ellipticities of (B)CGs. The errors are defined as standard deviation divided by the square root of number of (B)CGs in each bin.

		$\log[\langle M_{\rm DM}\rangle/M_\odot]$	R_{ab} [pkpc]	$\langle e_{\rm (B)CG}\rangle$
observation	all	15.14	10	0.308 ± 0.027
			20	0.37 ± 0.024
			30	0.421 ± 0.026
	single peak	15.12	10	0.305 ± 0.03
			20	0.355 ± 0.027
			30	0.399 ± 0.029
	double peak	15.19	10	0.314 ± 0.062
			20	0.412 ± 0.052
			30	0.48 ± 0.057
	HFF	15.20	10	0.290 ± 0.073
			20	0.389 ± 0.034
			30	0.366 ± 0.063
	CLASH	15.08	10	0.24 ± 0.026
			20	0.345 ± 0.043
			30	0.361 ± 0.037
	RELICS	15.17	10	0.381 ± 0.044
			20	0.389 ± 0.033
			30	0.494 ± 0.038
simulation		12.6	10	0.282 ± 0.004
			20	0.258 ± 0.003
			30	0.254 ± 0.003
		12.8	10	0.282 ± 0.004
			20	0.274 ± 0.004
			30	0.278 ± 0.004
		13.1	10	0.294 ± 0.006
			20	0.305 ± 0.006
			30	0.314 ± 0.006
		13.5	10	0.3 ± 0.008
			20	0.325 ± 0.008
			30	0.336 ± 0.008
		13.8	10	0.297 ± 0.018
			20	0.352 ± 0.017
			30	0.387 ± 0.015
		14.3	10	0.338 ± 0.032
			20	0.362 ± 0.035
			30	0.374 ± 0.035

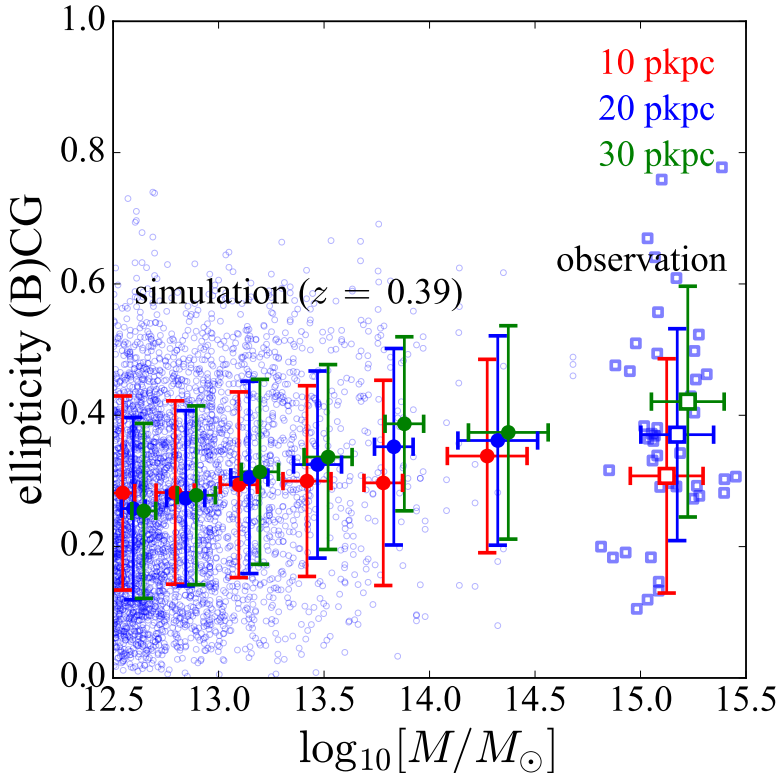

Figure 4.10. Large filled circles and open squares show mean values of ellipticities of CGs derived from the Horizon-AGN simulation and BCGs in HST observations, respectively. We show results for different ellipse scales, R_{ab} of 10 (red), 20 (blue), and 30 (green) pkpc, respectively for both observation and simulation. Just for the clarity, red and green symbols are shifted by -0.05 and $+0.05$ in the horizontal direction, respectively. We adopt redshift $z = 0.39$ for the analysis of the Horizon-AGN simulation. Error-bars of x- and y-axis directions denote the standard deviation of DM halo mass and ellipticities, respectively. Small circles and squares are individual values of ellipticities at $R_{ab} = 20$ pkpc of Horizon-AGN simulation and HST observations, respectively.

Figure 4.11 suggests that there is no strong trend of the mean values against the halo mass in the simulation. There is, however, weak trend of increasing $\langle e_{\rm SL} - e_{\rm BCG} \rangle$ particularly for $R_{ab}^{CG} = 10$ pkpc, which might explain observed values by extrapolating the mass dependence.

In addition to the mass dependence of ellipticities, we investigate that of alignment angles between DM haloes and the CGs. Figure 4.12 plots mean values of the alignment angles. In the low mass region $\log[M/M_\odot] < 14.0$, there is a clear trend that the alignment becomes tighter with increasing masses. However, in the high mass region $\log[M/M_\odot] > 14.0$, the alignment appears to be constant independent of the mass increase. This is presumably because low mass haloes and their CGs formed in the early epoch thus they lose information of the initial condition, while high mass haloes are dynamically young

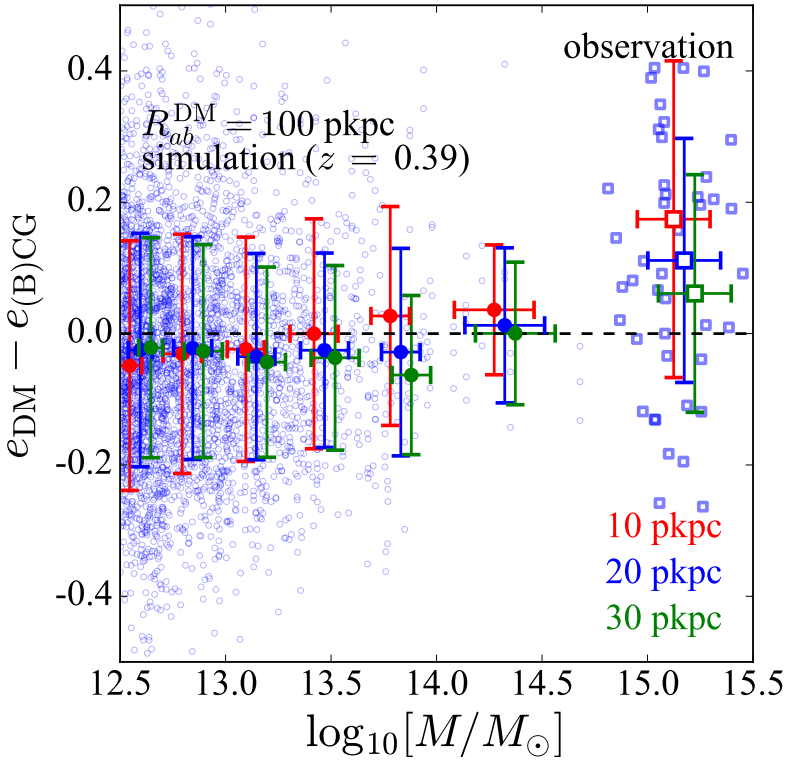

Figure 4.11. The mean values of difference between ellipticities of DM haloes and those of (B)CGs. Symbols are same as in Figure 4.10. Black squares show values taken from the analysis of strong lens systems at smaller mass scales (Bruderer *et al.*, 2016).

and are strongly affected by anisotropic surrounding environment such as filaments. Table 4.6 summarizes the mean values of the alignment angles.

4.6 Discussions

The difference of ellipticities between DM haloes and BCGs might be due to selection criteria. In particular, CLASH clusters are selected such that their shapes are round in X-ray images. In fact, Tables 4.4, 4.5 show that the mean values of ellipticities of CLASH survey are rounder than the other surveys. However, we confirmed that the differences of ellipticities for the three surveys are consistent within error-bars by dividing clusters for each survey to compute each mean value. Values of the mean ellipticities are 0.118 ± 0.061 (HFF), 0.072 ± 0.037 (CLASH), and 0.146 ± 0.046 (RELICS).

We find that observed values of the difference between ellipticities of DM haloes and BCGs, $e_{\rm SL} - e_{\rm BCG}$, are on average larger than 0, which differs from the result of the Horizon-AGN simulation for which the average difference is consistent with 0. Our results appear to be consistent with Gonzalez *et al.* (2005), who find that position angles of intracluster light (ICL) distributions tend to be aligned well with those of BCGs and ICL

Table 4.6. Mean values and their errors of alignment angles between DM haloes and the CGs. The errors are defined as standard deviation divided by the square root of number of DM haloes in each bin.

		$\log[\langle M_{\rm DM}\rangle/M_\odot]$	R_{ab} [pkpc]	$\langle\lvert\theta_{\rm DM}-\theta_{\rm (B)CG}\rvert\rangle$ [deg]
observation	all	15.14	10	23.1 ± 3.8
			20	22.2 ± 3.9
			30	23.3 ± 3.3
	single peak	15.12	10	22.3 ± 4.6
			20	20.6 ± 4.3
			30	21.8 ± 3.7
	double peak	15.19	10	25.2 ± 6.3
			20	26.7 ± 8.5
			30	27.4 ± 7.0
	HFF	15.20	10	37.6 ± 8.7
			20	22.6 ± 9.8
			30	21.3 ± 10.0
	CLASH	15.08	10	16.7 ± 4.8
			20	22.3 ± 5.8
			30	24.0 ± 5.3
	RELICS	15.17	10	24.8 ± 6.0
			20	22.0 ± 5.9
			30	23.2 ± 4.3
simulation		12.6	10	34.4 ± 0.7
			20	30.6 ± 0.6
			30	28.2 ± 0.6
		12.8	10	31.0 ± 0.7
			20	26.1 ± 0.7
			30	23.7 ± 0.7
		13.1	10	27.1 ± 1.0
			20	23.1 ± 1.0
			30	20.4 ± 0.9
		13.5	10	23.2 ± 1.3
			20	18.1 ± 1.1
			30	16.3 ± 1.0
		13.8	10	20.6 ± 2.4
			20	13.3 ± 1.6
			30	11.1 ± 1.5
		14.3	10	21.3 ± 5.3
			20	18.3 ± 5.5
			30	12.5 ± 2.8

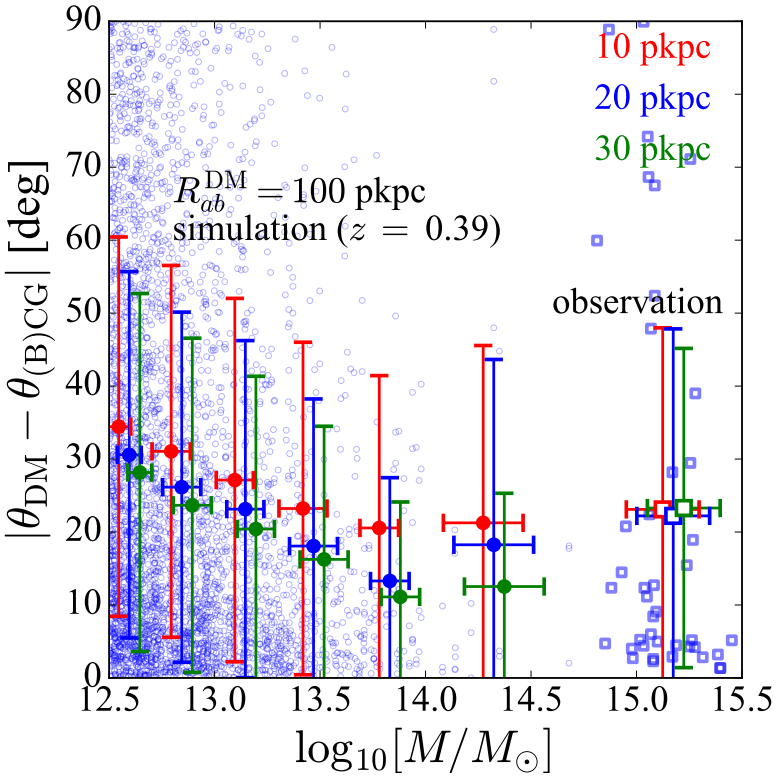

Figure 4.12. The mean values of alignment angles between major axes of DM haloes and those of (B)CGs. Symbols are the same in Figure 4.10.

distributions are more elongated than BCGs, if we assume that ICL distributions trace DM distributions as suggested by e.g. Montes & Trujillo (2019).

This difference is potentially interesting and requires some explanations. In what follows, we discuss possible causes of this apparent discrepancy between observations and the Horizon-AGN simulation.

(i) First, as already mentioned, a possible explanation comes from the difference of mass scales. Figure 4.9 indicates that ellipticities of DM haloes show a clear trend with mass and the observed value might be explained by the *extrapolation* of values in the simulation. Figure 4.10 shows that the observed ellipticity values of the BCGs can be explained by the extrapolation of the simulation, and thus the observed difference could also be explained by the mass dependence. Figure 4.11 indicates that the difference of ellipticities $e_{\rm DM} - e_{\rm CG}$ in the simulation shows a weak trend especially at the inner region such that the extrapolation of the trend may explain the observation. The possibility of this mass dependence may also be tested by other observations at smaller masses. Figure 4.13 compares the probability distributions of the ellipticity difference for our observation and the Horizon-AGN simulation with that of previous observational work by Bruderer *et al.* (2016), in which they measure projected shapes of 11 DM haloes by strong lensing and compare them with those of light profiles of the central galaxies. Since their definition of the ellipticity $(a^2 - b^2)/(a^2 + b^2)$ is different from ours, $1 - b/a$ with a

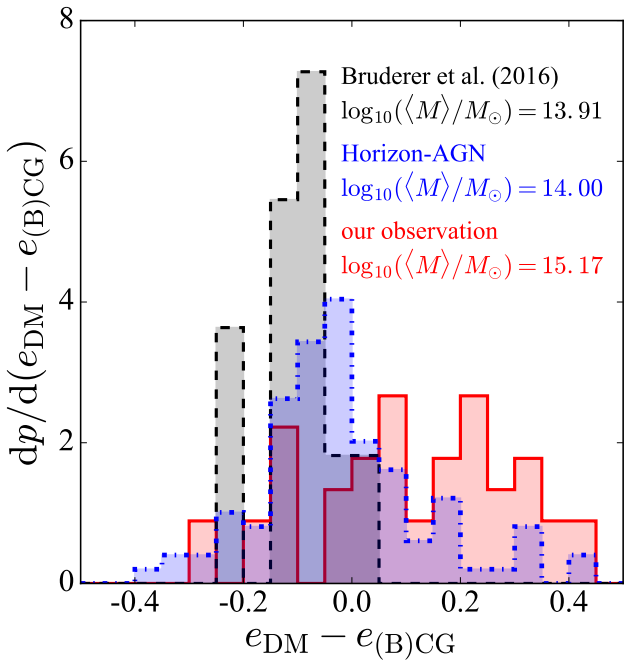

Figure 4.13. The probability distributions of the ellipticity difference, $e_{\rm DM} - e_{\rm (B)CG}$, observed by Bruderer *et al.* (2016) (black dashed), our observation (red solid), and in the Horizon-AGN simulation (blue dot-dashed). We use only haloes with their masses larger than $5 \times 10^{13} M_\odot$ in the Horizon-AGN simulation.

and b being lengths of semi-major and -minor axes, respectively, we convert their values to our definition. Their results show the opposite trend $e_{\rm SL} < e_{\rm CG}$, implying that the mass dependence is strong (see also Rusu *et al.*, 2016, for a similar result), although a caveat is that their strong lensing measurements probe radii smaller than 100 pkpc that we adopted in the simulation. Figure 4.13 also indicates that the probability distribution of the ellipticity difference in Bruderer *et al.* (2016) differs from that in the Horizon-AGN simulation with similar halo masses. More strong lens samples at different mass scales as well as simulations in larger box sizes are required to test this scenario further.

(ii) Another possibility is that strong lensing method we use to measure ellipticities of DM haloes is biased such that it derives higher ellipticity values than those of real DM mass distributions. Figure 4.14 compares our measurement values by strong lensing with those by weak lensing analysis (Umetsu *et al.*, 2018) for 15 galaxy clusters whose ellipticities are evaluated by both strong and weak lensing. The mean value estimated by strong lensing, $\langle e_{\rm SL}\rangle = 0.405 \pm 0.053$, is higher than those by weak lensing, $\langle e_{\rm WL}\rangle = 0.344 \pm 0.04$, although they are consistent with each other within the errors. Figure 4.15 shows the comparison of position angles. Both position angles are well aligned with each other despite the large errors for weak lensing measurements. Although we cannot draw any robust conclusion because weak and strong lensing measure ellipticities at different scales, this result implies that the strong lensing method might slightly over-estimate ellipticities.

On the other hand, Meneghetti *et al.* (2017) compares real DM mass distributions with

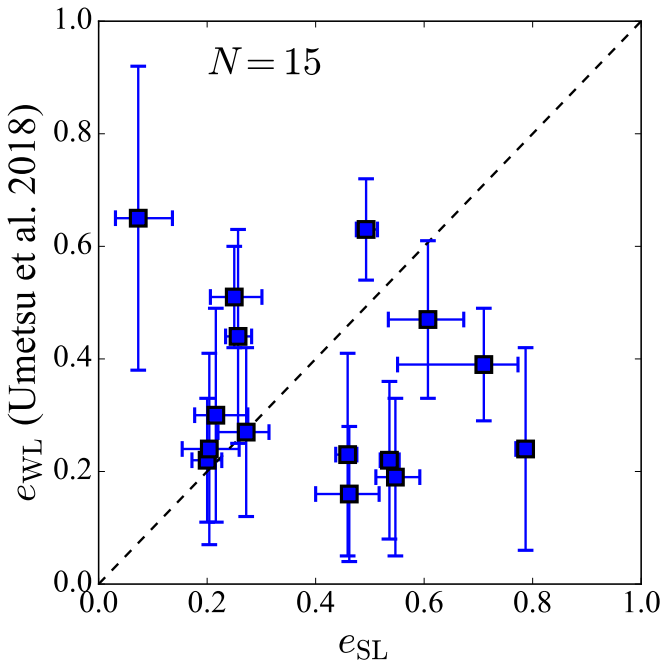

Figure 4.14. Correlation between values of ellipticities measured by strong lensing (x-axis) in this work and those by weak lensing (y-axis) from Umetsu *et al.* (2018) for the 15 galaxy clusters whose ellipticities are measured by both methods.

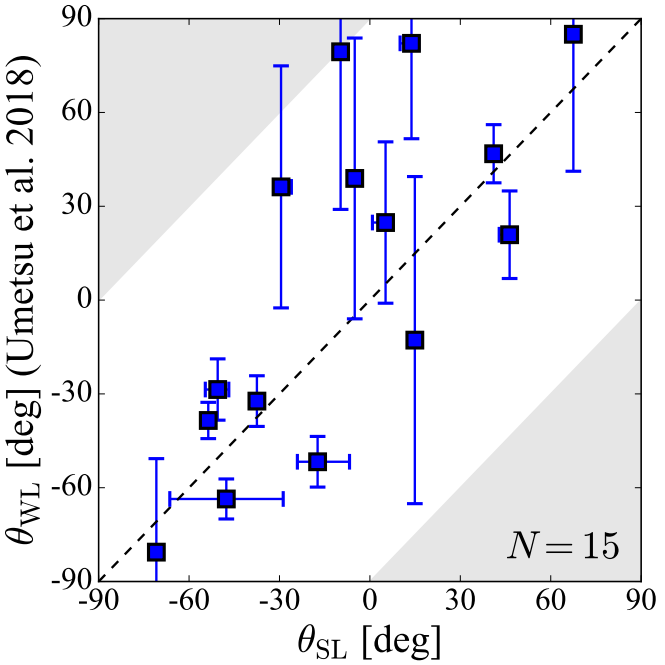

Figure 4.15. Correlation between values of position angles measured by strong lensing (x-axis) in this work and those by weak lensing (y-axis) from Umetsu *et al.* (2018) for the 15 galaxy clusters whose ellipticities are measured by both methods.

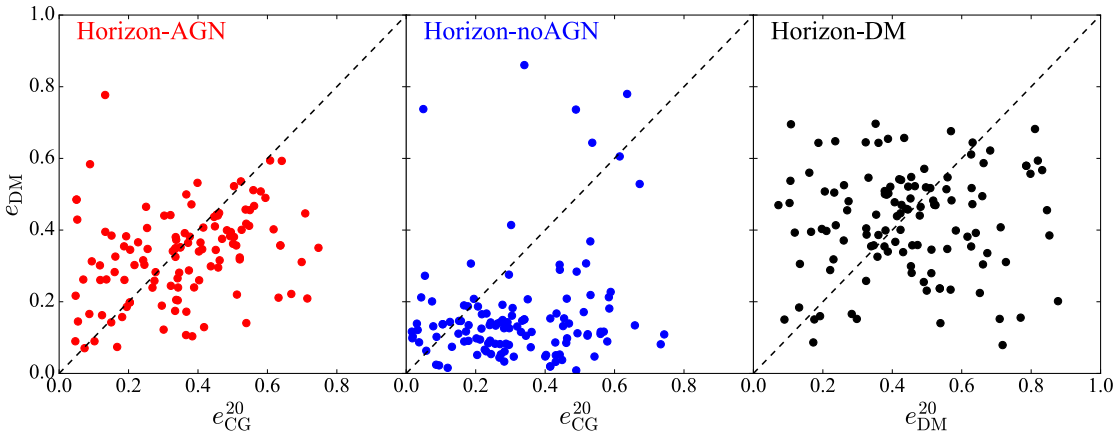

Figure 4.16. Correlations of ellipticities of DM haloes evaluated at 100 pkpc against those of CGs for the most massive 40 DM haloes in the Horizon-AGN (left), the Horizon-noAGN (centre). We consider three different projection directions assuming x-, y-, and z-axes as line-of-sight directions and regard these three projections as independent so that we effectively plot 120 DM haloes. The ellipticities are evaluated by the same procedures described in subsection 4.5. For reference, left panel shows the correlation between ellipticities of DM haloes evaluated at 100 pkpc and at 20 pkpc. The ellipticities at 100 pkpc are computed by the same procedures described in subsection 4.5. At inner part (20 pkpc), we first extract all the DM particles within a (100 pkpc)^3 cube with the centre of the mass of the DM halo at the centre, and then we project these particles along the three line-of-sight directions to compute the ellipticities.

those inferred from various strong lensing methods by using simulated cluster images with mock multiple images which mimic the HST Frontier Field survey. This mock challenge demonstrated that if there are a sufficient number of multiple images (say > 100), strong lensing method accurately reproduces input DM mass distributions. In fact, our lensing method is one of the best methods to reproduce shapes of simulated haloes (see "GLAFIC" panel of their Figure 7). However, there are not many multiple images for some of the observed clusters (see Appendix B), for which derived ellipticities might be biased. The validation of strong lensing methods to measure ellipticities is beyond the scope of this thesis, and further studies are required.

(iii) It is also possible that the Horizon-AGN simulation produces DM haloes or CGs with their shapes different from their true shapes. Although the Horizon-AGN simulation excellently explain various observations (see section A.4 for detail), the implemented baryon physics is never perfect. Suto *et al.* (2017) investigate shapes of DM, star, and gas distributions in galaxy cluster-sized haloes for three Horizon simulation, DM only (Horizon-DM), baryon+supernova feedback (Horizon-noAGN), and baryon+supernova feedback+AGN feedback (Horizon-AGN), and argue that implemented baryon physics affects shapes of DM haloes even up to ~ 1 Mpc. The DM haloes in the Horizon-noAGN

are much rounder than those in the Horizon-DM due to gas cooling at the central region of the haloes, while their ellipticities in the Horizon-AGN are comparable to those in the Horizon-DM since heating by AGN prevents gas from overcooling which makes haloes rounder. This implies that the change of details of baryon physics may change quantitative results on halo shapes in simulations To investigate the effect of baryon physics in more detail, we measure ellipticities of DM haloes and the CGs in galaxy clusters for the three Horizon simulations. Figure 4.16 shows that the correlation between ellipticities of DM haloes and that of the CGs varies with the baryon physics. DM haloes are more rounder for both the Horizon-noAGN and the Horizon-AGN simulations than those in the Horizon-DM simulation. Therefore, the discrepancy in the difference of ellipticities might be caused by the implementation of the baryon physics. Turning the problem around, we may be able to test the baryon physics such as AGN feedback by observations of ellipticities.

(iv) The remaining possibility is that the ΛCDM model is not correct. Although the standard ΛCDM model has passed through many observational tests, there remains several challenges (e.g. Bullock & Boylan-Kolchin, 2017). For example, self-interacting instead of collisionless dark matter model is proposed as one possibility to solve them (e.g. Tulin & Yu, 2018). While collisionless dark matter forms triaxial haloes (e.g. Jing & Suto, 2002), simulations with self-interacting dark matter (SIDM) predict that shapes of DM haloes are more spherical than those in collisionless dark matter (e.g. Spergel & Steinhardt, 2000; Yoshida *et al.*, 2000a; Peter *et al.*, 2013). Robertson *et al.* (2019) investigate halo shapes by using cosmological simulations including both baryon physics and SIDM. Their results suggest that the difference of ellipticities between collisionless and SIDM haloes become larger in the inner region such that SIDM haloes are on average rounder. Therefore it appears that SIDM cannot reconcile the difference between observations and Horizon-AGN simulation, but there may be other DM scenarios that better explain the observations.

In either case, our observations provide new constraints on the background physics such as structure formation scenarios, dark matter models and theories of modified gravity. Therefore, this result should be worth investigating more by future studies in both observations and simulations. For the simulation side, larger box sizes are required so as to include higher mass haloes and exploration of baryon physics possibly to improve it. For the observational side, future large surveys such as the *Subaru* Hyper Suprime-Cam (HSC) [*4] (e.g. Miyazaki *et al.*, 2018a,b; Oguri *et al.*, 2018; Mandelbaum *et al.*, 2018) and the Large Synoptic Survey Telescope (LSST) [*5] (e.g. LSST Science Collaboration *et al.*, 2009; Ivezić *et al.*, 2019), and deep imaging by space telescopes such as the James Webb Space Telescope (JWST) [*6] (e.g. Gardner *et al.*, 2006), the Wide Field Infrared Survey Telescope (WFIRST) [*7], the *Euclid* [*8] would help to extend samples of strong lensing clusters and improve strong lensing constraints for individual clusters.

[*4] https://hsc.mtk.nao.ac.jp/ssp/
[*5] https://www.lsst.org/
[*6] https://www.jwst.nasa.gov/
[*7] https://wfirst.gsfc.nasa.gov/
[*8] https://sci.esa.int/web/euclid/

4.7 Summary

In some studies to investigate the ellipticities and position angles of the clusters, X-ray surface brightness or the member galaxy distributions are used as tracers of the shape of the host DM halo. Since these tracers need some assumptions such as dynamical state of the clusters to infer the shape of host DM halo, the estimated values depend on the validity of the assumptions. While gravitational lensing provides a powerful method to measure the shape of DM haloes directly without any assumptions, it requires both deep imaging and spectroscopic data of the background lensed galaxies. Thus, qualities and sample sizes are limited in previous studies.

In this chapter, we present a new measurement of ellipticities and position angles of individual galaxy clusters, which are observed by three deep imaging surveys by the Hubble Space Telescope. We measure shapes for 45 DM haloes in 39 galaxy clusters by strong lensing. 6 clusters have double peaks and thus we measure those shapes separately. In addition to DM haloes, we also measure shapes of BCGs of each DM halo by diagonalizing the surface brightness tensor computed from HST images in F814W band.

We obtain the mean value of ellipticities of DM haloes, $\langle e_{\rm SL}\rangle = 0.482 \pm 0.028$, and those of BCGs, $\langle e^{R_{ab}}_{BCG}\rangle = 0.308 \pm 0.027$, 0.37 ± 0.024, 0.421 ± 0.026 at $R_{ab} = 10, 20$ and 30 pkpc, respectively. The ellipticities of DM haloes are on average more elongated than those of BCGs with mean value of $\langle e_{\rm SL} - e^{20}_{\rm BCG}\rangle = 0.11 \pm 0.03$. The ellipticities of DM haloes and BCGs, and their difference do not strongly depend on the redshift. We divide our sample into 33 single peak clusters and 6 double peak clusters (12 haloes) and compute their mean ellipticities. We obtained the mean ellipticity values of DM haloes $\langle e_{\rm SL}\rangle = 0.451 \pm 0.033$ and 0.567 ± 0.04 for single and double peak haloes, respectively. We also compute the mean ellipticity values of BCG and find that both DM halo and BCG of double peak haloes are more elongated than those of single peak.

Orientations of DM haloes and BCGs are well aligned with each other and the degree of alignment is almost independent of the redshift. The mean values of the alignment angles are $\langle|\theta_{\rm SL} - \theta^{R_{ab}}_{BCG}|\rangle = 23.1 \pm 3.8$, 22.2 ± 3.9, and 23.3 ± 3.3 deg at $R_{ab} = 10, 20$ and 30 pkpc, respectively. We compute the mean alignment values for single and double peak clusters and find that these values are consistent with each other within the error-bars.

For comparison, we compute projected shapes of DM haloes and CGs in the Horizon-AGN simulation. We extract 1265 DM haloes identified by ADAPTAHOP halo finder with FOF mass higher than $10^{12.5} M_\odot$ at $\langle z\rangle = 0.39$ and create projected particle distributions. We regard three different projection directions as independent to obtain 3795 *independent* DM haloes in our analysis. Since in the Horizon-AGN simulation there is no haloes whose mass scale is comparable to observed galaxy clusters, $M_{\rm vir} \sim 10^{15} M_\odot$, we focus on the mass dependence of those shape in the mass range of $10^{12.5} M_\odot < M_{\rm vir} < 10^{14.5} M_\odot$. We compute ellipticities by tensor method for DM haloes without substructure and for CGs with substructures for a fair comparison with observations.

For DM haloes, there is a clear trend that ellipticities become higher with increasing

halo masses. Their mean values increase from 0.233 at $M_{\rm vir} = 10^{12.6} M_\odot$ to 0.374 at $10^{14.3} M_\odot$. Ellipticities of BCGs show the same but weak trend as DM haloes for the outer regions $R_{ab} = 20, 30$ pkpc, whereas ellipticities are almost constant against host halo mass in the inner region $R_{ab} = 10$ pkpc. The difference of ellipticities between DM haloes and CGs are about 0, indicating those ellipticities are almost the same.

We also compute alignment angles between DM haloes and the CGs. DM haloes and CGs are well aligned with each other and the degree of the alignment shows the mass dependence; the alignment becomes tighter with increasing halo masses. The mean values change from $\langle|\theta_{\rm DM} - \theta^{20}_{\rm CG}|\rangle = 30.6 \pm 0.6$ deg at $M_{\rm vir} = 10^{12.6} M_\odot$ to 18.3 ± 5.5 deg at $10^{14.3} M_\odot$. For all mass bins, the inner region of CGs shows tighter alignment than outer regions.

Chapter 5

Cosmological evolution of orientations of cluster-sized dark matter haloes and their central galaxies

This chapter explores the origin of the alignments between orientations of galaxy clusters and those of their central galaxies in the ΛCDM universe using the Horizon-AGN simulation. First, we see when the tight alignments at the present time as seen in chapter 3 were formed by examining the time evolution of the alignments during cosmic time from $t = 1.5$ Gyr to 13.5 Gyr.

Next, we investigate the correlation between mass accretion episodes and orientation changes. Since the ΛCDM model predicts bottom-up structure formation, DM haloes and BCGs are considered to grow by repeated mergers, and their orientations are also greatly changed by the mergers. We follow DM haloes and CGs for *individual* galaxy clusters to investigate effects of the mass accretion episodes on the orientation changes.

Finally, we investigate the evolution of orientations of galaxy clusters relative to surrounding matter distributions. In the ΛCDM universe, galaxy clusters are generally located at filament intersections, and the mergers occur preferentially along directions of the filaments. Therefore, the orientations of DM haloes and CGs may correlate with the directions of the filaments. We use tidal fields to define directions of the filaments, and examine the time evolution of the alignments of orientations of galaxy clusters relative to the filaments.

5.1 Orientations of dark matter haloes, central galaxies, and the tidal field in the Horizon-AGN simulation

5.1.1 Identification of cluster-sized DM haloes and CGs and their progenitors

In this chapter, we use the same 40 haloes as section 3.1 but we identify their progenitor haloes at 50 different redshifts so as to trace their evolution. The 50 epochs are selected from $z \sim 5$ ($t \sim 1.5$ Gyr) to $z \sim 0$ ($t \sim 13.5$ Gyr) in an equal time interval of $\Delta t \sim 250$ Myr. We make the merger trees of all the 40 cluster-sized DM haloes by using TREEMAKER (Tweed *et al.*, 2009), which first builds the merger history tree, and then connects the haloes with their progenitors.

Once DM haloes are identified at redshift 0, we define the CG in each halo as the most massive galaxy in a halo within 1 pMpc from the most bound particle of each halo (see section 3.1, for more detail). Thus we define the CG at each epoch t by using the CG in the previous epoch $t - \Delta t$. Specifically, we define the CG at each epoch t as a galaxy containing the largest number of stellar particles of the CG in the adjacent snapshot $t - \Delta t$ and is located within 100 pkpc from the most bound particle of each halo at each epoch t. We expect that the CG selected by the above procedure are similar to observed BCGs. Finally we define the "halo centre" by the centre-of-mass of the CG, instead of the centre-of-mass of the DM halo; see equation (5.2) below.

5.1.2 Procedure of ellipsoid fit

Once DM haloes and CGs are identified at each epoch, we fit them to the triaxial ellipsoid model in three-dimensional space following Suto *et al.* (2016), and measure the major, intermediate, and minor axis vectors, $\hat{a}_1$, $\hat{a}_2$, and $\hat{a}_3$, respectively, unlike in chapter 3 that fit the data in the projected two dimensional space.

More specifically, we follow the ellipsoid fitting based on the inertia tensor as described in Suto *et al.* (2016). From all the star particles belonging to the CG, we first compute its centre-of-mass position $x^{\rm CM}_{{\rm CG},\alpha}$ ($\alpha = 1, 2, 3$), and compute the following mass tensor from the star particles located within a sphere of radius 20 pkpc from $x^{\rm CM}_{{\rm CG},\alpha}$:

$$I_{{\rm CG},\alpha\beta}(z) \equiv \frac{\sum_{n=1}^{N_{\rm star}} m^{(n)}_{\rm star} \left[x^{(n)}_{{\rm star},\alpha} - x^{\rm CM}_{{\rm CG},\alpha}\right] \left[x^{(n)}_{{\rm star},\beta} - x^{\rm CM}_{{\rm CG},\beta}\right]}{\sum_{n=1}^{N_{\rm star}} m^{(n)}_{\rm star}}, \tag{5.1}$$

where $m^{(n)}_{\rm star}$ and $x^{(n)}_{{\rm star},\alpha}$ are the mass and the coordinate of the n-th stellar particle ($n = 1, \cdots, N_{\rm star}$).

The above mass tensor is diagonalized and the directions of the major, intermediate, and minor axes are computed. We then select the size of the ellipsoid $R^{\rm star}_{abc} \equiv \sqrt[3]{a_1 a_2 a_3} = 20$ pkpc, where a_1, a_2, and a_3 are the half lengths of the major, intermediate, and minor axes, respectively. We repeat the above procedure using the star particles in the ellipsoid around the update centre-of-mass position $x^{\rm CM}_{{\rm CG},\alpha}$. We choose the value of 20 pkpc as the

size of CGs for definiteness. We confirmed that changing the value to 10 or 30 pkpc does not affect the main conclusion of this chapter (see also section 3.1).

The whole procedure is iterated until the three eigenvalues of the mass tensor converge within a fractional error of 10^{-8}. We then *redefine* the CG as the set of star particles within the ellipsoid of $R^{\rm star}_{abc} = 20$ pkpc, and characterize the CG by the parameters including the half lengths of major axis a_1, intermediate axis a_2, and minor axis a_3 ($a_1 \geq a_2 \geq a_3$), their direction, and the centre of mass $x^{\rm CM}_{{\rm CG},\alpha}$. Therefore the resulting CG is different from the original set of star particles identified with the ADAPTAHOP halo finder.

The shape and orientation of the host DM halo at each z are computed similarly except that we use the mass tensor of DM particles around the centre-of-mass of the CG:

$$I_{{\rm DM},\alpha\beta}(z) \equiv \frac{\sum_{n=1}^{N_{\rm DM}} m_{\rm DM}\left[x^{(n)}_{{\rm DM},\alpha} - x^{\rm CM}_{{\rm CG},\alpha}\right]\left[x^{(n)}_{{\rm DM},\beta} - x^{\rm CM}_{{\rm CG},\beta}\right]}{\sum_{n=1}^{N_{\rm DM}} m_{\rm DM}}, \tag{5.2}$$

where $m_{\rm DM}$ and $x^{(n)}_{{\rm DM},\alpha}$ are the mass and the coordinate of the n-th dark matter particle within the ellipsoid. In this calculation, we use all the dark matter particles including those in subhaloes. Once we fix the size of the ellipsoid, $R^{\rm DM}_{abc} \equiv \sqrt[3]{a_1 a_2 a_3}$, we can compute the total mass and number of DM particles within the ellipsoid, $M_{\rm DM}$ and $N_{\rm DM}$. Unlike in the case of CG, we consider three values of the ellipsoidal bound so that the corresponding to $M_{\rm DM} = 0.1M_{200}$, $0.5M_{200}$, and M_{200}, where M_{200} is the mass of a sphere whose average DM density is 200 times larger than the cosmic critical density at each z.

5.1.3 The tidal field of the large-scale mass distribution

As mentioned in chapter 2, the orientations of DM haloes are correlated to their surrounding matter distribution. Let us expand the gravitational potential of the matter with respect to the centre of a DM halo, $\boldsymbol{x}^{\rm CM}$:

$$\begin{aligned}\Phi(\boldsymbol{x}) = \Phi(\boldsymbol{x}^{\rm CM}) &+ \sum_{\alpha=1}^{3}(x_\alpha - x^{\rm CM}_\alpha)\left(\frac{\partial\Phi}{\partial x_\alpha}\right)_{\boldsymbol{x}=\boldsymbol{x}^{\rm CM}} \\ &+ \frac{1}{2}\sum_{\alpha,\beta=1}^{3}(x_\alpha - x^{\rm CM}_\alpha)(x_\beta - x^{\rm CM}_\beta)\left(\frac{\partial^2\Phi}{\partial x_\alpha \partial x_\beta}\right)_{\boldsymbol{x}=\boldsymbol{x}^{\rm CM}} \\ &+ \cdots .\end{aligned} \tag{5.3}$$

The third term in equation (5.3) describes the tidal field around the DM halo and is responsible for its ellipsoidal growth. If we define the tidal field tensor:

$$T_{\alpha\beta} = \frac{\partial^2\Phi}{\partial x_\alpha \partial x_\beta}, \tag{5.4}$$

its eigen-vectors and eigen-values characterize the direction and relative growth rate of the ellipsoidal evolution of the object.

We compute the tidal field tensor from the simulation data as follows. We first divide the simulation box into 100^3 small grids and assign the DM density field $\rho(\boldsymbol{x})$ at each grid

by a cloud-in-cell interpolation with $\boldsymbol{x}$ being the comoving coordinates of the grid. Next we define the dimensionless density contrast fields:

$$\delta(\boldsymbol{x}) = \frac{\rho(\boldsymbol{x}) - \langle\rho\rangle}{\langle\rho\rangle}, \tag{5.5}$$

where $\langle\rho\rangle$ is the mean density averaged over the entire simulation box. Then the tidal tensor $T_{\alpha\beta}(\boldsymbol{x})$ at each grid is defined by the second spatial derivative of the *smoothed* density contrast. If we adopt a Gaussian smoothing over a scale σ, the Fourier transform of $T_{\alpha\beta}(\boldsymbol{x})$ is easily computed as

$$\tilde{T}_{\alpha\beta}(\boldsymbol{k}) = \frac{k_\alpha k_\beta}{|\boldsymbol{k}|^2}\tilde{\delta}(\boldsymbol{k})\exp\left(\frac{-|\boldsymbol{k}|^2\sigma^2}{2}\right), \tag{5.6}$$

where k_α and $\tilde{\delta}(\boldsymbol{k})$ are α-th component of the wave-number vector $\boldsymbol{k}$ and the Fourier transform $\delta(\boldsymbol{x})$, respectively. We use the FFTW package to compute the Fourier transform of the tidal field (Frigo & Johnson, 1998, 2005).

Since the spatial extent of cluster-sized haloes is typically $\sim 1\ h^{-1}$cMpc, we choose σ =3, 5, and 10 h^{-1}cMpc as the smoothing scale so that the corresponding tidal tensor traces the large-scale structure surrounding those haloes. Then, we compute the inverse Fourier transform of $\tilde{T}_{\alpha\beta}(\boldsymbol{k})$ to obtain the tidal tensor $T_{\alpha\beta}(\boldsymbol{x})$. We apply the cloud-in-cell interpolation of the tidal tensors at the nearby grids to obtain the tidal tensor defined at the centre of the CG that is assumed to be the centre of the host DM halo as well.

Finally, we diagonalize the tidal field tensor to obtain the normalized eigenvectors, $\hat{u}_\alpha$ ($\alpha = 1, 2,$ and 3), and the corresponding eigenvalues with λ_1, λ_2, and λ_3 of $\lambda_1 \geq \lambda_2 \geq \lambda_3$. In particular, $\hat{u}_3$ corresponds to the direction of the slowest collapsing or the fastest expanding mode, and expected to be correlated to the major axis of the object located at the centre. Previous studies (e.g., Hahn *et al.*, 2007; Lee, 2019) found that the set of eigenvalues roughly corresponds to the structure defined at the location as follows;

(i) clusters ($\lambda_1 > 0$, $\lambda_2 > 0$, and $\lambda_3 > 0$),
(ii) filaments ($\lambda_1 > 0$, $\lambda_2 > 0$, and $\lambda_3 < 0$),
(iii) sheets ($\lambda_1 > 0$, $\lambda_2 < 0$, and $\lambda_3 < 0$),
(iv) voids ($\lambda_1 < 0$, $\lambda_2 < 0$, and $\lambda_3 < 0$).

We confirmed that for $\sigma = 10\ h^{-1}$cMpc 11 of our haloes are classified as "clusters", and the remaining 29 haloes are as "filaments" according to the above classification.

5.2 An example of the ellipsoid fit

In this section, we select the most massive single-core-dominated halo from the 40 haloes in our sample, which is the same as plotted in Figures 3.1 and 3.4. Figure 5.1 shows the evolution of the mass of the DM halo and CG (top), the ratios of their major and minor axes a_3/a_1 (middle), and the angles between their major axes (bottom). The masses of the DM halo and CG are plotted in blue and red, respectively, in the top panel. The axis ratios, a_3/a_1, are computed for the ellipsoids enclosing those masses and plotted in the

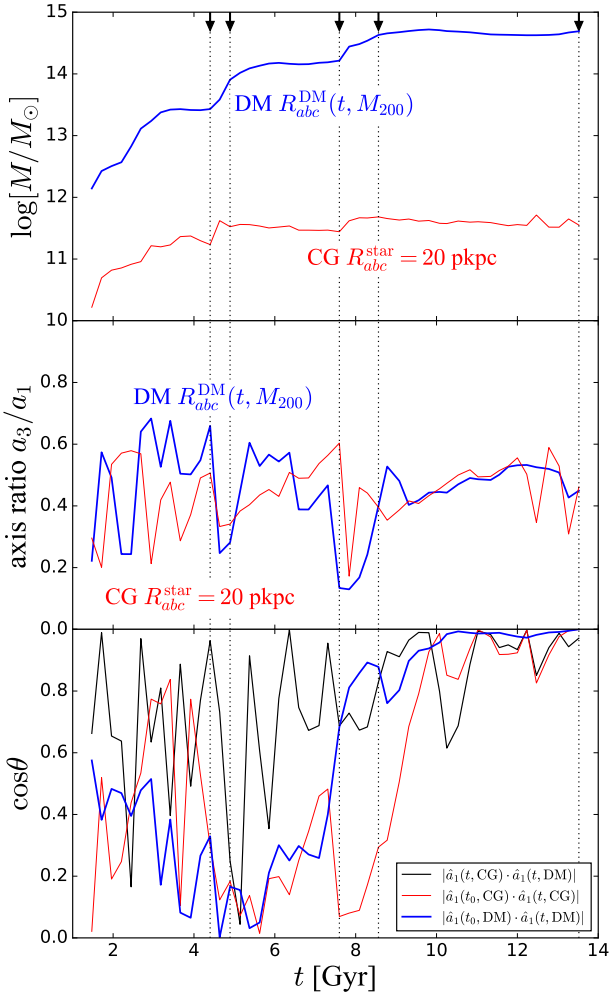

Figure 5.1. Top: The redshift evolution of the DM mass M_{200} (thick blue) and mass of the CG within 20 pkpc (thin red) for an example of one halo shown in Figure 5.2. Vertical dotted lines correspond to five epochs shown in Figure 5.2. Middle: The redshift evolution of major-to-minor axis ratios a_3/a_1 of fitted ellipsoids both for the DM and for the CG. Bottom: Alignment angles between orientations of the CG and the DM halo at each epoch (black), orientations of the DM at the present epoch and in the past (thick blue), and orientations of the CG at the present epoch and in the past (thin red).

same colour, respectively. The bottom panel plots absolute values of the three direction cosines of the different major axes. The black line is computed from $\hat{a}_1$ of the CG and the DM halo at the same epoch t. The red and blue lines are computed from $\hat{a}_1$ defined at t and the present epoch t_0 for the CG and the DM halo, respectively.

We choose five redshifts (indicated by the vertical dotted lines) to investigate the snapshots in more detail; before and after two major merger events ($z = 1.49$, 1.31, 067, and 0.52) and at present ($z \approx 0$). The signature of the mergers is clearly seen in the top panel of Figure 5.1, where the DM halo mass significantly increases. The first and second

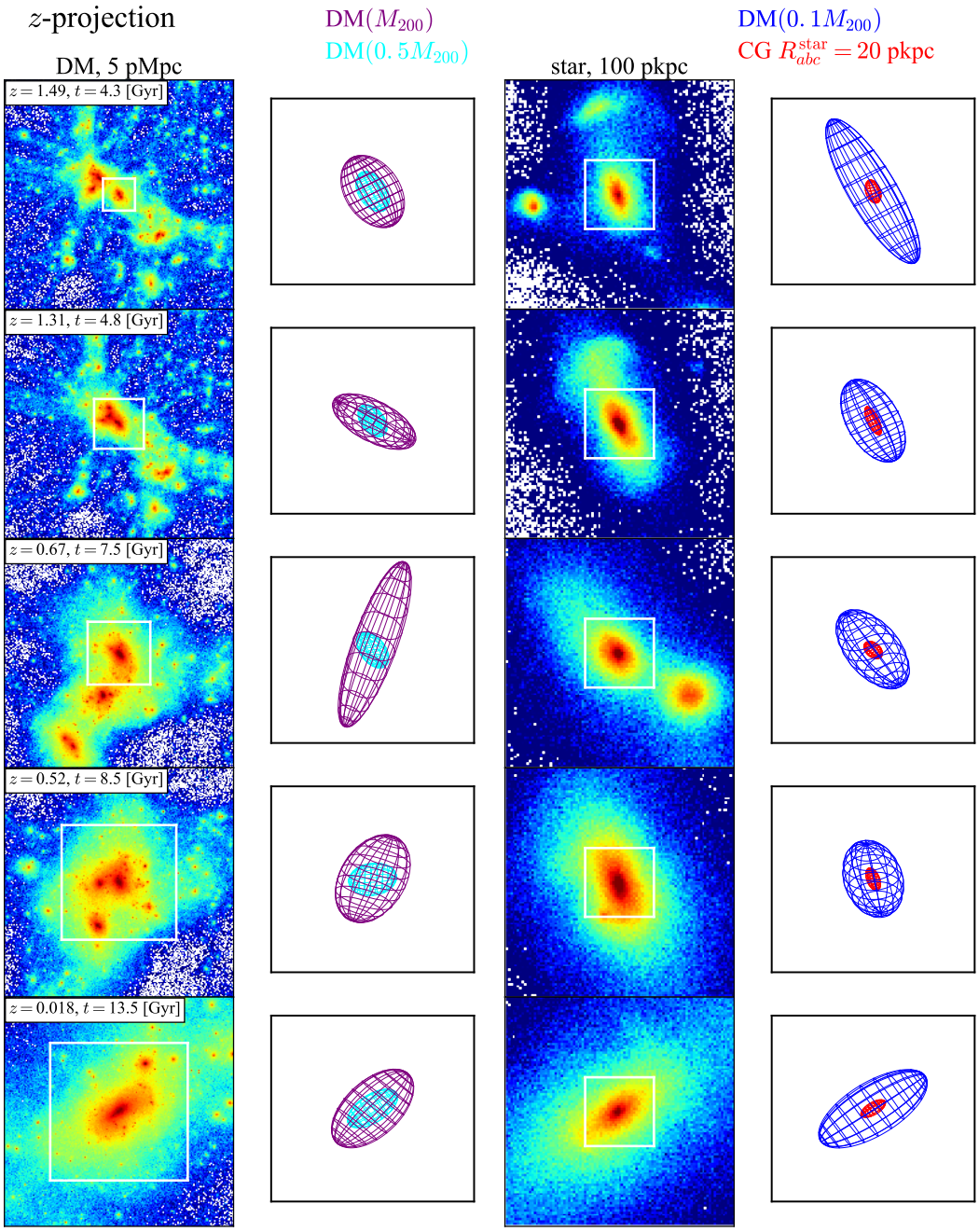

Figure 5.2. From left to right, we show images projected along the z-direction of the Horizon-AGN simulation box of DM particles within a $(5\ \mathrm{pMpc})^3$ cube, fitted ellipsoids of DM for the enclosed mass of M_{200} (purple) and $0.5M_{200}$ (cyan), stellar particles within a $(100\ \mathrm{pkpc})^3$ cube, and the ellipsoids of the DM for $0.1M_{200}$ (blue) and CG (red), respectively. From top to bottom, the images correspond to those at $z = 1.49$ ($t = 4.3$ Gyr), $z = 1.31$ ($t = 4.8$ Gyr), $z = 0.67$ ($t = 7.5$ Gyr), $z = 0.52$ ($t = 8.5$ Gyr), and $z = 0.018$ ($t = 13.5$ Gyr), respectively. These five epochs are also indicated by vertical dotted lines in Figure 5.1.

columns in Figure 5.2 show the surface density of dark matter component and the corresponding ellipsoids projected along the z-axis, respectively. At each redshift, we extract a cube of (5 pMpc)^3 around the centre of the CG of that halo. The white squares in the first column indicate the box square in the second column. Similarly, we extract a cube of (100 pkpc)^3 around the centre of the CG, and plot the surface density of stellar component and the corresponding ellipsoids in the third and fourth columns, respectively.

Figure 5.1 indicates that masses, axis ratios, and orientations of those objects did not change much after the last major merger around 8 Gyr. Before the epoch, the axis ratios and the orientations change significantly, presumably due to repeated mergers or mass accretion events during the growth of the halo. In particular, the shape of the DM halo became very elongated at the two major merger events, leading to rapid changes of a_1 during the mergers. This also leads to the enhancement of the angular momentum amplitude during the merger episode (Peirani *et al.*, 2004). While there are large variations between the orientations of the CG and the host DM halo, they are relatively well aligned at each epoch (black line in the bottom panel), and evolve coherently toward their current direction (blue and red lines).

The above features are visually illustrated in Figure 5.2. The major merger between $z = 1.49$ and 1.31 proceeded through the mass accretion along the upper-left to lower-right filamentary structure. Thus the major axes of the DM haloes and CG follow the direction of the filament and do not change much, even though their ellipticities, in particular at the outer boundary, significantly change during the merger event. A similar trend is seen at the next major event between $z = 0.67$ and 0.52.

After $z = 0.52$ ($t = 8.5$ Gyr), the DM halo did not experience any violent merger (see the top panel of Figure 5.1), and the axis ratio and direction of the major axis of the outer boundary of the DM halo (corresponding to M_{200}) are fairly constant until the present epoch. The orientations of the inner DM haloes defined at $0.1M_{200}$ and $0.5M_{200}$ and the CG gradually became aligned toward that of the outer DM halo.

The evolution history of this specific halo presented in Figures 5.1 and 5.2 is summarized as follows. The DM halo grows through sequences of repeated mergers and mass accretions following the surrounding large-scale structure, in particular along the nearby filamentary structures. The shape and orientation of the DM halo are significantly affected by those events, whereas they did not evolve much after the last major merger around 8 Gyr. The inner part of the DM halo and CG evolves rather coherently so that their major axes become aligned better toward that of the outer DM halo, which is basically fixed just after the last major event.

It is not clear, however, to what extent the above simple picture is applicable to other DM haloes and CGs as well in general. Therefore we analyse the orientations of all the 40 haloes and study the statistical evolution behavior in the next section.

5.3 Statistical correlation among orientations of DM haloes, CGs, and surrounding tidal field

In order to examine the validity of a simple picture emerging from the evolution of the particular halo presented in the previous section, we consider three different aspects of the statistical correlation over 40 simulated haloes; (i) instantaneous correlation of orientations between CGs and DM haloes, (ii) evolution of the orientation of CGs and DM haloes towards their present values, and (iii) statistical correlation and evolution of their orientation with respect to the surrounding tidal field. As we will show below, those results indicate that the orientations of DM haloes at the present epoch are basically imprinted in the initial conditions of the large-scale structure, while the orientations of CGs drastically evolve with time due to mergers and mass accretions.

5.3.1 Instantaneous correlation of orientations between the CGs and DM haloes

We first examine to what extent the orientations of CGs are aligned to that of the host DM haloes instantaneously. For that purpose, we compute the direction cosines between the unit vectors along the major axes of CGs and DM haloes at the same epoch, and then average them over the entire 40 haloes:

$$\langle \cos\theta \rangle (t; \mathrm{CG}-\mathrm{DM}) \equiv \frac{1}{N_{\mathrm{cl}}} \sum_{i=1}^{N_{\mathrm{cl}}} \left| \hat{a}_1^{(i)}(t, \mathrm{CG}) \cdot \hat{a}_1^{(i)}(t, \mathrm{DM}) \right| . \tag{5.7}$$

Figure 5.3 plots equation (5.7) for CGs against their host DM haloes defined at the mass scale of M_{200} (blue-solid line) and $0.1M_{200}$ (cyan-dotted line). Since equation (5.7) should reduce to 0.5 (or $\cos^{-1}(0.5) = 60^\circ$) if the two major axes are uncorrelated and randomly oriented, Figure 5.3 indicates that the major axes of CGs are always positively aligned to those of their host DM haloes. In order to see the evolution of the above alignment more clearly, we plot their cumulative probability density functions in Figure 5.4 at 50 epochs. The alignment between CGs and their host DM haloes becomes more tightly aligned toward the present epoch.

As expected, CGs are correlated more strongly with the inner part of the DM haloes at any epoch, with a mean relative angle less than $\cos^{-1}(0.8) \approx 40^\circ$. This result is qualitatively consistent with the observational claim by West *et al.* (2017) that orientations of BCGs and their host DM haloes are aligned even at $z > 1.3$ ($t < 5$ Gyr). It is not easy, however, to compare our results with West *et al.* (2017) quantitatively, partly because cluster masses of the West *et al.* (2017) sample are $M_{\mathrm{vir}} \sim 10^{15}\ M_\odot$, whereas masses of our sample are $M_{200} \sim 10^{14}\ M_\odot$. We also find that the correlation with DM haloes increases gradually on average toward the present epoch. The average alignment angles between CGs and the outer boundary of DM haloes at M_{200} are $\approx \cos^{-1}(0.70) = 45^\circ$ before $t = 8$Gyr and $\approx \cos^{-1}(0.82) = 35^\circ$ at present (see also chapter 3), respectively.

Since the angles are observationally measurable only in the projected two dimensional

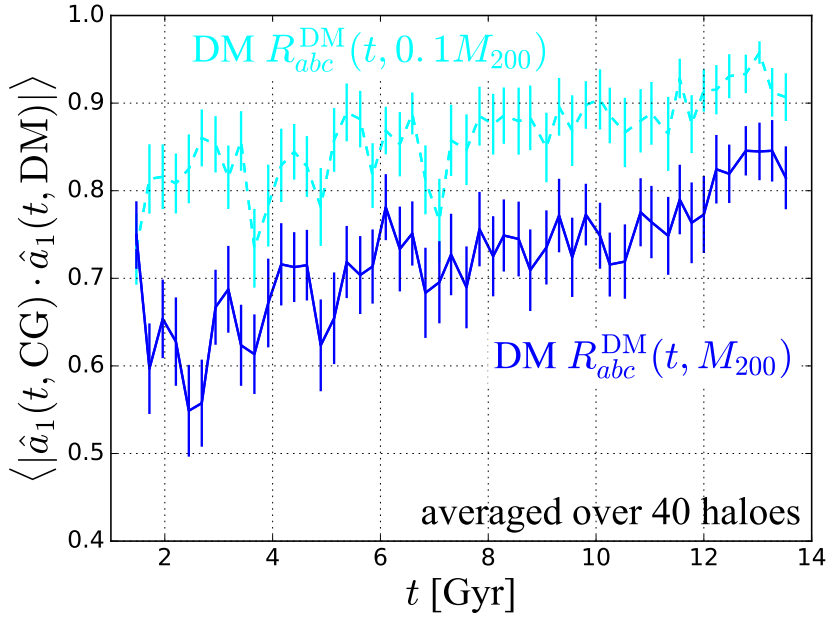

Figure 5.3. Correlation between orientations of CGs and DM haloes evaluated at the same epoch. Dashed cyan and solid blue lines indicate the direction cosine between CGs and DM haloes for enclosed masses of $0.1M_{200}$ and M_{200}, respectively, averaged over 40 haloes. The error bars correspond to the determination accuracy of the mean values defined as the standard deviation divided by the square root of the number of haloes, $N_{\rm cl} = 40$.

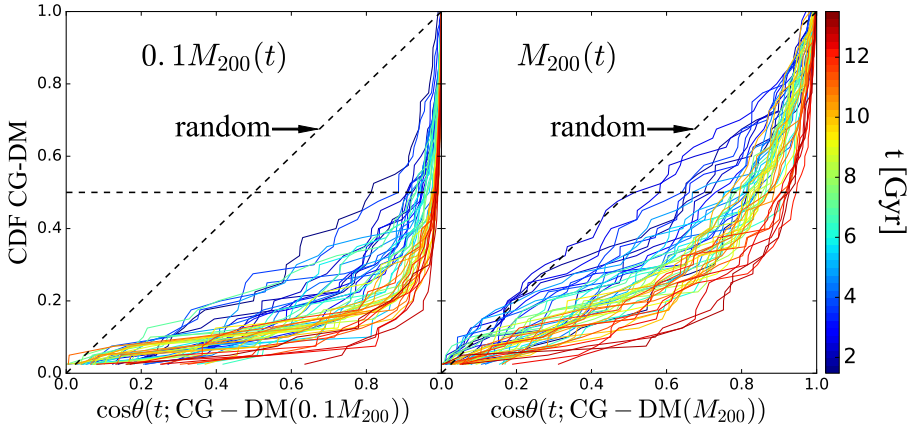

Figure 5.4. Cumulative probability distributions of alignment angles between orientations of DM haloes and CGs at each epoch t. Left and right panels show results for DM haloes with the enclosed mass $0.1M_{200}$ and M_{200}, respectively. Colour scale corresponds to the cosmic time, bluer lines are earlier and redder lines are later.

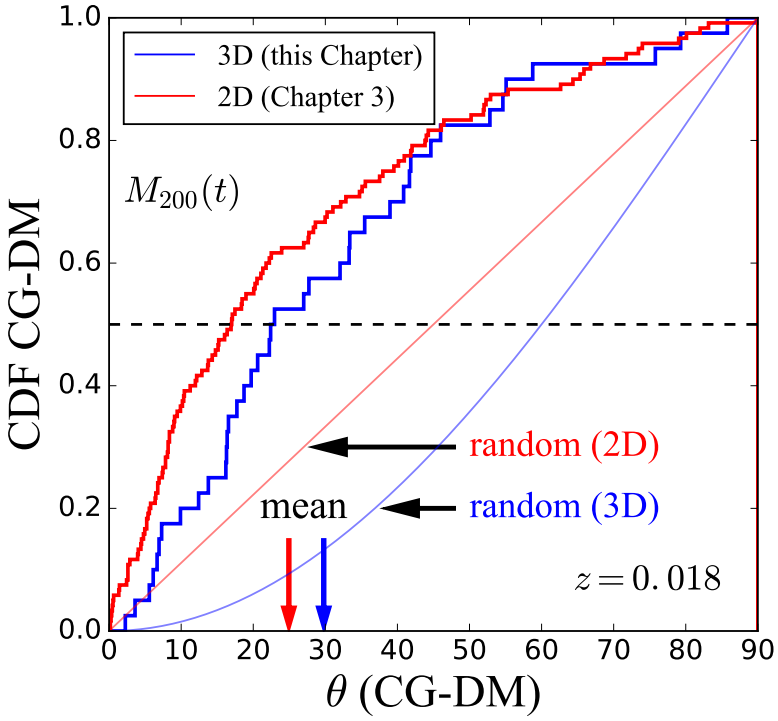

Figure 5.5. Cumulative probability distributions of alignment angles θ between orientations of DM haloes and CGs at present epoch $z = 0.018$. Blue and red thick lines correspond to the alignment angles of three dimensional (3D) fit (this chapter) and two dimensional (2D) fit (chapter 3), respectively. The angles θ of 3D fit is the same as the right panel in Figure 5.4. The angles θ of 2D fit is the same of the bottom right panel in Figure 3.9. Red and blue thin lines correspond to the cumulative probability distribution of the random distributions. Mean values of θ for both the 3D and 2D are shown with arrows.

plane, Figure 5.5 compares the cumulative distribution of the angles defined in three dimensional space (see Figure 5.3) with those similarly defined after projected along either x, y, or z direction in the simulation coordinates at $z \approx 0$. This plot helps understanding the connection between the three dimensional angles studied in this chapter and observable two dimensional angles.

5.3.2 Evolution of orientations of CGs and DM haloes towards the present time

We consider next how the orientations of CGs and DM haloes become aligned towards their present values. Figure 5.6 plots

$$\langle \cos\theta \rangle (t, t_0; \mathrm{X}) \equiv \frac{1}{N_{\rm cl}} \sum_{i=1}^{N_{\rm cl}} \left| \hat{a}_1^{(i)}(t, \mathrm{X}) \cdot \hat{a}_1^{(i)}(t_0, \mathrm{X}) \right| \tag{5.8}$$

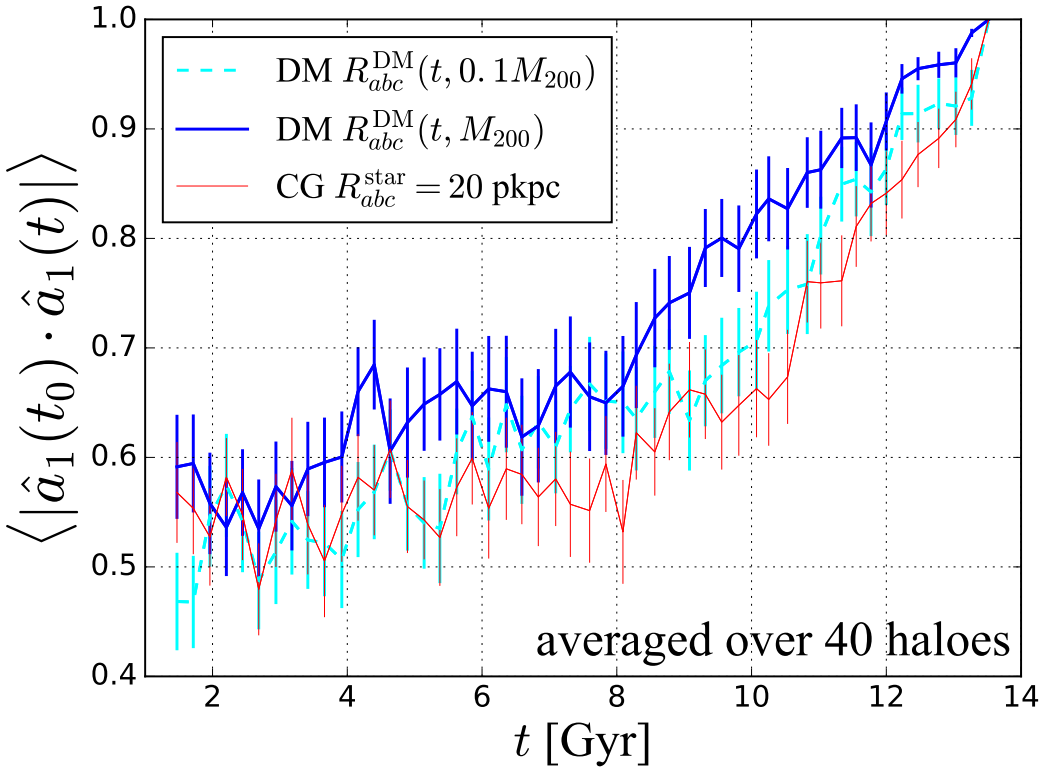

Figure 5.6. Correlation between orientations of objects at t and the present epoch t_0 for the three components; Red-thin line is for CGs, and cyan-dashed and blue-solid lines are for DM haloes with enclosed masses of $0.1M_{200}$ and M_{200}, respectively. The quoted error-bars represent the root mean square value divided by $\sqrt{N_{\rm cl}}$.

for the three components, X=CG (red-thin solid) and DM haloes of $0.1M_{200}$ (cyan-dashed) and M_{200} (blue-solid).

Orientations of the major axes of those objects at early epochs ($t \leq 4$ Gyr) are quite different from the ones at the present time; the average alignment angles $\theta(t, t_0)$ are somewhere between 50° and 60°, corresponding to $\cos^{-1}(0.6)$ and $\cos^{-1}(0.5)$. This result confirms the scenario presented in section 5.2: orientations of both DM haloes and CGs change drastically with time. The correlation of each component increases gradually and steadily toward the present epoch, in particular, at $t > 8$ Gyr.

Since Figure 5.6 may suggest a possible break of the correlation curves around $t = 8$ Gyr, we examined both the occurrence rate of the last major merger events and the cluster mass growth history for the 40 haloes individually. However, they seem to be fairly continuous around $t = 8$ Gyr, and therefore we do not think that this epoch has any particular physical meaning. On the other hand, it corresponds approximately to the median epoch when the mass of each cluster exceeds the half of its current value. This may explain why orientations of both DM haloes and CGs remain close to their present

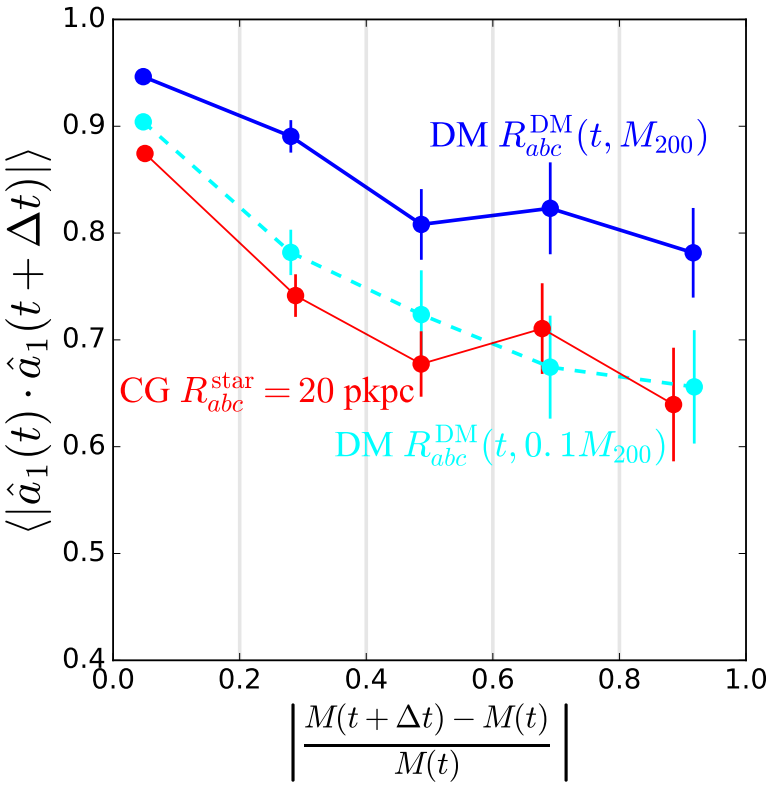

Figure 5.7. Correlations between changes of orientations and those of masses during the time interval $\Delta t = 250$ Myr. We take the absolute values of the fractional mass differences because large negative values correspond to flyby galaxies that are below the detection threshold of the galaxy finder and detach after their passage, and therefore negative values are similar to mergers with large positive values. For each bin of the fractional mass difference, we show the average and error of direction cosines of major axes of neighboring epochs. To compute the averages and the errors, we use all the 40 haloes and 49 snapshot pairs for each halo. The quoted error-bars represent the root mean square value divided by the square root of the number of corresponding objects in each bin. Red-thin line is for CGs, and cyan-dashed and blue-solid lines are for DM haloes with enclosed masses of $0.1M_{200}$ and M_{200}, respectively.

ones at $t > 8$ Gyr.

Figure 5.6 also appears to indicate that the orientations of the outer DM haloes first become aligned closer to its present value, followed by that of the inner DM haloes, and then by that of CGs. This result suggests that the alignment proceeds from larger to smaller scales. Therefore those orientations and their mutual alignment may be determined by the surrounding larger-scale structure.

Figure 5.6 implies that the change of orientations between DM haloes and CGs is driven by strong dynamical interactions through successive mergers and mass accretion episodes. To check this point more explicitly, in Figure 5.7 we show the correlation between fractional mass changes and changes of orientations at neighboring snapshots with a time

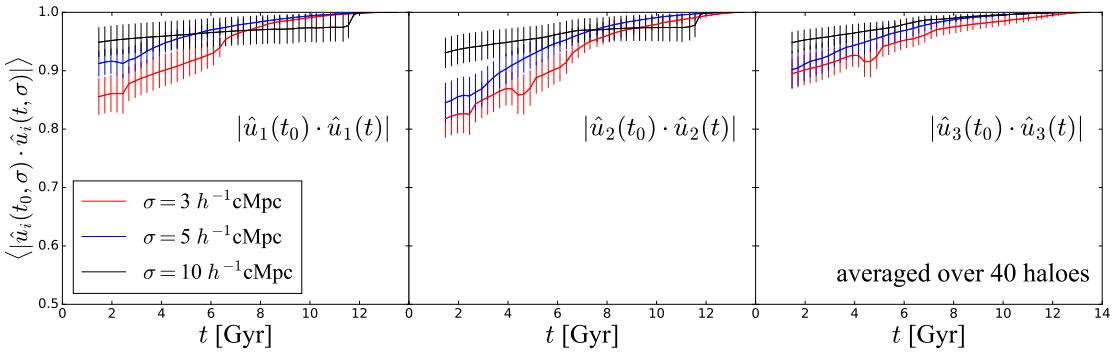

Figure 5.8. Correlation between the eigenvectors of the tidal field at t and the present epoch t_0. They are computed from a density field Gaussian-smoothed over $\sigma = 3h^{-1}$ (red), $5h^{-1}$ (blue), and $10h^{-1}$ (black) cMpc; see section 5.1.3 for further details. The eigenvectors are labelled as $\hat{u}_1$, $\hat{u}_2$, and $\hat{u}_3$ corresponding to the largest, medium, and smallest eigenvalues. Their correlations $|\hat{u}_\alpha(t_0)\cdot\hat{u}_\alpha(t)|$ averaged over the 40 halo locations are plotted for $\alpha = 1$, 2 and 3 in the left, centre and right panels, respectively. The quoted error-bars represent the root mean square value divided by $\sqrt{N_{\rm cl}}$. The sudden change at ~ 12 Gyr in the left and middle panels is due to an outlier cluster whose eigenvectors suddenly change at that epoch.

interval of $\Delta t = 250$ Myr. Figure 5.7 indicates that changes of orientations are large when fractional mass differences are large, which correspond to mergers and large mass accretions, both for DM haloes and CGs. This suggests that the spin swings of both DM haloes and galaxies are mainly driven by their mergers and mass accretions, while they are also affected by the later re-distribution of the angular momentum vector inside them. This picture is qualitatively consistent with the result of Welker *et al.* (2014).

5.3.3 Orientations of DM haloes and CGs with respect to the surrounding large-scale structure

The results presented in the previous subsections imply that the large scale environment is responsible for the orientations and the alignments of CGs and their host DM haloes. Thus we choose the orientations of the eigenvectors of the tidal field as a proxy of the directions embedded in the large scale structure, which may keep the memory of the initial conditions.

Figure 5.8 plots the correlation of the three eigenvectors $\hat{u}_\alpha$ computed at each epoch (t) and the present epoch (t_0). We apply three different smoothing lengths, $\sigma = 3h^{-1}$, $5h^{-1}$, and $10h^{-1}$ cMpc, and compute the eigenvectors at the location of CGs according to the procedure described in section 5.1.3. As is clear from Figure 5.8, those eigenvectors do not change so much over the cosmic time.

In particular, directions of the tidal field eigenvectors with $\sigma = 10\ h^{-1}$cMpc are fairly constant over ~ 10 Gyr. Since $10\ h^{-1}$cMpc is sufficiently larger than the size of the typical

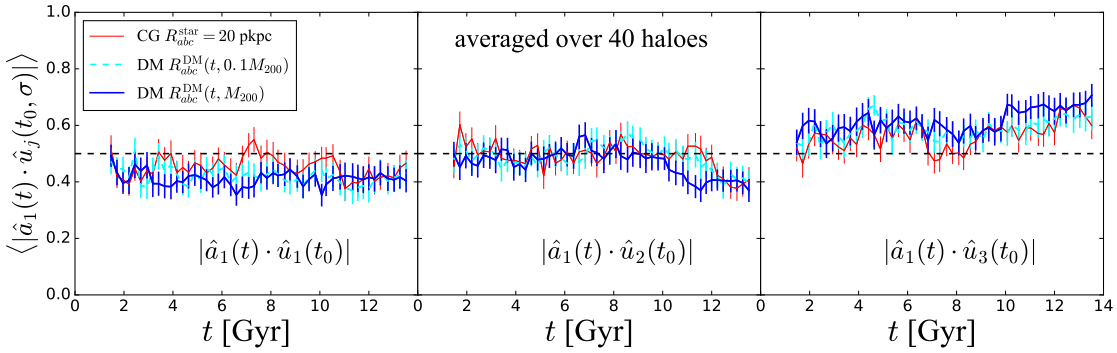

Figure 5.9. Mean values of alignment angles between orientations of haloes at each epoch t and eigenvectors of the tidal field at the present epoch t_0. Left, middle, and right panels show the alignments of halo orientations with respect to eigenvectors $\hat{u}_1$, $\hat{u}_2$, and $\hat{u}_3$, respectively. Dashed cyan, thick blue, and thin red lines indicate median alignment angles of DM haloes for enclosed masses of $0.1M_{200}$, M_{200}, and those of CGs, respectively. The quoted error-bars represent the root mean square value divided by $\sqrt{N_{\rm cl}}$. The smoothing scale of the tidal field is set to $\sigma = 10\ h^{-1}$cMpc.

cluster-sized haloes and less than the typical separation ($\sim 30\ h^{-1}$cMpc) of the nearest cluster-sized halo, we choose $10h^{-1}$ cMpc as the smoothing length in the following analysis, and adopt $\hat{u}_\alpha(t_0;\sigma = 10\ h^{-1}\text{cMpc})$ defined at the CG's location as a set of proxies for the preferential directions imprinted in the large-scale structure surrounding those haloes.

In order to see the relation of the orientations of objects and the surrounding environment, we compute the correlations of the major axis direction of $\hat{a}_1(t;\mathrm{X})$, where $X = \mathrm{CG}$, inner DM halo, and outer DM halo, against the eigenvectors of the tidal field $\hat{u}_\alpha(t_0)$ averaged over the 40 halo locations. Figure 5.9 plots $\langle|\hat{a}_1(t)\cdot\hat{u}_\alpha(t_0)|\rangle$ as a function of t for $\alpha = 1$, 2, and 3 in the left, centre, and right panels, respectively. Each panel has three curves corresponding to the three objects; CG (red), inner DM halo (cyan) and outer DM halo (blue). The major axes of the three objects exhibit positive and negative correlations with $\hat{u}_3(t_0)$ (~ 0.6) and $\hat{u}_1(t_0)$ (~ 0.4), respectively, relative to the random distribution. The intermediate axis of the tidal field, on the contrary, is almost uncorrelated (~ 0.5) with the major axis of the objects, although they tend to become weakly negative correlated gradually toward the present epoch (~ 0.4).

In order to see the evolution of the above alignment more clearly, we plot the cumulative probability density functions in Figure 5.10. The upper and lower panels show those for DM haloes and CGs against $\hat{\boldsymbol{u}}_1$ (left), $\hat{\boldsymbol{u}}_2$ (centre), and $\hat{\boldsymbol{u}}_3$ (right). Each curve represents the cumulative probability density function at t according to the colour-bar shown to the right. The diagonal dotted line indicates the completely random distribution. Positive and negative correlations correspond to the convex and concave curves in Figure 5.10, respectively.

As we have seen in Figure 5.9, the major axes of DM haloes evolve preferentially toward the direction of $\hat{\boldsymbol{u}}_3(t_0)$. The major axes of DM haloes tend to be away from $\hat{\boldsymbol{u}}_1(t_0)$ in a

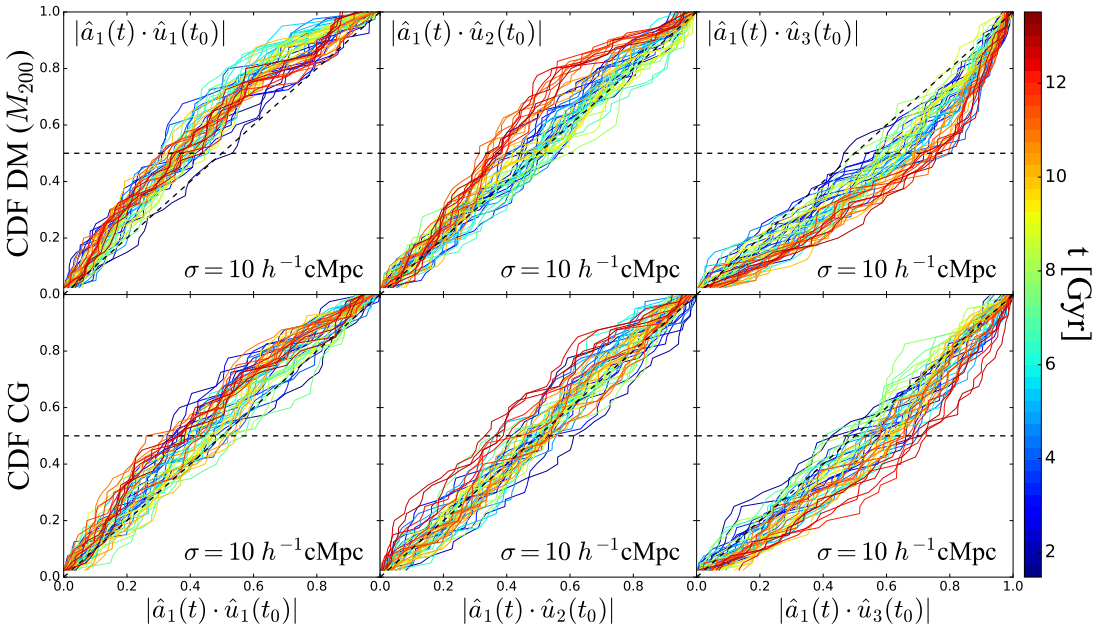

Figure 5.10. Cumulative probability distributions of alignment angles between orientations of haloes at each epoch t and eigenvectors of the tidal field at the present epoch t_0. Top and Bottom panels show results for dark matter haloes with the enclosed mass M_{200} and for CGs, respectively. Left, middle, and right panels show the position angles of $\hat{u}_1$, $\hat{u}_2$, and $\hat{u}_3$ relative to $\mathrm{a}_1(t, \mathrm{DM})$, respectively. Colour scale corresponds to the cosmic time, bluer lines are earlier and redder lines are later. The smoothing scale of the tidal field of $\sigma = 10\ h^{-1}$cMpc is adopted.

time-independent manner. They are fairly uncorrelated with $\hat{\boldsymbol{u}}_2(t_0)$ at the early epochs, but develop weak correlation toward the present epoch. The correlation of CGs against the tidal field are weaker than that of DM haloes, but exhibits qualitatively a similar trend. This is consistent with the fact that 11 and 29 out of our 40 clusters correspond to "clusters" and "filaments", respectively, according to the definition in section 5.1.3 (e.g. Hahn *et al.*, 2007).

Bate *et al.* (2019) have studied in particular the evolution of alignments of massive elliptical galaxies relative to the tidal field. They find that the alignments are tighter for $\hat{u}_1$ and $\hat{u}_3$ than for $\hat{u}_2$, and also that the alignments increase from $z = 3$ to 0. These two findings are consistent with our results.

5.4 Summary

In this chapter, we explore the origin of alignments between orientations of BCGs and their host DM haloes by tracing their cosmic evolutions. We use the same 40 cluster-sized

DM haloes and CGs in chapter 3 and identify their progenitors at 50 different epochs from $z = 5$ to 0. We then fit their shapes and orientations with a triaxial ellipsoid model following Jing & Suto (2002).

While the orientations of both DM haloes and CGs change significantly due to repeated mergers and smooth mass accretion episodes, their relative orientations are well aligned at each epoch even at high redshifts, $z > 1$. The result is qualitatively consistent with observations of West *et al.* (2017), who reported the mutual alignment between orientations of BCGs and clusters even at high redshift, $z > 1.3$ ($t < 5$ Gyr). The alignment becomes tighter with cosmic time; the major axes of the CGs and their host DM haloes at present are aligned on average within 30 deg in three dimensional space and ~ 20 deg in the projected plane. We also compute the eigen-vectors of the tidal field centred at the location of CG in each halo with smoothing scale of 10 h^{-1} cMpc. The orientations of the major axes of DM haloes on average follow one of the eigen-vectors of the surrounding tidal field that corresponds to the *slowest collapsing* (or even stretching) mode, and the alignment with the tidal field also becomes tighter.

A picture of the evolution of the orientations of CGs and DM haloes emerging from our current study is summarized as follows (see Figure 5.11 for a schematic picture). Even at early epochs, $t = 2$ Gyr, orientations of the CG and its host DM halo in an individual system exhibit weakly correlation in a statistical sense. The orientations of both the CG and its host DM halo significantly change due to mergers and mass accretion episodes. However, the orientations of the CG and host DM halo change coherently and evolve together toward their current orientations that are more tightly correlated with the surrounding large-scale matter distribution $\hat{u}_3(t_0)$ than at early epochs. This implies that the instantaneous alignment between the DM halo and the CG is driven by strong dynamical interactions through repeated mergers and mass accretion episodes.

Finally, the major axes of both galaxy clusters and CGs tend to be aligned with preferred directions of surrounding matter distributions such as filaments. This can be interpreted as the mass accretion episodes happen statistically more often from the directions of surrounding matter distributions. As a result, the alignments become tighter with time and then the strong alignments at present epoch have been generated. Indeed the CG evolves following that of the host DM halo and becomes tightly aligned with each other; their typical angles are $< 30^\circ$ and $< 20^\circ$ in the three dimensional space and in the projected plane, respectively, at the present epoch.

The above basic picture is visually illustrated in Figure 5.12. Each panel depicts the simulation box of $(100\ h^{-1}\mathrm{cMpc})^3$ projected along the z-axis of the simulation. The grey scale represents the surface density of DM particles on $(1\ h^{-1}\mathrm{cMpc})^2$ cells at $z = 1.97$ (top), 0.67 (centre) and 0.16 (bottom). Green bars in the left panels and red bars in the right panels indicate the eigen-vector $\hat{u}_3(t)$ of the tidal field and the major axis $\hat{a}_1(t)$ of CGs projected on each x-y plane, whereas blue bars in all the panels are the projected major axis $\hat{a}_1(t)$ of DM haloes at epochs around the redshift of each panel. The green bars are roughly aligned along the filamentary structure and do not change so much. The blue bars seem to be aligned with the green bars gradually with time, and the tendency

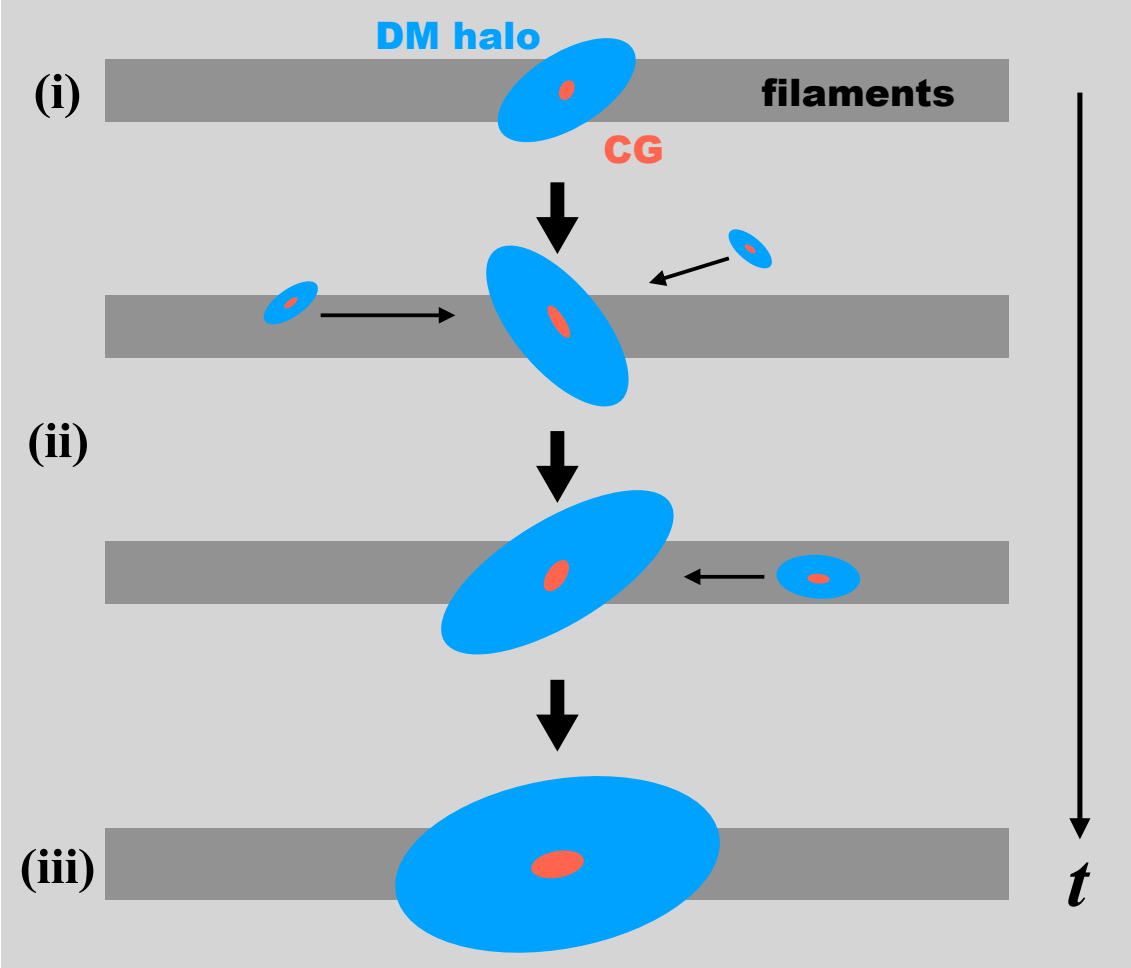

Figure 5.11. A schematic picture of evolution of alignment between CG and DM halo in a galaxy cluster. (i) Orientations of CG and DM halo are weakly aligned with each other. (ii) Orientations of CG and DM halo are changed significantly by repeated mergers and mass accretion episodes, but the major axes of them remain to be aligned with each other even after the mass accretions. (iii) Orientations of both CG and DM halo tend to be aligned with preferred directions of the filament.

of the mutual alignment is stronger between the blue and red bars, i.e., DM haloes and CGs.

In this chapter, we present the predicted evolution of alignments between BCGs, DM haloes, and the large-scale structure, which should be confronted with observations. A caveat is that we focused on the evolution of the same halo over the cosmic time whose mass is different at different epochs (see Figure 5.1). Such difference of masses should be taken into account for a fair comparison with observations (Lin *et al.*, 2017). The survey result by Hyper Suprime-Cam Survey (Aihara *et al.*, 2018) would be useful for examining the redshift evolution of the alignment between orientations of BCGs and clusters because it covers a large (~ 1000 deg^2) and deep ($z \sim 1.1$) area (Oguri *et al.*, 2018).

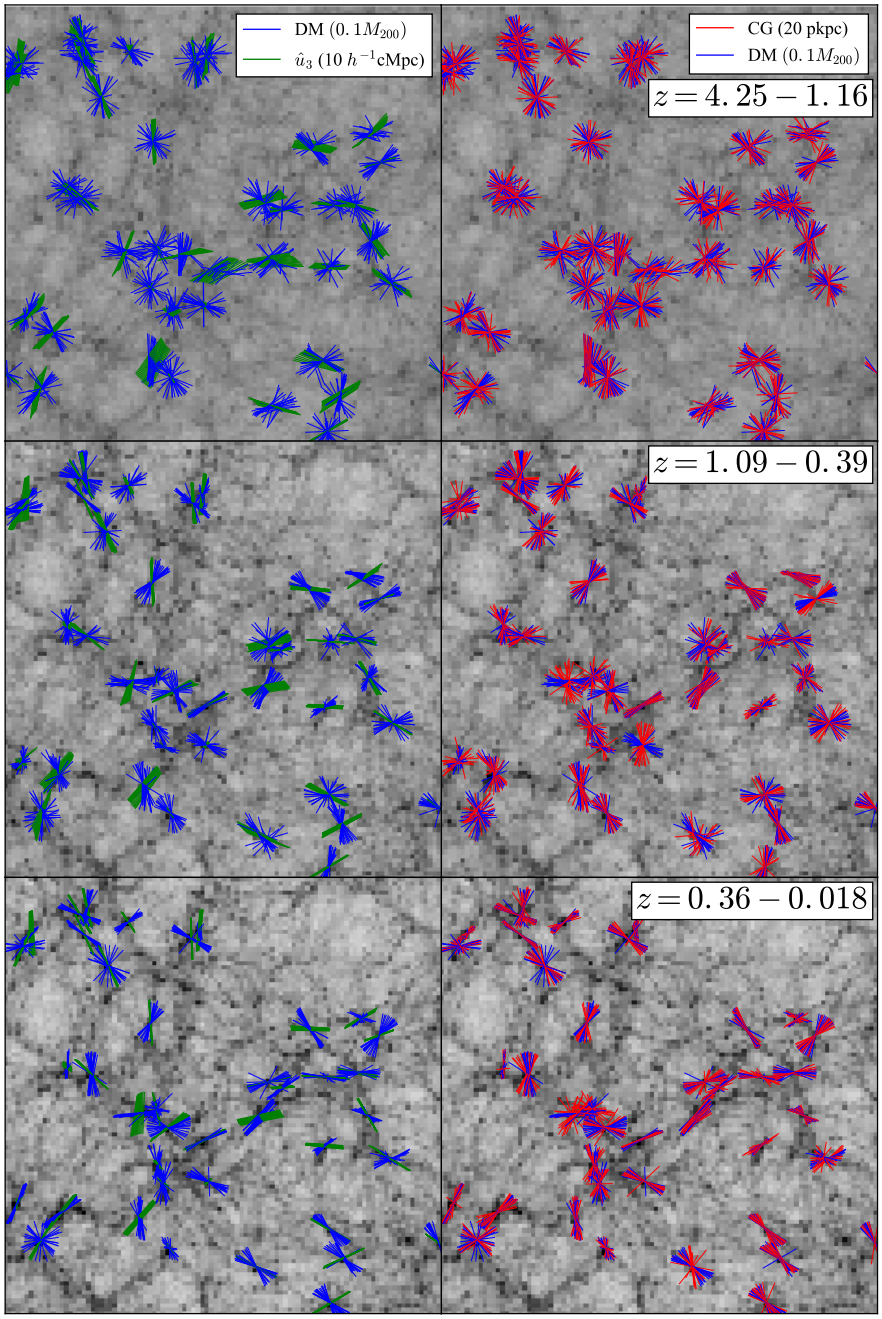

Figure 5.12. Projected mass density fields of DM and the orientations of CGs (red), DM haloes for the enclosed mass of $0.1M_{200}$ (blue), and the tidal field eigenvectors $\hat{u}_3$ (green) for early (top panel, $z = 4.25$-1.16, $t = 1.5$-5.4 Gyr), middle (middle panel, $z = 1.09$-0.39, $t = 5.6$-9.6 Gyr), and late (bottom panel, $z = 0.36$-0.018, $t = 9.8$-13.5 Gyr) epoch. In each panel, all the eigenvectors in the redshift range are shown. The size of each panel corresponds to the simulation box size, 100 h^{-1}cMpc. Lengths of lines indicate orientations with respect to the projection, long lines are nearly perpendicular to the line of sight and short lines are nearly parallel to the line of sight, respectively. Grey scales correspond to the surface mass density of DM which are computed by the projection of all particles in the simulation box at middle time for each panel $t = 1.97$ (top), $t = 0.67$ (middle), $t = 0.16$ (bottom) Gyr, respectively.

Chapter 6

Summary and conclusions

In this thesis, we focus on non-sphericity of galaxy clusters and central galaxies (CGs), especially the ellipticity and the orientation, and investigate systematically to what extent they correlate. The new point of this thesis is to conduct a comprehensive study both theoretically and observationally focusing on the non-sphericity of galaxy clusters. Although to carry out simulations incorporating baryon physics is essential to theoretically investigate physical quantities related to CGs, such simulations have been difficult for a long time. Since recently both understanding of baryon physics, especially AGN feedback, and the computational performance, have advanced, simulations involving reliable baryon physics have been conducted. We made theoretical predictions related to the non-sphericity of galaxy clusters using the Horizon-AGN simulation, which is one of the latest simulations, and also tried to understand the structure formation history in the ΛCDM universe. We validate the consistency of the ΛCDM model complementarily to previous probes by comparing the theoretical predictions with our new observation in addition to previous observations. The results obtained in each chapter are summarized below.

Chapter 3

- We measured ellipticities and orientations of 120 galaxy clusters in the Horizon-AGN simulation using mock observational images in visible light, X-ray, and radio wavelength.
- Mean ellipticity values obtained from dark matter (DM), member galaxy distribution, and X-ray are 0.35, 0.5, and 0.2, respectively, which are marginally consistent with the currently available observations.
- Orientations of galaxy clusters measured in the mock images are aligned well with those of CGs in the ΛCDM universe, and the theoretical predictions were also marginally consistent with currently available observations.

Chapter 4

- We obtained a large sample of galaxy clusters by combining three survey data observed by Hubble Space Telescope. We measured ellipticities and orientations for 45 DM haloes using the strong lensing, and those of CGs from high resolution images to provide a new observational constraint.

- From our new observation, we found that orientations of DM haloes and those of their CGs are aligned well with each other, $\langle|\theta_{\rm SL}-\theta^{20}_{BCG}|\rangle = 22.2\pm3.9$ deg, and that galaxy clusters are on average more aspherical than central galaxies, $\langle e_{\rm DM}-e^{20}_{\rm BCG}\rangle = 0.11\pm0.03$.
- We obtained theoretical predictions of the ΛCDM model from the Horizon-AGN simulation that ellipticity values of the DM haloes and central galaxies are almost equal on average from galaxy to cluster scales, but the slightly larger masses are, the larger the differences of ellipticities become such that DM haloes become aspherical.

Chapter 5

- We investigated time evolution of orientations and masses of DM haloes and their CGs for 40 galaxy clusters in the Horizon-AGN simulation over the cosmic time from $t = 1.5$ to 13.5 Gyr.
- Even in the early stage of the universe, $t = 1.5$ Gyr, orientations of DM haloes and those of their CGs are weakly correlated, and the alignments at each epoch become tighter with cosmic time.
- Orientations of both DM haloes and CGs have significantly changed through evolution rather than being constant, and the changes of orientations are mainly caused by mass accretion episodes.
- We examined the time evolution of orientations of DM haloes and CGs relative to the directions of surrounding matter distributions around galaxy clusters defined by tidal fields. The major axes of both DM haloes and CGs tend to slightly be aligned with the directions of surrounding matter distributions.

Throughout this thesis, we carried out mock observations of simulated galaxy clusters to understand the structure formation history in the ΛCDM universe, and validated the consistency of the ΛCDM model through comparisons of these results with observations in the real Universe. In the ΛCDM universe, DM haloes grow up following the bottom-up structure formation scenario, in which small structures of DM collapse first and larger structures are formed by their mergers. Galaxy clusters, the largest self-gravitational bounding systems in the universe, are still growing objects by repeated mergers under this scenario.

We confirmed that DM haloes of cluster scales are more elongated than those of galaxy scales in the ΛCDM universe (Figure 4.9). This result can be interpreted that galaxy clusters are growing through anisotropic mass accretion episodes whereas DM haloes at galaxy scales formed relatively earlier epochs and settled in virialization. This scale dependence is observed; i.e., mean ellipticity values of DM haloes at galaxy scales are on average $\langle e\rangle \sim 0.3$ (e.g. Hoekstra *et al.*, 2004) while those at cluster scales are $\langle e\rangle \sim 0.5$ (e.g. Oguri *et al.*, 2010, 2012, and our work). The quantitative consistency of these observations (Figure 4.9) indicates the validation of the ΛCDM model.

We found that galaxy clusters in RELICS sample, which likely contains disturbed clusters, are more aspherical than those in CLASH sample, which preferentially comprises relaxed clusters. In addition, double peak clusters, which might be during or before

merger, are more aspherical than those of single peak indicating that shapes of clusters are elongated by such merger events. Since we did not investigate the effects of such sample selection in this thesis, it remains future tasks to investigate ellipticity variations of galaxy clusters before and after mergers in the ΛCDM universe and compare with these observations.

Orientations of galaxy clusters and CGs are well aligned in the ΛCDM universe (Figure 3.11). The alignments might be because both are affected by anisotropic matter distributions such as filaments imprinted in the initial conditions of primordial density fluctuations. We confirmed the effect of the initial conditions by examining preferred directions of surrounding matter distributions defined by the tidal field. According to the bottom-up scenario, galaxy clusters and CGs grow up through mass accretion episodes, and the mass accretions change their orientations (Figure 5.7), but the orientations remain aligned on average at each time (Figure 5.3). The mass accretions take place along directions of filaments which were already imprinted in the early universe (Figures 5.8 and 5.9). The bottom-up structure formation scenario in the ΛCDM universe explains observational facts that orientations of galaxy clusters and those of their CGs are well aligned (Figure 3.12), and that the alignments already existed at 10 billion years before (West *et al.*, 2017).

The alignment becomes weaker as the mass decreases (Figure 4.12). Since DM haloes of small mass scales collapse quickly and are approaching the physical equilibrium state in the ΛCDM universe, they have forgotten the memory of the initial conditions. The weaker alignments at small mass scales also support that galaxy clusters and CGs are aligned because they still retain the memory of the initial conditions, rather than because of physical processes such as tidal torques. Observationally, the alignment is also weak at galaxy scales (e.g. Okumura & Jing, 2009), and thus the structure formation scenario predicted by the ΛCDM model is consistent with the observations.

Orientations of X-ray surface brightness are well aligned with those of CGs in the ΛCDM universe (Figure 3.11). Since the cluster sample in the Horizon-AGN simulation is a volume limited sample containing both relaxed and disturbed clusters, there is no bias for gas states. However, we found that the distribution of the alignment angles in the simulation is consistent with that from the CLASH observation composed of relaxed clusters (Figure 3.12), suggesting that the alignment is independent of gas states. This result is qualitatively consistent with observational finding by Hashimoto *et al.* (2008) and also supports the ΛCDM model.

Future large surveys such as HSC and LSST will enable us to validate the ΛCDM model more precisely by comparing our theoretical predictions in this thesis with the observations. In particular, the theoretical predictions of the ΛCDM model about the evolution scenario of the alignments between orientations of galaxy clusters and CGs will be testable by observing the alignments at high redshifts beyond $z = 1$. Furthermore, non-sphericities of both DM haloes and their BCGs for more galaxy cluster samples with wider mass range will be obtained from high resolution images of HST and future space telescopes such as JWST. Especially, it plays an important role in directly comparing

with theoretical predictions of the ΛCDM model to measure non-sphericities of relatively low mass galaxy clusters, $\sim 10^{14} M_{\odot}$, whose masses are comparable to typical clusters in the Horizon-AGN simulation. In addition to the observational updates, cosmological hydrodynamical simulations would be updated such that they have larger box sizes. The future simulations would generate massive galaxy clusters with mass of $\sim 10^{15} M_{\odot}$ corresponding to typical observed clusters. Therefore, our finding that the observed mean value of ellipticity differences between galaxy clusters and BCGs is inconsistent with those of the simulated galaxy clusters would be directly testable by updating both observations and simulations.

Once we accept the validity of the ΛCDM model, we would be able to constrain DM model and AGN feedback, and explore baryon distributions in the Universe from the non-sphericity of galaxy clusters. Since the non-sphericity of galaxy clusters is sensitive to the cross section of the self-interacting DM (e.g. Yoshida *et al.*, 2000b) and the strength of the AGN feedback (e.g. Suto *et al.*, 2017), these parameters can be constrained by comparing results of simulations with observations. The tendency of galaxy clusters to be aligned with filaments can also be used to search for baryons in filaments. About 30% of baryons in the Universe are missing (Fukugita *et al.*, 1998) compared with the ΛCDM model and are believed to exist in filaments (de Graaff *et al.*, 2019; Tanimura *et al.*, 2019). Future large surveys will explore these baryons within the filaments to validate the ΛCDM model, and thus to identify locations of filaments should be important. The orientations of galaxy clusters can be used as indicators of the filament locations. In any case, our study in this thesis will serve as a bridge between previous and future studies in terms that we focus on the non-sphericity of galaxy clusters and attempt to extract cosmological and astrophysical informations through comparison of observations and theoretical predictions.

Appendix A

The Horizon simulation: cosmological hydrodynamical simulation

We examine the correlations of non-sphericities of projected surface densities among different components of simulated galaxy clusters and the evolution of the non-sphericities and orientations of DM haloes and their CGs in this thesis. In particular, we are interested in the alignment between the position angles of DM haloes and those of their CGs. Clearly this requires a cosmological hydrodynamical simulation implemented with detailed baryon physics and also with high spatial and mass resolutions to identify CGs in the cluster centres. We thus focus on the Horizon simulation, one of the state-of-the-art cosmological hydrodynamical simulations. The detail of this simulation is already described in Dubois *et al.* (2014). Thus we summarize only its major features relevant to our current studies. The Horizon simulation adopts the standard ΛCDM cosmological model. The cosmological parameters are based on the seven-year Wilkinson Microwave Anisotropy Probe (Komatsu *et al.*, 2011); $\Omega_{\rm m,0} = 0.272$ (total matter density at present day), $\Omega_{\Lambda,0} = 0.728$ (dark energy density at present day), $\Omega_{\rm b,0} = 0.045$ (baryon density at present day), $\sigma_8 = 0.81$ (amplitude of the power spectrum of density fluctuations that are averaged on spheres of $8h^{-1}$ Mpc radius at present day), $\rm H_0 = 70.4$ km/s/Mpc (Hubble constant), and $n_s = 0.967$ (the power-law index of the primordial power spectrum), and thus we use these values throughout this thesis to suit the Horizon simulation.

A.1 Detail of the Horizon simulation: box size, resolution, resolved components, and how to solve them

The simulation is performed in a periodic cube of $(100h^{-1}\,{\rm Mpc})^3$, and the initial condition is generated with MPGRAFIC software (Prunet *et al.*, 2008). The simulation follows the evolution of three different components, dark matter, gas, and star. Dark matter is represented by $N = 1024^3$ equal-mass particles in the entire box, corresponding to the mass

resolution of $8.27 \times 10^7\,\mathrm{M}_\odot$. Baryon gas is assigned over the meshes in the simulation box, and its evolution is solved with the adaptive mesh refinement code RAMSES (Teyssier, 2002). Star is represented by collisionless particles, whose formation is modeled on the basis of an empirical Schmidt law. Since those star particles are created according to a random Poisson process, their masses are not the same, but typically around $2 \times 10^6 M_\odot$.

The evolution of collisionless particles (dark matter and star) are followed by the particle-mesh solver with a cloud-in-cell interpolation. Therefore, the spatial resolution depends on the size of the local cell where those particles are located. The initial size of the gas cell is 136 kpc, and then refined up to 1.06 kpc ($= 136/2^7$kpc after seven times refinement), which corresponds to the highest spatial resolution achieved in the simulation.

In addition to radiative cooling and hydrodynamical evolution of gas component, feedback from stars is implemented assuming the Salpeter initial mass function (Salpeter, 1955) with lower and upper mass limits of $0.1M_\odot$ and $100M_\odot$, respectively. The mechanical energy from Type II supernova explosions and stellar winds is computed according to the STARBURST99 (Leitherer *et al.*, 1999, 2010) with the frequency of Type Ia supernova explosions computed using Greggio & Renzini (1983).

A.2 Three different types of the Horizon simulation: Horizon-DM, Horizon-AGN, and Horizon-noAGN

The Horizon simulations consist of three simulations, Horizon-DM, Horizon-AGN, and Horizon-noAGN. In this thesis, we use the Horizon-AGN simulation in order to explore shapes of CGs that are not created in Horizon-DM, and do not use Horizon-noAGN which adopts exactly the same initial condition and physical process as the Horizon-AGN except for feedback of active galactic nuclei (AGN) due to inconsistency with observations. Suto *et al.* (2017) compared axis ratios of cluster-sized haloes in the Horizon-AGN with those in Horizon-noAGN to find that baryon processes affect shapes of DM haloes even in outer regions, ~ 1 Mpc, of galaxy clusters. They also claim that AGN feedback plays a curial role to match simulations with various observations such as mass density profiles, temperature profiles, and ellipticities of galaxy clusters. Furthermore, while the Horizon-AGN simulation reproduces various observations, the Horizon-noAGN does not. The comparisons of the Horizon simulations with observations will be discussed later in detail in Subsection A.4. It is not our main subject to what extent AGN feedback affects the observable values, and this is why we focus on the Horizon-AGN simulation in this thesis.

A.3 The AGN feedbacks implemented in the Horizon-AGN simulation

Active galactic nuclei (AGN) are central regions of galaxies which have comparable luminosities to those of galaxies while the size of them are compact and much smaller than galaxies. The AGN are considered as super massive central black holes emitting by the

accretions of matter on to them and the radiation is powerful such that they substantially affect the galaxy formation through heating the surrounding gases. Therefore, modeling and implementing their effects are crucial for cosmological hydrodynamical simulations to reproduce observations as discussed in Section A.4.

In the Horizon-AGN, black holes are created when the local gas mass density becomes larger than $\rho > \rho_0$ with an initial mass of $10^5 M_\odot$ The black holes are prohibited to form within 50 kpc from nearby one such that only one black holes exist in a galaxy. The accretion rate on to black holes is computed by the Bondi-Hoyle-Lyttleton rate,

$$\dot{M}_{\rm BH} = \frac{4\pi\alpha G^2 M_{\rm BH}^2 \overline{\rho}}{(\overline{c}_{\rm s}^2 + \overline{u}^2)^{3/2}}, \tag{A.1}$$

where $M_{\rm BH}$ denotes the black hole mass, $\overline{\rho}$, $c_{\rm s}$, and $\overline{u}$ are the average gas density, the average sound speed, and the average gas velocity relative to black hole, respectively and α is a dimensionless boost factor defined by

$$\alpha = \begin{cases} \left(\dfrac{\rho}{\rho_0}\right)^2 & (\rho > \rho_0) \\ 1 & (otherwise) \end{cases} \tag{A.2}$$

(Booth & Schaye, 2009). The factor is introduced in order to correct sub-grid physics because regions of interstellar medium with colder and higher density cannot be captured. The upper limit of the accretion rate is set to the Eddington accretion rate defied as

$$\dot{M}_{\rm Edd} = \frac{4\pi\alpha G M_{\rm BH} m_{\rm p}}{\epsilon_{\rm r}\sigma_{\rm T} c}, \tag{A.3}$$

where $m_{\rm p}$, c, $\sigma_{\rm T}$, and $\epsilon_{\rm r}$ denote the mass of proton, speed of light, the Tompson cross-section, and the radiative efficiency, respectively. The efficiency is assumed, $\epsilon_{\rm r} = 0.1$, following Shakura & Sunyaev (1973).

There are two different AGN feedback modes in the Horizon-AGN simulation; one is *radio* mode and the other is *quasar* mode depending on the Eddington ratio

$$\chi \equiv \dot{M}_{\rm BH}/\dot{M}_{\rm Edd} \tag{A.4}$$

Recent observations (e.g. Cheung *et al.*, 2016) support that both modes exist, and thus it is reasonable to implement both the feedback mode in the simulation. At low accretion rate $\chi < 0.01$, feedback from black holes behaves as radio mode which injects the energy into a bipolar outflow with a jet velocity of $10^4\,{\rm km\ s^{-1}}$. The outflow jet is modeled as a cylinder following Omma *et al.* (2004). Dubois *et al.* (2010) describes more details. The energy deposition rate of the radio mode is computed by $\dot{E}_{\rm AGN} = \epsilon_{\rm f}\epsilon_{\rm r}\dot{M}_{\rm BH}c^2$ where $\epsilon_{\rm f}$ is the free parameter and set to unity for the radio mode. The quasar mode is adopted at high accretion rate $\chi > 0.01$, which deposits the thermal energy into the gas isotropically at an energy deposition rate $\dot{E}_{\rm AGN}$. The free parameter $\epsilon_{\rm f}$ is chosen so as to reproduce observations of the scaling relations between black hole masses and galaxy properties (bulge masses and velocity dispersions of stars) and the black hole density in our local Universe. The more details are given in Dubois *et al.* (2012).

A.4 The consistency of the Horizon-AGN simulation with observations

The dataset from the Horizon-AGN simulation has been examined in detail by various authors from different aspects. The free parameter, $\epsilon_{\rm f}$, in the simulation is set in order to reproduce the scaling relations between black hole masses and galaxy properties (bulge masses and velocity dispersions of stars) and the black hole density in our local Universe. Comparisons of the simulation with other observations are important to check the consistency of the simulation. Many studies using the Horizon simulations show that the AGN feedback is essential to reproduce various observed features such as intrinsic alignment of galaxies (Chisari *et al.*, 2015, 2016), morphological diversity of galaxies, galaxy-halo mass relation, size-mass relation of galaxies (Dubois *et al.*, 2016), AGN luminosity function, black hole mass density (Volonteri *et al.*, 2016), density profile of massive galaxies (Peirani *et al.*, 2017, 2019), high-mass end of the galaxy stellar mass function (Beckmann *et al.*, 2017), gas fraction as a function of halo mass Chisari *et al.* (2018), the correlation of number counts between massive black holes and galaxies Habouzit *et al.* (2019), the relation between spin parameters and ellipticities of galaxies Choi *et al.* (2018), the star formation processes and morphologies of high redshift galaxies Martin *et al.* (2018), luminosity functions of galaxies, stellar mass functions, the star formation main sequence, rest-frame UV-optical-NIR colours, the cosmic star formation history in the redshift range $1 < z < 6$ (Kaviraj *et al.*, 2017), ellipticities of X-ray galaxy clusters (Suto *et al.*, 2017), and tight relation between black hole masses in the brightest group/cluster galaxies and their host group/cluster masses (Bogdan *et al.*, 2017). These properties are not accounted for in the Horizon-noAGN, and that is why we only used the results of the Horizon-AGN simulation, not the Horizon-noAGN simulation, in this thesis.

Appendix B

Strong lensing mass models

Strong lens mass models that are used in the analysis of this thesis are summarized in Table B.1. All the mass models are constructed using the software GLAFIC (Oguri, 2010). The mass models of HFF clusters have already been presented in Kawamata *et al.* (2016) and Kawamata *et al.* (2018), whereas those of CLASH and RELICS clusters have not been published elsewhere.

We follow Kawamata *et al.* (2016) for mass modeling procedure of CLASH and RELICS clusters. We assume simply parametrize mass models that consist of halo components modeled by an elliptical NFW profile and cluster galaxies modeled by an elliptical pseudo-Jaffe profile. To reduce the number of parameters, we assume scaling relations between galaxy luminosities and model parameters (velocity dispersions and truncation radii) of the pseudo-Jaffe profile. Ellipticities and position angles of cluster member galaxies are fixed to measured values of their light profiles, whereas ellipticities and position angles of halo components are treated as free parameters. We may also add external perturbations to the lens potential. We start with a simple mass model, and keep adding more halo components or external perturbations until we obtain reasonably good fit. Interested readers are referred to Kawamata *et al.* (2016) for more details.

We optimize model parameters so that the model can reproduce positions of multiple images. We rely on previous work as listed in Table B.1 for identifications of multiple images and spectroscopic redshift information for some of them. Positional uncertainties of multiple images are set so as to achieve reasonably good fit i.e., reduced χ^2 being of order one. χ^2 is defined by differences of observed and model-predicted image positions evaluated in the source plane (see Appendix 2 of Oguri, 2010, for more details). The minimum χ^2 for our best-fitting models are listed in Table B.1. Errors of model parameters are estimated using the Markov chain Monte Carlo method.

Table B.1. Summary of strong lens mass modeling using GLAFIC (Oguri, 2010). $N_{\rm sys}$ denotes the number of multiple image systems, $N_{\rm sys,spec}$ is the number of multiple image systems with spectroscopic redshifts, and $N_{\rm img}$ is the total number of multiple images used for mass modeling. The assumed positional error of multiple images in the image plane is shown by $\sigma_{\rm img}$. The minimum χ^2 and degree of freedom are indicated by $\chi^2_{\rm min}$ and dof, respectively.

Survey	Cluster name	$N_{\rm sys}$	$N_{\rm sys,spec}$	$N_{\rm img}$	$\sigma_{\rm img}$ [$''$]	$\chi^2_{\rm min}$/dof	Refs.
HFF	Abell 2744	45	24	132	0.4	130.2/134	1
HFF	MACSJ0416.1−2403	75	34	202	0.4	240.0/196	1
HFF	MACSJ1149.5+2223	36	16	108	0.4	100.1/103	2
HFF	Abell S1063	53	19	141	0.4	136.2/138	1
CLASH	Abell 209	3	0	7	0.8	2.8/1	3,4
CLASH	Abell 383	8	6	23	0.4	22.5/18	3,4
CLASH	MACSJ0329.7−0211	9	8	23	0.4	16.3/12	5,4
CLASH	MACSJ0429.6−0253	3	2	11	0.4	7.2/9	5,4
CLASH	MACSJ0744.9+3927	10	0	25	0.4	6.7/8	3,4
CLASH	Abell 611	3	2	14	0.4	11.6/12	3,4
CLASH	MACSJ1115.9+0129	3	1	9	0.6	4.9/3	5,4
CLASH	MACSJ1206.2-0847	27	27	82	0.4	79.9/83	6,4
CLASH	CLJ1226.9+3332	4	0	15	0.6	10.8/9	3,4
CLASH	MACSJ1311.0−0310	3	1	8	0.6	7.2/4	5,4
CLASH	RXJ1347.5−1145	8	4	20	0.4	1.9/4	7,5,4
CLASH	MACSJ1423.8+2404	3	2	12	0.8	6.9/9	3,4
CLASH	MACSJ1720.3+3536	7	0	22	0.6	16.1/14	3,4
CLASH	Abell 2261	11	0	28	0.4	13.4/13	3,4
CLASH	MACSJ1931.8−2635	7	7	19	0.4	17.9/12	5,4
CLASH	RXJ2129.7+0005	7	7	22	0.4	17.1/21	5,4
CLASH	MS2137−2353	3	3	10	0.6	5.7/6	3,4
CLASH	MACSJ0647.8+7015	11	0	31	0.4	24.3/20	3,4
CLASH	MACSJ2129.4−0741	11	11	38	0.6	45.6/37	5,4
RELICS	Abell 2163	4	0	15	0.4	6.6/12	8,4
RELICS	Abell 2537	8	1	29	0.6	16.1/23	8,4
RELICS	Abell 3192	5	2	16	0.8	7.4/6	9,4
RELICS	Abell 697	3	0	9	0.4	6.7/6	10,4
RELICS	Abell S295	6	4	18	0.4	5.4/13	10,4
RELICS	ACT-CL J0102−49151	10	0	28	0.6	17.6/15	8,4
RELICS	CL J0152.7−1357	8	1	24	0.4	8.1/16	11,4
RELICS	MACSJ0159.8−0849	4	0	10	0.6	5.6/4	10,4
RELICS	MACSJ0257.1−2325	4	0	12	0.4	10.1/7	12,4
RELICS	MACSJ0308.9+2645	3	0	7	0.4	0.7/1	13,4
RELICS	MACSJ0417.5−1154	20	7	54	0.4	29.4/40	14,4
RELICS	MACSJ0553.4−3342	10	2	30	0.8	29.9/25	15,4
RELICS	PLCK G171.9−40.7	5	0	16	0.4	11.7/7	13,4
RELICS	PLCK G308.3−20.2	11	0	31	0.6	17.8/18	16,4
RELICS	RXC J0142.9+4438	4	0	14	0.4	8.8/9	8,4
RELICS	RXC J2211.7−0350	3	1	11	0.4	2.7/3	8,4
RELICS	SPT-CL J0615−5746	6	5	22	0.4	5.2/17	17,4

References – (1) Kawamata *et al.* (2018); (2) Kawamata *et al.* (2016); (3) Zitrin *et al.* (2015); (4) this thesis; (5) Caminha *et al.* (2019); (6) Caminha *et al.* (2017); (7) Ueda *et al.* (2018); (8) Cerny *et al.* (2018); (9) Hsu *et al.* (2013); (10) Cibirka *et al.* (2018); (11) Acebron *et al.* (2019); (12) Zitrin *et al.* (2011); (13) Acebron *et al.* (2018); (14) Mahler *et al.* (2019); (15) Ebeling *et al.* (2017); (16) Zitrin *et al.* (2017); (17) Paterno-Mahler *et al.* (2018).

Acknowledgement

First of all, I would like to express my great gratitude to my supervisor, Yasushi Suto. He was like a lighthouse to help me figure out where to go. He led me very kindly, persistently, and warmly. I do feel lucky to be able to work with him who has the insight to find out the essence of things accurately and the ability to immediately express it clearly in words. I learned a lot from his tough attitude of being kind to people but not compromising on facts. In addition, I developed my ability to think logically and to tell a story from a big picture, which is important not only in research but also in all situations. I cannot fully express my appreciation for him in any words.

I would also like to express my great gratitude to another instructor guiding me, Masamune Oguri. He listened kindly and persistently to my vague claims in discussions and instantly understood them to a deep level that even I didn't realize. His words contained a lot of information, in which I always felt the depth of humanity, the sincerity to science, and the consideration for me. In addition, my papers has been brushed up thanks to his careful reviews and appropriate comments for my poor drafts which an ordinary person would have given up. Without him, it would have been impossible to complete published papers and this thesis. I would like to thank him again for providing the data of non-sphericity measured using strong lensing analysed in Chapter 4. Without his cooperation, I could not do such analyses.

I would like to express my deep gratitude to Takahiro Nishimichi for giving me advices, especially on computers. Since the calculations in this thesis were basically performed using his computer, this study could not be completed without his cooperation. He taught me a lot about how to use the computer and the algorithm to calculate the tidal field, and also motivated me by teaching kindly. I really appreciate a number of helpful and constructive comments from my collaborators Shin Sasaki and Tetsu Kitayama at the weekly Monday discussions. From the discussions, I learned the importance of interacting with various people and receive comments from different perspectives.

I would like to express my deepest gratitude to Sébastien Peirani for providing the data of the Horizon-AGN simulation. Without his cooperation, I could not conduct the analyses in this thesis. In addition, when I stayed at the Observatoire de la Côte d'Azur as part of the research program, he took care me of everything. Thanks to his warm hospitality, I did my best to research and write a paper. I am also very grateful to his wife and son for welcoming me warmly when I visited his house. I would like to express my deepest gratitude to the people on the Horizon simulation team for providing the data, and in particular Yohan Dubois and Christophe Pichon for encouraging me from France

and contributing to the promotion of my paper writing. I would like to thank Yohan for giving me useful advices on my research and for helping to make the paper better. I would like to thank Christophe for providing very useful advices on the aesthetics of the figures. I am very grateful to people at the Observatoire de la Côte d'Azur for welcoming me and engaging in constructive discussions.

I would like to express my great gratitude to Kazumi Kashiyama for teaching me the basic approach of capturing the essence of things, reconstructing it as a simple picture, and communicating it to other people. I was always amazed at his extraordinary insight, and learned a methodology for understanding complex things simply. In addition, I was always very helped by the encouraging, constructive and highly motivating advices. I am also thankful for the casual conversation while drinking coffee and coaching me on basketball. I would like to thank Naoki Yoshida for teaching on the importance of studying not only within the narrow field but also within the challenges of physics as a whole. I am very thankful for taking me to Vietnamese food once in a while and having a pleasant chat. I would also like to thank other faculty members of UTAP and RESEU, especially Jun'ichi Yokoyama, Toshikazu Shigeyama, Kipp Cannon, Takuma Suda, Takashi Hosokawa, and Kohei Kamada, for constructive comments through seminars and private discussions. I am also grateful to Professor Hideo Higuchi, who was my assistant supervisor through the ALPS course. He helped me to interact with students from various fields, including biology, chemistry, and artificial intelligence. He listened kindly and sincerely to my reports and gave me fruitful comments with a friendly and gentle smile. I learned how difficult but interesting and important it is for people in other fields to understand my research.

I would like to express my deepest gratitude to two of my senior colleagues, Toshiya Kashiwagi and Daichi Suto. Kashiwagi-san gave me a gentle education through seminars and discussions when I was a first-year of my Master course. He taught me the joy of research, and thus without his help, I could not even start my research life. Daichi-san kindly transfer the knowledges regarding the research contents in this thesis, and thus I was able to conduct the analysis in this thesis thanks to his cooperation. Both of them have taken care of me after graduation and have encouraged me by taking me out to dinner. I would like to thank Summyon Chon and Gen Chiaki for their support in daily research life. Chon-san gave me great mental support by staying in the lab until midnight, sometimes eating ramen, and sometimes relaxing in *sento* together. I was always encouraged by his extraordinary toughness, persistence, and perseverance. Chiaki-san always accepted my concerns and chatted with me in coffee shops about various fields as well as science which helped me broaden my knowledge and perspectives. I cannot thank Shoya Kamiaka too enough for accepting me whenever I speak to him, for teaching me about detailed paperwork procedures, and for taking care of me after graduation. I would also like to express my deepest gratitude to my two colleagues, Riouhei Nakatani and Ken Osato. I really thank Nakatani-kun a lot for sharing joys of scientific discussions and relieving stress by playing sports. In addition, I really respect him and was always stimulated by his mentality, toughness, and persistence. I also thank SatoKen a lot for discussing

cosmology, giving me many useful comments on my research, and helping me with codes and plotting tools. I am very grateful to Masataka Aizawa for discussing physics in a different field. I was always encouraged by his passion, ideas, toughness, and talent to make everyone around him happy. He also encouraged and helped me many times as a fellow writer of PhD thesis. Without him, I might give up writing my thesis. I would also like to send my thanks to my two juniors, Akinari Hamabata and Yuta Nakagawa. I really enjoyed studying and discussing cosmology and galaxy clusters with Bata-kun. I was always excited by his rough but interesting ideas, and I was always stimulated by his powerfulness. Thanks to him, I was able to realize the fun of research. I really appreciate Gawa-kun's broad-mind which always healed my desperate heart by research.

I would like to express my great thanks to other members and secretaries of UTAP and RESCEU, Shigeki Inoue, Taira Oogi, Yi-Peng Wu, Shingo Hirano, Akira Oka, Kento Masuda, Natsuki Hayatsu, Ayako Ishii, Yuya Sakurai, Akira Harada, Naritaka Oshita, Yuya Deno, Hiroaki Tahara, Soichiro Morisaki, Takahiro Kato, Kojiro Kawana, Leo Tsukada, Conar Omand, Shijie Wang, Toshinori Hayashi, Tomohisa Ueno, Kana Moriwaki, Daichi Tsuna, Yuuki Takei, Kazuko Filson, Mayuko Niwata, Mieko Minamisawa, Sayuri Nagano, Chiyo Ueda, and other members. I am also really grateful to my high school friends, my baseball team friends, and my undergraduate friends for supporting me in graduate school.

Last but not least, I would like to express my special thanks to my parents who raised me and allowed me to go to university; to my grandparents who loved me sweetly and warmly; and to my brother Tomohiro whom I have spent most of my life with.

I greatly appreciate the funding by the Advanced Leading Graduate Course for Photon Science (ALPS) at the University of Tokyo and Japan Society for the Promotion of Science (JSPS) KAKENHI Grant Numbers JP17J05056.

As mentioned above, I am grateful that I was blessed with people around me and that I was able to study in the good environment. In retrospect, I was only just given in my graduate course, and thus I will express my sincerity and gratitude by returning to the society what I received.

Bibliography

Abell, G. O. (1958). *The Distribution of Rich Clusters of Galaxies.* ApJS**3**, 211.

Acebron, A., Alon, M., Zitrin, A., Mahler, G., Coe, D., Sharon, K., Cibirka, N., Bradač, M., Trenti, M., Umetsu, K., Andrade-Santos, F., Avila, R. J., Bradley, L., Carrasco, D., Cerny, C., Czakon, N. G., Dawson, W. A., Frye, B., Hoag, A. T., Huang, K.-H., Johnson, T. L., Jones, C., Kikuchihara, S., Lam, D., Livermore, R. C., Lovisari, L., Mainali, R., Oesch, P. A., Ogaz, S., Ouchi, M., Past, M., Paterno-Mahler, R., Peterson, A., Ryan, R. E., Salmon, B., Sendra-Server, I., Stark, D. P., Strait, V., Toft, S. & Vulcani, B. (2019). *RELICS: High-resolution Constraints on the Inner Mass Distribution of the z = 0.83 Merging Cluster RXJ0152.7-1357 from Strong Lensing.* ApJ**874**(2), 132.

Acebron, A., Cibirka, N., Zitrin, A., Coe, D., Agulli, I., Sharon, K., Bradač, M., Frye, B., Livermore, R. C., Mahler, G., Salmon, B., Umetsu, K., Bradley, L., Andrade-Santos, F., Avila, R., Carrasco, D., Cerny, C., Czakon, N. G., Dawson, W. A., Hoag, A. T., Huang, K.-H., Johnson, T. L., Jones, C., Kikuchihara, S., Lam, D., Lovisari, L., Mainali, R., Oesch, P. A., Ogaz, S., Ouchi, M., Past, M., Paterno-Mahler, R., Peterson, A., Ryan, R. E., Sendra-Server, I., Stark, D. P., Strait, V., Toft, S., Trenti, M. & Vulcani, B. (2018). *RELICS: Strong-lensing Analysis of the Massive Clusters MACS J0308.9+2645 and PLCK G171.9-40.7.* ApJ**858**(1), 42.

Aihara, H., Armstrong, R., Bickerton, S., Bosch, J., Coupon, J., Furusawa, H., Hayashi, Y., Ikeda, H., Kamata, Y., Karoji, H., Kawanomoto, S., Koike, M., Komiyama, Y., Lang, D., Lupton, R. H., Mineo, S., Miyatake, H., Miyazaki, S., Morokuma, T., Obuchi, Y., Oishi, Y., Okura, Y., Price, P. A., Takata, T., Tanaka, M. M., Tanaka, M., Tanaka, Y., Uchida, T., Uraguchi, F., Utsumi, Y., Wang, S.-Y., Yamada, Y., Yamanoi, H., Yasuda, N., Arimoto, N., Chiba, M., Finet, F., Fujimori, H., Fujimoto, S., Furusawa, J., Goto, T., Goulding, A., Gunn, J. E., Harikane, Y., Hattori, T., Hayashi, M., Hełminiak, K. G., Higuchi, R., Hikage, C., Ho, P. T. P., Hsieh, B.-C., Huang, K., Huang, S., Imanishi, M., Iwata, I., Jaelani, A. T., Jian, H.-Y., Kashikawa, N., Katayama, N., Kojima, T., Konno, A., Koshida, S., Kusakabe, H., Leauthaud, A., Lee, C.-H., Lin, L., Lin, Y.-T., Mandelbaum, R., Matsuoka, Y., Medezinski, E., Miyama, S., Momose, R., More, A., More, S., Mukae, S., Murata, R., Murayama, H., Nagao, T., Nakata, F., Niida, M., Niikura, H., Nishizawa, A. J., Oguri, M., Okabe, N., Ono, Y., Onodera, M.,

Onoue, M., Ouchi, M., Pyo, T.-S., Shibuya, T., Shimasaku, K., Simet, M., Speagle, J., Spergel, D. N., Strauss, M. A., Sugahara, Y., Sugiyama, N., Suto, Y., Suzuki, N., Tait, P. J., Takada, M., Terai, T., Toba, Y., Turner, E. L., Uchiyama, H., Umetsu, K., Urata, Y., Usuda, T., Yeh, S. & Yuma, S. (2018). *First data release of the Hyper Suprime-Cam Subaru Strategic Program.* PASJ**70**, S8.

Allen, S. W., Fabian, A. C., Edge, A. C., Bohringer, H. & White, D. A. (1995). *Cooling flows, central galaxy-cluster alignments, X-ray absorption and dust.* MNRAS**275**(3), 741–754.

Allgood, B., Flores, R. A., Primack, J. R., Kravtsov, A. V., Wechsler, R. H., Faltenbacher, A. & Bullock, J. S. (2006). *The shape of dark matter haloes: dependence on mass, redshift, radius and formation.* MNRAS**367**, 1781–1796.

AMI Consortium, Rodríguez-Gonzálvez, C., Shimwell, T. W., Davies, M. L., Feroz, F., Franzen, T. M. O., Grainge, K. J. B., Hobson, M. P., Hurley-Walker, N., Lasenby, A. N., Olamaie, M., Pooley, G., Saunders, R. D. E., Scaife, A. M. M., Schammel, M. P., Scott, P. F., Titterington, D. J. & Waldram, E. M. (2012). *Detailed Sunyaev-Zel'dovich study with AMI of 19 LoCuSS galaxy clusters: masses and temperatures out to the virial radius.* MNRAS**425**(1), 162–203.

Argyres, P. C., Groth, E. J., Peebles, P. J. E. & Struble, M. F. (1986). *Detection of large-scale alignment of Lick counts around Abell clusters.* AJ**91**, 471–477.

Arnaud, M., Pointecouteau, E. & Pratt, G. W. (2007). *Calibration of the galaxy cluster M{500}-Y{X} relation with XMM-Newton.* A&A**474**(3), L37–L40.

Aubert, D., Pichon, C. & Colombi, S. (2004). *The origin and implications of dark matter anisotropic cosmic infall on ˜L∗ haloes.* MNRAS**352**, 376–398.

Azzaro, M., Patiri, S. G., Prada, F. & Zentner, A. R. (2007). *Angular distribution of satellite galaxies from the Sloan Digital Sky Survey Data Release 4.* MNRAS**376**, L43–L47.

Bailin, J. & Steinmetz, M. (2005). *Internal and External Alignment of the Shapes and Angular Momenta of ΛCDM Halos.* ApJ**627**(2), 647–665.

Bartelmann, M. (1996). *Arcs from a universal dark-matter halo profile.* A&A**313**, 697–702.

Bate, J., Chisari, N. E., Codis, S., Martin, G., Dubois, Y., Devriendt, J., Pichon, C. & Slyz, A. (2019). *When galaxies align: intrinsic alignments of the progenitors of elliptical galaxies in the Horizon-AGN simulation.* arXiv e-prints , arXiv:1911.04213.

Beckmann, R. S., Devriendt, J., Slyz, A., Peirani, S., Richardson, M. L. A., Dubois, Y., Pichon, C., Chisari, N. E., Kaviraj, S., Laigle, C. & Volonteri, M. (2017). *Cosmic evolution of stellar quenching by AGN feedback: clues from the Horizon-AGN simulation.* MNRAS**472**, 949–965.

Bernstein, G. M. & Jarvis, M. (2002). *Shapes and Shears, Stars and Smears: Optimal Measurements for Weak Lensing.* AJ**123**, 583–618.

Binggeli, B. (1980). *On the intrinsic shape of elliptical galaxies.* A&A**82**(3), 289–294.

Binggeli, B. (1982). *The shape and orientation of clusters of galaxies.* A&A**107**, 338–349.

Bogdan, A., Lovisari, L., Volonteri, M. & Dubois, Y. (2017). *Correlation Between the Total Gravitating Mass of Groups and Clusters and the Supermassive Black Hole Mass of Brightest Galaxies.* ArXiv e-prints .

Booth, C. M. & Schaye, J. (2009). *Cosmological simulations of the growth of supermassive black holes and feedback from active galactic nuclei: method and tests.* MNRAS**398**(1), 53–74.

Brainerd, T. G. (2005). *Anisotropic Distribution of SDSS Satellite Galaxies: Planar (Not Polar) Alignment.* ApJ**628**, L101–L104.

Bruderer, C., Read, J. I., Coles, J. P., Leier, D., Falco, E. E., Ferreras, I. & Saha, P. (2016). *Light versus dark in strong-lens galaxies: dark matter haloes that are rounder than their stars.* MNRAS**456**(1), 870–884.

Buchert, T. (1992). *Lagrangian theory of gravitational instability of Friedman-Lemaitre cosmologies and the 'Zel'dovich approximation'.* MNRAS**254**, 729–737.

Bullock, J. S. & Boylan-Kolchin, M. (2017). *Small-Scale Challenges to the ΛCDM Paradigm.* ARA&A**55**(1), 343–387.

Buote, D. A. & Canizares, C. R. (1992). *X-ray constraints on the shape of the dark matter in five Abell clusters.* ApJ**400**, 385–397.

Buote, D. A. & Canizares, C. R. (1996). *X-Ray Constraints on the Intrinsic Shapes and Baryon Fractions of Five Abell Clusters.* ApJ**457**, 565.

Buote, D. A. & Humphrey, P. J. (2012). *Spherically averaging ellipsoidal galaxy clusters in X-ray and Sunyaev-Zel'dovich studies - I. Analytical relations.* MNRAS**420**(2), 1693–1705.

Caminha, G. B., Grillo, C., Rosati, P., Meneghetti, M., Mercurio, A., Ettori, S., Balestra, I., Biviano, A., Umetsu, K., Vanzella, E., Annunziatella, M., Bonamigo, M., Delgado-Correal, C., Girardi, M., Lombardi, M., Nonino, M., Sartoris, B., Tozzi, P., Bartelmann, M., Bradley, L., Caputi, K. I., Coe, D., Ford, H., Fritz, A., Gobat, R., Postman, M., Seitz, S. & Zitrin, A. (2017). *Mass distribution in the core of MACS J1206. Robust modeling from an exceptionally large sample of central multiple images.* A&A**607**, A93.

Caminha, G. B., Rosati, P., Grillo, C., Rosani, G., Caputi, K. I., Meneghetti, M., Mercurio, A., Balestra, I., Bergamini, P., Biviano, A., Nonino, M., Umetsu, K., Vanzella, E., Annunziatella, M., Broadhurst, T., Delgado-Correal, C., Demarco, R., Lombardi, M., Maier, C. & Zitrin, A. (2019). *Strong lensing models of eight CLASH clusters from extensive spectroscopy: accurate total mass reconstructions in the cores.* arXiv e-prints , arXiv:1903.05103.

Carter, D. & Metcalfe, N. (1980). *The morphology of clusters of galaxies.* MNRAS**191**, 325–337.

Cerny, C., Sharon, K., Andrade-Santos, F., Avila, R. J., Bradač, M., Bradley, L. D., Carrasco, D., Coe, D., Czakon, N. G., Dawson, W. A.,

Frye, B. L., Hoag, A., Huang, K.-H., Johnson, T. L., Jones, C., Lam, D., Lovisari, L., Mainali, R., Oesch, P. A., Ogaz, S., Past, M., Paterno-Mahler, R., Peterson, A., Riess, A. G., Rodney, S. A., Ryan, R. E., Salmon, B., Sendra-Server, I., Stark, D. P., Strolger, L.-G., Trenti, M., Umetsu, K., Vulcani, B. & Zitrin, A. (2018). *RELICS: Strong Lens Models for Five Galaxy Clusters from the Reionization Lensing Cluster Survey.* ApJ**859**(2), 159.

Chen, S., Wang, H., Mo, H. J. & Shi, J. (2016). *Alignments of Dark Matter Halos with Large-scale Tidal Fields: Mass and Redshift Dependence.* ApJ**825**, 49.

Chen, Y.-C., Ho, S., Blazek, J., He, S., Mandelbaum, R., Melchior, P. & Singh, S. (2019). *Detecting galaxy-filament alignments in the Sloan Digital Sky Survey III.* MNRAS**485**, 2492–2504.

Cheung, E., Bundy, K., Cappellari, M., Peirani, S., Rujopakarn, W., Westfall, K., Yan, R., Bershady, M., Greene, J. E., Heckman, T. M., Drory, N., Law, D. R., Masters, K. L., Thomas, D., Wake, D. A., Weijmans, A.-M., Rubin, K., Belfiore, F., Vulcani, B., Chen, Y.-M., Zhang, K., Gelfand, J. D., Bizyaev, D., Roman-Lopes, A. & Schneider, D. P. (2016). *Suppressing star formation in quiescent galaxies with supermassive black hole winds.* Nature**533**, 504–508.

Chisari, N., Codis, S., Laigle, C., Dubois, Y., Pichon, C., Devriendt, J., Slyz, A., Miller, L., Gavazzi, R. & Benabed, K. (2015). *Intrinsic alignments of galaxies in the Horizon-AGN cosmological hydrodynamical simulation.* MNRAS**454**, 2736–2753.

Chisari, N., Laigle, C., Codis, S., Dubois, Y., Devriendt, J., Miller, L., Benabed, K., Slyz, A., Gavazzi, R. & Pichon, C. (2016). *Redshift and luminosity evolution of the intrinsic alignments of galaxies in Horizon-AGN.* MNRAS**461**, 2702–2721.

Chisari, N. E., Koukoufilippas, N., Jindal, A., Peirani, S., Beckmann, R. S., Codis, S., Devriendt, J., Miller, L., Dubois, Y., Laigle, C., Slyz, A. & Pichon, C. (2017). *Galaxy-halo alignments in the Horizon-AGN cosmological hydrodynamical simulation.* MNRAS**472**, 1163–1181.

Chisari, N. E., Richardson, M. L. A., Devriendt, J., Dubois, Y., Schneider, A., Le Brun, A. M. C., Beckmann, R. S., Peirani, S., Slyz, A. & Pichon, C. (2018). *The impact of baryons on the matter power spectrum from the Horizon-AGN cosmological hydrodynamical simulation.* MNRAS**480**(3), 3962–3977.

Choi, H., Yi, S. K., Dubois, Y., Kimm, T., Devriendt, J. E. G. & Pichon, C. (2018). *Early-type Galaxy Spin Evolution in the Horizon-AGN Simulation.* ApJ**856**(2), 114.

Cibirka, N., Acebron, A., Zitrin, A., Coe, D., Agulli, I., Andrade-Santos, F., Bradač, M., Frye, B., Livermore, R. C., Mahler, G., Salmon, B., Sharon, K., Trenti, M., Umetsu, K., Avila, R., Bradley, L., Carrasco, D., Cerny, C., Czakon, N. G., Dawson, W. A., Hoag, A. T., Huang, K.-H., Johnson, T. L., Jones, C., Kikuchihara, S., Lam, D., Lovisari, L., Mainali, R., Oesch, P. A., Ogaz, S., Ouchi, M., Past, M., Paterno-Mahler, R., Peterson, A.,

Ryan, R. E., Sendra-Server, I., Stark, D. P., Strait, V., Toft, S. & Vulcani, B. (2018). *RELICS: Strong Lensing Analysis of the Galaxy Clusters Abell S295, Abell 697, MACS J0025.4-1222, and MACS J0159.8-0849.* ApJ**863**(2), 145.

Clampitt, J. & Jain, B. (2016). *Lensing measurements of the ellipticity of luminous red galaxies dark matter haloes.* MNRAS**457**, 4135–4146.

Coe, D., Salmon, B., Bradač, M., Bradley, L. D., Sharon, K., Zitrin, A., Acebron, A., Cerny, C., Cibirka, N., Strait, V., Paterno-Mahler, R., Mahler, G., Avila, R. J., Ogaz, S., Huang, K.-H., Pelliccia, D., Stark, D. P., Mainali, R., Oesch, P. A., Trenti, M., Carrasco, D., Dawson, W. A., Rodney, S. A., Strolger, L.-G., Riess, A. G., Jones, C., Frye, B. L., Czakon, N. G., Umetsu, K., Vulcani, B., Graur, O., Jha, S. W., Graham, M. L., Molino, A., Nonino, M., Hjorth, J., Selsing, J., Christensen, L., Kikuchihara, S., Ouchi, M., Oguri, M., Welch, B., Lemaux, B. C., Andrade-Santos, F., Hoag, A. T., Johnson, T. L., Peterson, A., Past, M., Fox, C., Agulli, I., Livermore, R., Ryan, R. E., Lam, D., Sendra-Server, I., Toft, S., Lovisari, L. & Su, Y. (2019). *RELICS: Reionization Lensing Cluster Survey.* ApJ**884**(1), 85.

Croton, D. J., Farrar, G. R., Norberg, P., Colless, M., Peacock, J. A., Baldry, I. K., Baugh, C. M., Bland-Hawthorn, J., Bridges, T., Cannon, R., Cole, S., Collins, C., Couch, W., Dalton, G., De Propris, R., Driver, S. P., Efstathiou, G., Ellis, R. S., Frenk, C. S., Glazebrook, K., Jackson, C., Lahav, O., Lewis, I., Lumsden, S., Maddox, S., Madgwick, D., Peterson, B. A., Sutherland, W. & Taylor, K. (2005). *The 2dF Galaxy Redshift Survey: luminosity functions by density environment and galaxy type.* MNRAS**356**(3), 1155–1167.

Cypriano, E. S., Sodré, J., Laerte, Kneib, J.-P. & Campusano, L. E. (2004). *Weak-Lensing Mass Distributions for 24 X-Ray Abell Clusters.* ApJ**613**(1), 95–108.

Czakon, N. G., Sayers, J., Mantz, A., Golwala, S. R., Downes, T. P., Koch, P. M., Lin, K.-Y., Molnar, S. M., Moustakas, L. A., Mroczkowski, T., Pierpaoli, E., Shitanishi, J. A., Siegel, S. & Umetsu, K. (2015). *Galaxy Cluster Scaling Relations between Bolocam Sunyaev-Zel'dovich Effect and Chandra X-Ray Measurements.* ApJ**806**, 18.

de Graaff, A., Cai, Y.-C., Heymans, C. & Peacock, J. A. (2019). *Probing the missing baryons with the Sunyaev-Zel'dovich effect from filaments.* A&A**624**, A48.

Despali, G., Giocoli, C., Angulo, R. E., Tormen, G., Sheth, R. K., Baso, G. & Moscardini, L. (2016). *The universality of the virial halo mass function and models for non-universality of other halo definitions.* MNRAS**456**, 2486–2504.

Despali, G., Giocoli, C. & Tormen, G. (2014). *Some like it triaxial: the universality of dark matter halo shapes and their evolution along the cosmic time.* MNRAS**443**, 3208–3217.

Donahue, M., Connor, T., Fogarty, K., Li, Y., Voit, G. M., Postman, M., Koekemoer, A., Moustakas, J., Bradley, L. & Ford, H. (2015). *Ultraviolet Morphology and Unobscured UV Star Formation Rates of CLASH Brightest Cluster*

Galaxies. ApJ**805**, 177.

Donahue, M., Ettori, S., Rasia, E., Sayers, J., Zitrin, A., Meneghetti, M., Voit, G. M., Golwala, S., Czakon, N., Yepes, G., Baldi, A., Koekemoer, A. & Postman, M. (2016). *The Morphologies and Alignments of Gas, Mass, and the Central Galaxies of CLASH Clusters of Galaxies*. ApJ**819**, 36.

Dong, X. C., Lin, W. P., Kang, X., Ocean Wang, Y., Dutton, A. A. & Macciò, A. V. (2014). *The Distribution of Satellites around Central Galaxies in a Cosmological Hydrodynamical Simulation*. ApJ**791**, L33.

Donoso, E., O'Mill, A. & Lambas, D. G. (2006). *Alignment between luminous red galaxies and surrounding structures at z ~0.5*. MNRAS**369**(1), 479–484.

Dubois, Y., Devriendt, J., Slyz, A. & Teyssier, R. (2010). *Jet-regulated cooling catastrophe*. MNRAS**409**, 985–1001.

Dubois, Y., Devriendt, J., Slyz, A. & Teyssier, R. (2012). *Self-regulated growth of supermassive black holes by a dual jet-heating active galactic nucleus feedback mechanism: methods, tests and implications for cosmological simulations*. MNRAS**420**, 2662–2683.

Dubois, Y., Peirani, S., Pichon, C., Devriendt, J., Gavazzi, R., Welker, C. & Volonteri, M. (2016). *The HORIZON-AGN simulation: morphological diversity of galaxies promoted by AGN feedback*. MNRAS**463**, 3948–3964.

Dubois, Y., Pichon, C., Welker, C., Le Borgne, D., Devriendt, J., Laigle, C., Codis, S., Pogosyan, D., Arnouts, S., Benabed, K., Bertin, E., Blaizot, J., Bouchet, F., Cardoso, J.-F., Colombi, S., de Lapparent, V., Desjacques, V., Gavazzi, R., Kassin, S., Kimm, T., McCracken, H., Milliard, B., Peirani, S., Prunet, S., Rouberol, S., Silk, J., Slyz, A., Sousbie, T., Teyssier, R., Tresse, L., Treyer, M., Vibert, D. & Volonteri, M. (2014). *Dancing in the dark: galactic properties trace spin swings along the cosmic web*. MNRAS**444**, 1453–1468.

Durret, F., Tarricq, Y., Márquez, I., Ashkar, H. & Adami, C. (2019). *Link between brightest cluster galaxy properties and large scale extensions of 38 DAFT/FADA and CLASH clusters in the redshift range 0.2 < z < 0.9*. A&A**622**, A78.

Ebeling, H., Qi, J. & Richard, J. (2017). *Fully stripped? The dynamics of dark and luminous matter in the massive cluster collision MACSJ0553.4-3342*. MNRAS**471**(3), 3305–3322.

Evans, A. K. D. & Bridle, S. (2009). *A Detection of Dark Matter Halo Ellipticity using Galaxy Cluster Lensing in the SDSS*. ApJ**695**, 1446–1456.

Evrard, A. E., Mohr, J. J., Fabricant, D. G. & Geller, M. J. (1993). *A Morphology-Cosmology Connection for X-Ray Clusters*. ApJ**419**, L9.

Faltenbacher, A., Jing, Y. P., Li, C., Mao, S., Mo, H. J., Pasquali, A. & van den Bosch, F. C. (2008). *Spatial and Kinematic Alignments between Central and Satellite Halos*. ApJ**675**, 146–155.

Faltenbacher, A., Li, C., Mao, S., van den Bosch, F. C., Yang, X., Jing, Y. P., Pasquali, A. & Mo, H. J. (2007). *Three Different Types of Galaxy Alignment within*

Dark Matter Halos. ApJ**662**, L71–L74.

Flores, R. A., Allgood, B., Kravtsov, A. V., Primack, J. R., Buote, D. A. & Bullock, J. S. (2007). *The shape of galaxy cluster dark matter haloes: systematics of its imprint on cluster gas and comparison to observations.* MNRAS**377**, 883–896.

Foëx, G., Chon, G. & Böhringer, H. (2017). *From the core to the outskirts: structure analysis of three massive galaxy clusters.* A&A**601**, A145.

Frigo, M. & Johnson, S. G. (1998). FFTW: An adaptive software architecture for the FFT. In: *Proc. 1998 IEEE Intl. Conf. Acoustics Speech and Signal Processing*, vol. 3. IEEE.

Frigo, M. & Johnson, S. G. (2005). *The design and implementation of FFTW3.* Proceedings of the IEEE **93**(2), 216–231. Special issue on "Program Generation, Optimization, and Platform Adaptation".

Fukugita, M., Hogan, C. J. & Peebles, P. J. E. (1998). *The Cosmic Baryon Budget.* ApJ**503**(2), 518–530.

Fuller, T. M., West, M. J. & Bridges, T. J. (1999). *Alignments of the Dominant Galaxies in Poor Clusters.* ApJ**519**(1), 22–26.

Gardner, J. P., Mather, J. C., Clampin, M., Doyon, R., Greenhouse, M. A., Hammel, H. B., Hutchings, J. B., Jakobsen, P., Lilly, S. J., Long, K. S., Lunine, J. I., McCaughrean, M. J., Mountain, M., Nella, J., Rieke, G. H., Rieke, M. J., Rix, H.-W., Smith, E. P., Sonneborn, G., Stiavelli, M., Stockman, H. S., Windhorst, R. A. & Wright, G. S. (2006). *The James Webb Space Telescope.* Space Sci. Rev.**123**(4), 485–606.

Gonzalez, A. H., Zabludoff, A. I. & Zaritsky, D. (2005). *Intracluster Light in Nearby Galaxy Clusters: Relationship to the Halos of Brightest Cluster Galaxies.* ApJ**618**(1), 195–213.

Gottlöber, S. & Yepes, G. (2007). *Shape, Spin, and Baryon Fraction of Clusters in the MareNostrum Universe.* ApJ**664**, 117–122.

Greggio, L. & Renzini, A. (1983). *The binary model for type I supernovae - Theoretical rates.* A&A**118**, 217–222.

Habouzit, M., Volonteri, M., Somerville, R. S., Dubois, Y., Peirani, S., Pichon, C. & Devriendt, J. (2019). *The diverse galaxy counts in the environment of high-redshift massive black holes in Horizon-AGN.* MNRAS**489**(1), 1206–1229.

Hahn, O., Carollo, C. M., Porciani, C. & Dekel, A. (2007). *The evolution of dark matter halo properties in clusters, filaments, sheets and voids.* MNRAS**381**, 41–51.

Hao, J., Kubo, J. M., Feldmann, R., Annis, J., Johnston, D. E., Lin, H. & McKay, T. A. (2011). *Intrinsic Alignment of Cluster Galaxies: The Redshift Evolution.* ApJ**740**, 39.

Hashimoto, Y., Böhringer, H., Henry, J. P., Hasinger, G. & Szokoly, G. (2007). *Robust quantitative measures of cluster X-ray morphology, and comparisons between cluster characteristics.* A&A**467**, 485–499.

Hashimoto, Y., Henry, J. P. & Boehringer, H. (2008). *Alignment of galaxies and clusters.* MNRAS**390**, 1562–1568.

Hashimoto, Y., Henry, J. P. & Boehringer, H. (2014). *Multiwavelength investigations of co-evolution of bright cluster galaxies and their host clusters.* MNRAS**440**(1), 588–600.

Hildebrandt, H., Viola, M., Heymans, C., Joudaki, S., Kuijken, K., Blake, C., Erben, T., Joachimi, B., Klaes, D., Miller, L., Morrison, C. B., Nakajima, R., Verdoes Kleijn, G., Amon, A., Choi, A., Covone, G., de Jong, J. T. A., Dvornik, A., Fenech Conti, I., Grado, A., Harnois-Déraps, J., Herbonnet, R., Hoekstra, H., Köhlinger, F., McFarland, J., Mead, A., Merten, J., Napolitano, N., Peacock, J. A., Radovich, M., Schneider, P., Simon, P., Valentijn, E. A., van den Busch, J. L., van Uitert, E. & Van Waerbeke, L. (2017). *KiDS-450: cosmological parameter constraints from tomographic weak gravitational lensing.* MNRAS**465**, 1454–1498.

Hirata, C. & Seljak, U. (2003). *Shear calibration biases in weak-lensing surveys.* MNRAS**343**, 459–480.

Hirata, C. M., Mandelbaum, R., Ishak, M., Seljak, U., Nichol, R., Pimbblet, K. A., Ross, N. P. & Wake, D. (2007). *Intrinsic galaxy alignments from the 2SLAQ and SDSS surveys: luminosity and redshift scalings and implications for weak lensing surveys.* MNRAS**381**, 1197–1218.

Ho, S., Bahcall, N. & Bode, P. (2006). *Cluster Ellipticities as a Cosmological Probe.* ApJ**647**, 8–12.

Hoekstra, H., Yee, H. K. C. & Gladders, M. D. (2004). *Properties of Galaxy Dark Matter Halos from Weak Lensing.* ApJ**606**(1), 67–77.

Hogg, D. W., Blanton, M. R., Brinchmann, J., Eisenstein, D. J., Schlegel, D. J., Gunn, J. E., McKay, T. A., Rix, H.-W., Bahcall, N. A., Brinkmann, J. & Meiksin, A. (2004). *The Dependence on Environment of the Color-Magnitude Relation of Galaxies.* ApJ**601**(1), L29–L32.

Hopkins, P. F., Bahcall, N. A. & Bode, P. (2005). *Cluster Alignments and Ellipticities in ΛCDM Cosmology.* ApJ**618**, 1–15.

Hsu, L.-Y., Ebeling, H. & Richard, J. (2013). *The three-dimensional geometry and merger history of the massive galaxy cluster MACS J0358.8-2955.* MNRAS**429**(1), 833–848.

Huang, H.-J., Mandelbaum, R., Freeman, P. E., Chen, Y.-C., Rozo, E. & Rykoff, E. (2018). *Intrinsic alignment in redMaPPer clusters - II. Radial alignment of satellites towards cluster centres.* MNRAS**474**(4), 4772–4794.

Huang, H.-J., Mandelbaum, R., Freeman, P. E., Chen, Y.-C., Rozo, E., Rykoff, E. & Baxter, E. J. (2016). *Intrinsic alignments in redMaPPer clusters - I. Central galaxy alignments and angular segregation of satellites.* MNRAS**463**, 222–244.

Huff, E. M., Hirata, C. M., Mandelbaum, R., Schlegel, D., Seljak, U. & Lupton, R. H. (2014). *Seeing in the dark - I. Multi-epoch alchemy.* MNRAS**440**, 1296–1321.

Ivezić, Ž., Kahn, S. M., Tyson, J. A., Abel, B., Acosta, E., Allsman, R.,

Alonso, D., AlSayyad, Y., Anderson, S. F., Andrew, J., Angel, J. R. P., Angeli, G. Z., Ansari, R., Antilogus, P., Araujo, C., Armstrong, R., Arndt, K. T., Astier, P., Aubourg, É., Auza, N., Axelrod, T. S., Bard, D. J., Barr, J. D., Barrau, A., Bartlett, J. G., Bauer, A. E., Bauman, B. J., Baumont, S., Bechtol, E., Bechtol, K., Becker, A. C., Becla, J., Beldica, C., Bellavia, S., Bianco, F. B., Biswas, R., Blanc, G., Blazek, J., Bland ford, R. D., Bloom, J. S., Bogart, J., Bond, T. W., Booth, M. T., Borgland, A. W., Borne, K., Bosch, J. F., Boutigny, D., Brackett, C. A., Bradshaw, A., Brand t, W. N., Brown, M. E., Bullock, J. S., Burchat, P., Burke, D. L., Cagnoli, G., Calabrese, D., Callahan, S., Callen, A. L., Carlin, J. L., Carlson, E. L., Chand rasekharan, S., Charles-Emerson, G., Chesley, S., Cheu, E. C., Chiang, H.-F., Chiang, J., Chirino, C., Chow, D., Ciardi, D. R., Claver, C. F., Cohen-Tanugi, J., Cockrum, J. J., Coles, R., Connolly, A. J., Cook, K. H., Cooray, A., Covey, K. R., Cribbs, C., Cui, W., Cutri, R., Daly, P. N., Daniel, S. F., Daruich, F., Daubard, G., Daues, G., Dawson, W., Delgado, F., Dellapenna, A., de Peyster, R., de Val-Borro, M., Digel, S. W., Doherty, P., Dubois, R., Dubois-Felsmann, G. P., Durech, J., Economou, F., Eifler, T., Eracleous, M., Emmons, B. L., Fausti Neto, A., Ferguson, H., Figueroa, E., Fisher-Levine, M., Focke, W., Foss, M. D., Frank, J., Freemon, M. D., Gangler, E., Gawiser, E., Geary, J. C., Gee, P., Geha, M., Gessner, C. J. B., Gibson, R. R., Gilmore, D. K., Glanzman, T., Glick, W., Goldina, T., Goldstein, D. A., Goodenow, I., Graham, M. L., Gressler, W. J., Gris, P., Guy, L. P., Guyonnet, A., Haller, G., Harris, R., Hascall, P. A., Haupt, J., Hernand ez, F., Herrmann, S., Hileman, E., Hoblitt, J., Hodgson, J. A., Hogan, C., Howard, J. D., Huang, D., Huffer, M. E., Ingraham, P., Innes, W. R., Jacoby, S. H., Jain, B., Jammes, F., Jee, M. J., Jenness, T., Jernigan, G., Jevremović, D., Johns, K., Johnson, A. S., Johnson, M. W. G., Jones, R. L., Juramy-Gilles, C., Jurić, M., Kalirai, J. S., Kallivayalil, N. J., Kalmbach, B., Kantor, J. P., Karst, P., Kasliwal, M. M., Kelly, H., Kessler, R., Kinnison, V., Kirkby, D., Knox, L., Kotov, I. V., Krabbendam, V. L., Krughoff, K. S., Kubánek, P., Kuczewski, J., Kulkarni, S., Ku, J., Kurita, N. R., Lage, C. S., Lambert, R., Lange, T., Langton, J. B., Le Guillou, L., Levine, D., Liang, M., Lim, K.-T., Lintott, C. J., Long, K. E., Lopez, M., Lotz, P. J., Lupton, R. H., Lust, N. B., MacArthur, L. A., Mahabal, A., Mand elbaum, R., Markiewicz, T. W., Marsh, D. S., Marshall, P. J., Marshall, S., May, M., McKercher, R., McQueen, M., Meyers, J., Migliore, M., Miller, M., Mills, D. J., Miraval, C., Moeyens, J., Moolekamp, F. E., Monet, D. G., Moniez, M., Monkewitz, S., Montgomery, C., Morrison, C. B., Mueller, F., Muller, G. P., Muñoz Arancibia, F., Neill, D. R., Newbry, S. P., Nief, J.-Y., Nomerotski, A., Nordby, M., O'Connor, P., Oliver, J., Olivier, S. S., Olsen, K., O'Mullane, W., Ortiz, S., Osier, S., Owen, R. E., Pain, R., Pale-

cek, P. E., Parejko, J. K., Parsons, J. B., Pease, N. M., Peterson, J. M., Peterson, J. R., Petravick, D. L., Libby Petrick, M. E., Petry, C. E., Pierfederici, F., Pietrowicz, S., Pike, R., Pinto, P. A., Plante, R., Plate, S., Plutchak, J. P., Price, P. A., Prouza, M., Radeka, V., Rajagopal, J., Rasmussen, A. P., Regnault, N., Reil, K. A., Reiss, D. J., Reuter, M. A., Ridgway, S. T., Riot, V. J., Ritz, S., Robinson, S., Roby, W., Roodman, A., Rosing, W., Roucelle, C., Rumore, M. R., Russo, S., Saha, A., Sassolas, B., Schalk, T. L., Schellart, P., Schindler, R. H., Schmidt, S., Schneider, D. P., Schneider, M. D., Schoening, W., Schumacher, G., Schwamb, M. E., Sebag, J., Selvy, B., Sembroski, G. H., Seppala, L. G., Serio, A., Serrano, E., Shaw, R. A., Shipsey, I., Sick, J., Silvestri, N., Slater, C. T., Smith, J. A., Smith, R. C., Sobhani, S., Soldahl, C., Storrie-Lombardi, L., Stover, E., Strauss, M. A., Street, R. A., Stubbs, C. W., Sullivan, I. S., Sweeney, D., Swinbank, J. D., Szalay, A., Takacs, P., Tether, S. A., Thaler, J. J., Thayer, J. G., Thomas, S., Thornton, A. J., Thukral, V., Tice, J., Trilling, D. E., Turri, M., Van Berg, R., Vanden Berk, D., Vetter, K., Virieux, F., Vucina, T., Wahl, W., Walkowicz, L., Walsh, B., Walter, C. W., Wang, D. L., Wang, S.-Y., Warner, M., Wiecha, O., Willman, B., Winters, S. E., Wittman, D., Wolff, S. C., Wood-Vasey, W. M., Wu, X., Xin, B., Yoachim, P. & Zhan, H. (2019). *LSST: From Science Drivers to Reference Design and Anticipated Data Products.* ApJ**873**(2), 111.

Jedrzejewski, R. I. (1987). *CCD surface photometry of elliptical galaxies. I - Observations, reduction and results.* MNRAS**226**, 747–768.

Jing, Y. P., Mo, H. J., Borner, G. & Fang, L. Z. (1995). *Substructures and density profiles of clusters in models of galaxy formation.* MNRAS**276**(2), 417–431.

Jing, Y. P. & Suto, Y. (2002). *Triaxial Modeling of Halo Density Profiles with High-Resolution N-Body Simulations.* ApJ**574**, 538–553.

Joachimi, B., Mandelbaum, R., Abdalla, F. B. & Bridle, S. L. (2011). *Constraints on intrinsic alignment contamination of weak lensing surveys using the MegaZ-LRG sample.* A&A**527**, A26.

Joachimi, B., Semboloni, E., Hilbert, S., Bett, P. E., Hartlap, J., Hoekstra, H. & Schneider, P. (2013). *Intrinsic galaxy shapes and alignments - II. Modelling the intrinsic alignment contamination of weak lensing surveys.* MNRAS**436**(1), 819–838.

Jones, C., Mandel, E., Schwarz, J., Forman, W., Murray, S. S. & Harnden, J., F. R. (1979). *The structure and evolution of X-ray clusters.* ApJ**234**, L21–L25.

Jullo, E., Kneib, J.-P., Limousin, M., Elíasdóttir, Á., Marshall, P. J. & Verdugo, T. (2007). *A Bayesian approach to strong lensing modelling of galaxy clusters.* New Journal of Physics **9**, 447.

Kaiser, N., Squires, G. & Broadhurst, T. (1995). *A Method for Weak Lensing Observations.* ApJ**449**, 460.

Kang, X., van den Bosch, F. C., Yang, X., Mao, S., Mo, H. J., Li, C. & Jing, Y. P. (2007). *The alignment between satellites and central galaxies: theory versus*

observations. MNRAS**378**, 1531–1542.

Kasun, S. F. & Evrard, A. E. (2005). *Shapes and Alignments of Galaxy Cluster Halos*. ApJ**629**, 781–790.

Kaviraj, S., Laigle, C., Kimm, T., Devriendt, J. E. G., Dubois, Y., Pichon, C., Slyz, A., Chisari, E. & Peirani, S. (2017). *The Horizon-AGN simulation: evolution of galaxy properties over cosmic time*. MNRAS**467**, 4739–4752.

Kawahara, H. (2010). *The Axis Ratio Distribution of X-ray Clusters Observed by XMM-Newton*. ApJ**719**, 1926–1931.

Kawamata, R., Ishigaki, M., Shimasaku, K., Oguri, M., Ouchi, M. & Tanigawa, S. (2018). *Size-Luminosity Relations and UV Luminosity Functions at z = 6-9 Simultaneously Derived from the Complete Hubble Frontier Fields Data*. ApJ**855**(1), 4.

Kawamata, R., Oguri, M., Ishigaki, M., Shimasaku, K. & Ouchi, M. (2016). *Precise Strong Lensing Mass Modeling of Four Hubble Frontier Field Clusters and a Sample of Magnified High-redshift Galaxies*. ApJ**819**(2), 114.

Kazantzidis, S., Kravtsov, A. V., Zentner, A. R., Allgood, B., Nagai, D. & Moore, B. (2004). *The Effect of Gas Cooling on the Shapes of Dark Matter Halos*. ApJ**611**, L73–L76.

Kim, R. S. J., Annis, J., Strauss, M. A. & Lupton, R. H. (2002). The Alignment Effect of Brightest Cluster Galaxies in the SDSS. In: *Tracing Cosmic Evolution with Galaxy Clusters* (Borgani, S., Mezzetti, M. & Valdarnini, R., eds.), vol. 268 of *Astronomical Society of the Pacific Conference Series*.

Koekemoer, A. M., Aussel, H., Calzetti, D., Capak, P., Giavalisco, M., Kneib, J. P., Leauthaud, A., Le Fèvre, O., McCracken, H. J., Massey, R., Mobasher, B., Rhodes, J., Scoville, N. & Shopbell, P. L. (2007). *The COSMOS Survey: Hubble Space Telescope Advanced Camera for Surveys Observations and Data Processing*. ApJS**172**(1), 196–202.

Koester, B. P., McKay, T. A., Annis, J., Wechsler, R. H., Evrard, A., Bleem, L., Becker, M., Johnston, D., Sheldon, E., Nichol, R., Miller, C., Scranton, R., Bahcall, N., Barentine, J., Brewington, H., Brinkmann, J., Harvanek, M., Kleinman, S., Krzesinski, J., Long, D., Nitta, A., Schneider, D. P., Sneddin, S., Voges, W. & York, D. (2007). *A MaxBCG Catalog of 13,823 Galaxy Clusters from the Sloan Digital Sky Survey*. ApJ**660**, 239–255.

Kolokotronis, V., Basilakos, S., Plionis, M. & Georgantopoulos, I. (2001). *Searching for cluster substructure using APM and ROSAT data*. MNRAS**320**, 49–60.

Komatsu, E., Smith, K. M., Dunkley, J., Bennett, C. L., Gold, B., Hinshaw, G., Jarosik, N., Larson, D., Nolta, M. R., Page, L., Spergel, D. N., Halpern, M., Hill, R. S., Kogut, A., Limon, M., Meyer, S. S., Odegard, N., Tucker, G. S., Weiland, J. L., Wollack, E. & Wright, E. L. (2011). *Seven-year Wilkinson Microwave Anisotropy Probe (WMAP) Observations: Cosmological Interpretation*. ApJS**192**, 18.

Krolewski, A., Lee, K.-G., Lukić, Z. & White, M. (2017). *Measuring Alignments between Galaxies and the Cosmic Web at z 2-3 Using IGM Tomography*. ApJ**837**(1),

31.

Lambas, D. G., Groth, E. J. & Peebles, P. J. E. (1988). *Alignments of brightest cluster galaxies with large-scale structures.* AJ**95**, 996–998.

Lau, E. T., Nagai, D., Kravtsov, A. V., Vikhlinin, A. & Zentner, A. R. (2012). *Constraining Cluster Physics with the Shape of X-Ray Clusters: Comparison of Local X-Ray Clusters Versus ΛCDM Clusters.* ApJ**755**, 116.

Le Brun, A. M. C., McCarthy, I. G., Schaye, J. & Ponman, T. J. (2014). *Towards a realistic population of simulated galaxy groups and clusters.* MNRAS**441**, 1270–1290.

Lee, J. (2019). *Revisiting the Galaxy Shape and Spin Alignments with the Large-scale Tidal Field: An Effective Practical Model.* ApJ**872**, 37.

Lee, J. & Suto, Y. (2003). *Modeling Intracluster Gas in Triaxial Dark Halos: An Analytic Approach.* ApJ**585**(1), 151–160.

Leitherer, C., Ortiz Otálvaro, P. A., Bresolin, F., Kudritzki, R.-P., Lo Faro, B., Pauldrach, A. W. A., Pettini, M. & Rix, S. A. (2010). *A Library of Theoretical Ultraviolet Spectra of Massive, Hot Stars for Evolutionary Synthesis.* ApJS**189**, 309–335.

Leitherer, C., Schaerer, D., Goldader, J. D., Delgado, R. M. G., Robert, C., Kune, D. F., de Mello, D. F., Devost, D. & Heckman, T. M. (1999). *Starburst99: Synthesis Models for Galaxies with Active Star Formation.* ApJS**123**, 3–40.

L'Huillier, B., Park, C. & Kim, J. (2017). *Ecology of dark matter haloes - II. Effects of interactions on the alignment of halo pairs.* MNRAS**466**, 4875–4887.

Li, Z., Wang, Y., Yang, X., Chen, X., Xie, L. & Wang, X. (2013). *Brightest Satellite Galaxy Alignment of Sloan Digital Sky Survey Galaxy Groups.* ApJ**768**, 20.

Lin, Y.-T., Hsieh, B.-C., Lin, S.-C., Oguri, M., Chen, K.-F., Tanaka, M., Chiu, I. N., Huang, S., Kodama, T. & Leauthaud, A. (2017). *First Results on the Cluster Galaxy Population from the Subaru Hyper Suprime-Cam Survey. III. Brightest Cluster Galaxies, Stellar Mass Distribution, and Active Galaxies.* ApJ**851**(2), 139.

Lotz, J. M., Koekemoer, A., Coe, D., Grogin, N., Capak, P., Mack, J., Anderson, J., Avila, R., Barker, E. A., Borncamp, D., Brammer, G., Durbin, M., Gunning, H., Hilbert, B., Jenkner, H., Khandrika, H., Levay, Z., Lucas, R. A., MacKenty, J., Ogaz, S., Porterfield, B., Reid, N., Robberto, M., Royle, P., Smith, L. J., Storrie-Lombardi, L. J., Sunnquist, B., Surace, J., Taylor, D. C., Williams, R., Bullock, J., Dickinson, M., Finkelstein, S., Natarajan, P., Richard, J., Robertson, B., Tumlinson, J., Zitrin, A., Flanagan, K., Sembach, K., Soifer, B. T. & Mountain, M. (2017). *The Frontier Fields: Survey Design and Initial Results.* ApJ**837**(1), 97.

Lovisari, L., Forman, W. R., Jones, C., Ettori, S., Andrade-Santos, F., Arnaud, M., Démoclès, J., Pratt, G. W., Randall, S. & Kraft, R. (2017). *X-Ray Morphological Analysis of the Planck ESZ Clusters.* ApJ**846**, 51.

LSST Science Collaboration, Abell, P. A., Allison, J., Anderson, S. F., Andrew, J. R., Angel, J. R. P., Armus, L., Arnett, D., Asztalos, S. J., Axel-

rod, T. S., Bailey, S., Ballantyne, D. R., Bankert, J. R., Barkhouse, W. A., Barr, J. D., Barrientos, L. F., Barth, A. J., Bartlett, J. G., Becker, A. C., Becla, J., Beers, T. C., Bernstein, J. P., Biswas, R., Blanton, M. R., Bloom, J. S., Bochanski, J. J., Boeshaar, P., Borne, K. D., Bradac, M., Brandt, W. N., Bridge, C. R., Brown, M. E., Brunner, R. J., Bullock, J. S., Burgasser, A. J., Burge, J. H., Burke, D. L., Cargile, P. A., Chand rasekharan, S., Chartas, G., Chesley, S. R., Chu, Y.-H., Cinabro, D., Claire, M. W., Claver, C. F., Clowe, D., Connolly, A. J., Cook, K. H., Cooke, J., Cooray, A., Covey, K. R., Culliton, C. S., de Jong, R., de Vries, W. H., Debattista, V. P., Delgado, F., Dell'Antonio, I. P., Dhital, S., Di Stefano, R., Dickinson, M., Dilday, B., Djorgovski, S. G., Dobler, G., Donalek, C., Dubois-Felsmann, G., Durech, J., Eliasdottir, A., Eracleous, M., Eyer, L., Falco, E. E., Fan, X., Fassnacht, C. D., Ferguson, H. C., Fernandez, Y. R., Fields, B. D., Finkbeiner, D., Figueroa, E. E., Fox, D. B., Francke, H., Frank, J. S., Frieman, J., Fromenteau, S., Furqan, M., Galaz, G., Gal-Yam, A., Garnavich, P., Gawiser, E., Geary, J., Gee, P., Gibson, R. R., Gilmore, K., Grace, E. A., Green, R. F., Gressler, W. J., Grillmair, C. J., Habib, S., Haggerty, J. S., Hamuy, M., Harris, A. W., Hawley, S. L., Heavens, A. F., Hebb, L., Henry, T. J., Hileman, E., Hilton, E. J., Hoadley, K., Holberg, J. B., Holman, M. J., Howell, S. B., Infante, L., Ivezic, Z., Jacoby, S. H., Jain, B., R, Jedicke, Jee, M. J., Garrett Jernigan, J., Jha, S. W., Johnston, K. V., Jones, R. L., Juric, M., Kaasalainen, M., Styliani, Kafka, Kahn, S. M., Kaib, N. A., Kalirai, J., Kantor, J., Kasliwal, M. M., Keeton, C. R., Kessler, R., Knezevic, Z., Kowalski, A., Krabbendam, V. L., Krughoff, K. S., Kulkarni, S., Kuhlman, S., Lacy, M., Lepine, S., Liang, M., Lien, A., Lira, P., Long, K. S., Lorenz, S., Lotz, J. M., Lupton, R. H., Lutz, J., Macri, L. M., Mahabal, A. A., Mandelbaum, R., Marshall, P., May, M., McGehee, P. M., Meadows, B. T., Meert, A., Milani, A., Miller, C. J., Miller, M., Mills, D., Minniti, D., Monet, D., Mukadam, A. S., Nakar, E., Neill, D. R., Newman, J. A., Nikolaev, S., Nordby, M., O'Connor, P., Oguri, M., Oliver, J., Olivier, S. S., Olsen, J. K., Olsen, K., Olszewski, E. W., Oluseyi, H., Padilla, N. D., Parker, A., Pepper, J., Peterson, J. R., Petry, C., Pinto, P. A., Pizagno, J. L., Popescu, B., Prsa, A., Radcka, V., Raddick, M. J., Rasmussen, A., Rau, A., Rho, J., Rhoads, J. E., Richards, G. T., Ridgway, S. T., Robertson, B. E., Roskar, R., Saha, A., Sarajedini, A., Scannapieco, E., Schalk, T., Schindler, R., Schmidt, S., Schmidt, S., Schneider, D. P., Schumacher, G., Scranton, R., Sebag, J., Seppala, L. G., Shemmer, O., Simon, J. D., Sivertz, M., Smith, H. A., Allyn Smith, J., Smith, N., Spitz, A. H., Stanford, A., Stassun, K. G., Strader, J., Strauss, M. A., Stubbs, C. W., Sweeney, D. W., Szalay, A., Szkody, P., Takada, M., Thorman, P., Trilling, D. E., Trimble, V., Tyson, A., Van Berg, R., Vand en Berk, D., VanderPlas, J., Verde, L., Vrsnak, B., Walkowicz, L. M., Wand elt, B. D.,

Wang, S., Wang, Y., Warner, M., Wechsler, R. H., West, A. A., Wiecha, O., Williams, B. F., Willman, B., Wittman, D., Wolff, S. C., Wood-Vasey, W. M., Wozniak, P., Young, P., Zentner, A. & Zhan, H. (2009). *LSST Science Book, Version 2.0.* arXiv e-prints , arXiv:0912.0201.

Mahler, G., Sharon, K., Fox, C., Coe, D., Jauzac, M., Strait, V., Edge, A., Acebron, A., Andrade-Santos, F., Avila, R. J., Bradač, M., Bradley, L. D., Carrasco, D., Cerny, C., Cibirka, N., Czakon, N. G., Dawson, W. A., Frye, B. L., Hoag, A. T., Huang, K.-H., Johnson, T. L., Jones, C., Kikuchihara, S., Lam, D., Livermore, R., Lovisari, L., Mainali, R., Ogaz, S., Ouchi, M., Paterno-Mahler, R., Roederer, I. U., Ryan, R. E., Salmon, B., Sendra-Server, I., Stark, D. P., Toft, S., Trenti, M., Umetsu, K., Vulcani, B. & Zitrin, A. (2019). *RELICS: Strong Lensing Analysis of MACS J0417.5-1154 and Predictions for Observing the Magnified High-redshift Universe with JWST.* ApJ**873**(1), 96.

Mandelbaum, R., Hirata, C. M., Ishak, M., Seljak, U. & Brinkmann, J. (2006). *Detection of large-scale intrinsic ellipticity-density correlation from the Sloan Digital Sky Survey and implications for weak lensing surveys.* MNRAS**367**(2), 611–626.

Mandelbaum, R., Miyatake, H., Hamana, T., Oguri, M., Simet, M., Armstrong, R., Bosch, J., Murata, R., Lanusse, F., Leauthaud, A., Coupon, J., More, S., Takada, M., Miyazaki, S., Speagle, J. S., Shirasaki, M., Sifón, C., Huang, S., Nishizawa, A. J., Medezinski, E., Okura, Y., Okabe, N., Czakon, N., Takahashi, R., Coulton, W. R., Hikage, C., Komiyama, Y., Lupton, R. H., Strauss, M. A., Tanaka, M. & Utsumi, Y. (2018). *The first-year shear catalog of the Subaru Hyper Suprime-Cam Subaru Strategic Program Survey.* PASJ**70**, S25.

Mandelbaum, R., Slosar, A., Baldauf, T., Seljak, U., Hirata, C. M., Nakajima, R., Reyes, R. & Smith, R. E. (2013). *Cosmological parameter constraints from galaxy-galaxy lensing and galaxy clustering with the SDSS DR7.* MNRAS**432**, 1544–1575.

Martin, G., Kaviraj, S., Devriendt, J. E. G., Dubois, Y., Pichon, C. & Laigle, C. (2018). *Identifying the progenitors of present-day early-type galaxies in observational surveys: correcting 'progenitor bias' using the Horizon-AGN simulation.* MNRAS**474**(3), 3140–3151.

Matthews, T. A., Morgan, W. W. & Schmidt, M. (1964). *A Discussion of Galaxies Indentified with Radio Sources.* ApJ**140**, 35.

McMillan, S. L. W., Kowalski, M. P. & Ulmer, M. P. (1989). *X-ray morphologies of Abell clusters.* ApJS**70**, 723–730.

Meneghetti, M., Natarajan, P., Coe, D., Contini, E., De Lucia, G., Giocoli, C., Acebron, A., Borgani, S., Bradac, M., Diego, J. M., Hoag, A., Ishigaki, M., Johnson, T. L., Jullo, E., Kawamata, R., Lam, D., Limousin, M., Liesenborgs, J., Oguri, M., Sebesta, K., Sharon, K., Williams, L. L. R. & Zitrin, A. (2017). *The Frontier Fields lens modelling comparison project.* MNRAS**472**(3),

3177–3216.

Miyazaki, S., Komiyama, Y., Kawanomoto, S., Doi, Y., Furusawa, H., Hamana, T., Hayashi, Y., Ikeda, H., Kamata, Y., Karoji, H., Koike, M., Kurakami, T., Miyama, S., Morokuma, T., Nakata, F., Namikawa, K., Nakaya, H., Nariai, K., Obuchi, Y., Oishi, Y., Okada, N., Okura, Y., Tait, P., Takata, T., Tanaka, Y., Tanaka, M., Terai, T., Tomono, D., Uraguchi, F., Usuda, T., Utsumi, Y., Yamada, Y., Yamanoi, H., Aihara, H., Fujimori, H., Mineo, S., Miyatake, H., Oguri, M., Uchida, T., Tanaka, M. M., Yasuda, N., Takada, M., Murayama, H., Nishizawa, A. J., Sugiyama, N., Chiba, M., Futamase, T., Wang, S.-Y., Chen, H.-Y., Ho, P. T. P., Liaw, E. J. Y., Chiu, C.-F., Ho, C.-L., Lai, T.-C., Lee, Y.-C., Jeng, D.-Z., Iwamura, S., Armstrong, R., Bickerton, S., Bosch, J., Gunn, J. E., Lupton, R. H., Loomis, C., Price, P., Smith, S., Strauss, M. A., Turner, E. L., Suzuki, H., Miyazaki, Y., Muramatsu, M., Yamamoto, K., Endo, M., Ezaki, Y., Ito, N., Kawaguchi, N., Sofuku, S., Taniike, T., Akutsu, K., Dojo, N., Kasumi, K., Matsuda, T., Imoto, K., Miwa, Y., Suzuki, M., Takeshi, K. & Yokota, H. (2018a). *Hyper Suprime-Cam: System design and verification of image quality.* PASJ**70**, S1.

Miyazaki, S., Oguri, M., Hamana, T., Shirasaki, M., Koike, M., Komiyama, Y., Umetsu, K., Utsumi, Y., Okabe, N., More, S., Medezinski, E., Lin, Y.-T., Miyatake, H., Murayama, H., Ota, N. & Mitsuishi, I. (2018b). *A large sample of shear-selected clusters from the Hyper Suprime-Cam Subaru Strategic Program S16A Wide field mass maps.* PASJ**70**, S27.

Mohr, J. J., Evrard, A. E., Fabricant, D. G. & Geller, M. J. (1995). *Cosmological Constraints from Observed Cluster X-Ray Morphologies.* ApJ**447**, 8.

Monaghan, J. J. (1992). *Smoothed particle hydrodynamics.* ARA&A**30**, 543–574.

Montes, M. & Trujillo, I. (2019). *Intracluster light: a luminous tracer for dark matter in clusters of galaxies.* MNRAS**482**(2), 2838–2851.

Navarro, J. F., Frenk, C. S. & White, S. D. M. (1997a). *A Universal Density Profile from Hierarchical Clustering.* ApJ**490**, 493–508.

Navarro, J. F., Frenk, C. S. & White, S. D. M. (1997b). *A Universal Density Profile from Hierarchical Clustering.* ApJ**490**, 493–508.

Niederste-Ostholt, M., Strauss, M. A., Dong, F., Koester, B. P. & McKay, T. A. (2010). *Alignment of brightest cluster galaxies with their host clusters.* MNRAS**405**, 2023–2036.

Oemler, A. (1973). *The cluster of galaxies Abell 2670.* ApJ**180**, 11–23.

Oemler, J., A. (1976). *The structure of elliptical and cD galaxies.* ApJ**209**, 693–709.

Oguri, M. (2010). *The Mass Distribution of SDSS J1004+4112 Revisited.* PASJ**62**, 1017–1024.

Oguri, M. (2014). *A cluster finding algorithm based on the multiband identification of red sequence galaxies.* MNRAS**444**(1), 147–161.

Oguri, M., Bayliss, M. B., Dahle, H., Sharon, K., Gladders, M. D., Natarajan, P., Hennawi, J. F. & Koester, B. P. (2012). *Combined strong and weak lensing*

analysis of 28 clusters from the Sloan Giant Arcs Survey. MNRAS**420**, 3213–3239.

Oguri, M., Hennawi, J. F., Gladders, M. D., Dahle, H., Natarajan, P., Dalal, N., Koester, B. P., Sharon, K. & Bayliss, M. (2009). *Subaru Weak Lensing Measurements of Four Strong Lensing Clusters: Are Lensing Clusters Overconcentrated?* ApJ**699**, 1038–1052.

Oguri, M., Lin, Y.-T., Lin, S.-C., Nishizawa, A. J., More, A., More, S., Hsieh, B.-C., Medezinski, E., Miyatake, H., Jian, H.-Y., Lin, L., Takada, M., Okabe, N., Speagle, J. S., Coupon, J., Leauthaud, A., Lupton, R. H., Miyazaki, S., Price, P. A., Tanaka, M., Chiu, I.-N., Komiyama, Y., Okura, Y., Tanaka, M. M. & Usuda, T. (2018). *An optically-selected cluster catalog at redshift $0.1 < z < 1.1$ from the Hyper Suprime-Cam Subaru Strategic Program S16A data.* PASJ**70**, S20.

Oguri, M., Takada, M., Okabe, N. & Smith, G. P. (2010). *Direct measurement of dark matter halo ellipticity from two-dimensional lensing shear maps of 25 massive clusters.* MNRAS**405**, 2215–2230.

Okabe, N., Takada, M., Umetsu, K., Futamase, T. & Smith, G. P. (2010). *LoCuSS: Subaru Weak Lensing Study of 30 Galaxy Clusters.* PASJ**62**, 811–870.

Okumura, T. & Jing, Y. P. (2009). *The Gravitational Shear-Intrinsic Ellipticity Correlation Functions of Luminous Red Galaxies in Observation and in the ΛCDM Model.* ApJ**694**(1), L83–L86.

Omma, H., Binney, J., Bryan, G. & Slyz, A. (2004). *Heating cooling flows with jets.* MNRAS**348**, 1105–1119.

Panko, E., Juszczyk, T. & Flin, P. (2009). *Orientation of Brighter Galaxies in Nearby Galaxy Clusters.* AJ**138**, 1709–1713.

Parekh, V., van der Heyden, K., Ferrari, C., Angus, G. & Holwerda, B. (2015). *Morphology parameters: substructure identification in X-ray galaxy clusters.* A&A**575**, A127.

Paterno-Mahler, R., Sharon, K., Coe, D., Mahler, G., Cerny, C., Johnson, T. L., Schrabback, T., Andrade-Santos, F., Avila, R. J., Bradač, M., Bradley, L. D., Carrasco, D., Czakon, N. G., Dawson, W. A., Frye, B. L., Hoag, A. T., Huang, K.-H., Jones, C., Lam, D., Livermore, R., Lovisari, L., Mainali, R., Oesch, P. A., Ogaz, S., Past, M., Peterson, A., Ryan, R. E., Salmon, B., Sendra-Server, I., Stark, D. P., Umetsu, K., Vulcani, B. & Zitrin, A. (2018). *RELICS: A Strong Lens Model for SPT-CLJ0615-5746, a $z = 0.972$ Cluster.* ApJ**863**(2), 154.

Paz, D. J., Lambas, D. G., Padilla, N. & Merchán, M. (2006). *Shapes of clusters and groups of galaxies: comparison of model predictions with observations.* MNRAS**366**, 1503–1510.

Peirani, S., Dubois, Y., Volonteri, M., Devriendt, J., Bundy, K., Silk, J., Pichon, C., Kaviraj, S., Gavazzi, R. & Habouzit, M. (2017). *Density profile of dark matter haloes and galaxies in the horizon-agn simulation: the impact of AGN feedback.* MNRAS**472**, 2153–2169.

Peirani, S., Mohayaee, R. & de Freitas Pacheco, J. A. (2004). *The angular*

momentum of dark haloes: merger and accretion effects. MNRAS**348**(3), 921–931.

Peirani, S., Sonnenfeld, A., Gavazzi, R., Oguri, M., Dubois, Y., Silk, J., Pichon, C., Devriendt, J. & Kaviraj, S. (2019). *Total density profile of massive early-type galaxies in HORIZON-AGN simulation: impact of AGN feedback and comparison with observations.* MNRAS**483**(4), 4615–4627.

Peter, A. H. G., Rocha, M., Bullock, J. S. & Kaplinghat, M. (2013). *Cosmological simulations with self-interacting dark matter - II. Halo shapes versus observations.* MNRAS**430**, 105–120.

Piras, D., Joachimi, B., Schäfer, B. M., Bonamigo, M., Hilbert, S. & van Uitert, E. (2018). *The mass dependence of dark matter halo alignments with large-scale structure.* MNRAS**474**, 1165–1175.

Plionis, M. (1994). *Position Angles and Alignments of Clusters of Galaxies.* ApJS**95**, 401.

Postman, M., Coe, D., Benítez, N., Bradley, L., Broadhurst, T., Donahue, M., Ford, H., Graur, O., Graves, G., Jouvel, S., Koekemoer, A., Lemze, D., Medezinski, E., Molino, A., Moustakas, L., Ogaz, S., Riess, A., Rodney, S., Rosati, P., Umetsu, K., Zheng, W., Zitrin, A., Bartelmann, M., Bouwens, R., Czakon, N., Golwala, S., Host, O., Infante, L., Jha, S., Jimenez-Teja, Y., Kelson, D., Lahav, O., Lazkoz, R., Maoz, D., McCully, C., Melchior, P., Meneghetti, M., Merten, J., Moustakas, J., Nonino, M., Patel, B., Regös, E., Sayers, J., Seitz, S. & Van der Wel, A. (2012). *The Cluster Lensing and Supernova Survey with Hubble: An Overview.* ApJS**199**(2), 25.

Prunet, S., Pichon, C., Aubert, D., Pogosyan, D., Teyssier, R. & Gottloeber, S. (2008). *Initial Conditions For Large Cosmological Simulations.* ApJS**178**, 179–188.

Reichardt, C. L., Stalder, B., Bleem, L. E., Montroy, T. E., Aird, K. A., Andersson, K., Armstrong, R., Ashby, M. L. N., Bautz, M., Bayliss, M., Bazin, G., Benson, B. A., Brodwin, M., Carlstrom, J. E., Chang, C. L., Cho, H. M., Clocchiatti, A., Crawford, T. M., Crites, A. T., de Haan, T., Desai, S., Dobbs, M. A., Dudley, J. P., Foley, R. J., Forman, W. R., George, E. M., Gladders, M. D., Gonzalez, A. H., Halverson, N. W., Harrington, N. L., High, F. W., Holder, G. P., Holzapfel, W. L., Hoover, S., Hrubes, J. D., Jones, C., Joy, M., Keisler, R., Knox, L., Lee, A. T., Leitch, E. M., Liu, J., Lueker, M., Luong-Van, D., Mantz, A., Marrone, D. P., McDonald, M., McMahon, J. J., Mehl, J., Meyer, S. S., Mocanu, L., Mohr, J. J., Murray, S. S., Natoli, T., Padin, S., Plagge, T., Pryke, C., Rest, A., Ruel, J., Ruhl, J. E., Saliwanchik, B. R., Saro, A., Sayre, J. T., Schaffer, K. K., Shaw, L., Shirokoff, E., Song, J., Spieler, H. G., Staniszewski, Z., Stark, A. A., Story, K., Stubbs, C. W., Šuhada, R., van Engelen, A., Vanderlinde, K., Vieira, J. D., Vikhlinin, A., Williamson, R., Zahn, O. & Zenteno, A. (2013). *Galaxy Clusters Discovered via the Sunyaev-Zel'dovich Effect in the First 720 Square Degrees of the South Pole Telescope Survey.* ApJ**763**, 127.

Reyes, R., Mandelbaum, R., Gunn, J. E., Nakajima, R., Seljak, U. & Hirata,

C. M. (2012). *Optical-to-virial velocity ratios of local disc galaxies from combined kinematics and galaxy-galaxy lensing.* MNRAS**425**, 2610–2640.

Rhee, G. F. R. N. & Katgert, P. (1987). *A study of the elongation of Abell clusters. I - A sample of 37 clusters studied earlier by Binggeli and Struble and Peebles.* A&A**183**, 217–227.

Richard, J., Smith, G. P., Kneib, J.-P., Ellis, R. S., Sanderson, A. J. R., Pei, L., Targett, T. A., Sand, D. J., Swinbank, A. M., Dannerbauer, H., Mazzotta, P., Limousin, M., Egami, E., Jullo, E., Hamilton-Morris, V. & Moran, S. M. (2010). *LoCuSS: first results from strong-lensing analysis of 20 massive galaxy clusters at z = 0.2.* MNRAS**404**, 325–349.

Robertson, A., Harvey, D., Massey, R., Eke, V., McCarthy, I. G., Jauzac, M., Li, B. & Schaye, J. (2019). *Observable tests of self-interacting dark matter in galaxy clusters: cosmological simulations with SIDM and baryons.* MNRAS**488**(3), 3646–3662.

Rusu, C. E., Oguri, M., Minowa, Y., Iye, M., Inada, N., Oya, S., Kayo, I., Hayano, Y., Hattori, M., Saito, Y., Ito, M., Pyo, T.-S., Terada, H., Takami, H. & Watanabe, M. (2016). *Subaru Telescope adaptive optics observations of gravitationally lensed quasars in the Sloan Digital Sky Survey.* MNRAS**458**(1), 2–55.

Salpeter, E. E. (1955). *The Luminosity Function and Stellar Evolution.* ApJ**121**, 161.

Sastry, G. N. (1968). *Clusters Associated with Supergiant Galaxies.* PASP**80**, 252.

Sayers, J., Czakon, N. G., Mantz, A., Golwala, S. R., Ameglio, S., Downes, T. P., Koch, P. M., Lin, K.-Y., Maughan, B. J., Molnar, S. M., Moustakas, L., Mroczkowski, T., Pierpaoli, E., Shitanishi, J. A., Siegel, S., Umetsu, K. & Van der Pyl, N. (2013). *Sunyaev-Zel'dovich-measured Pressure Profiles from the Bolocam X-Ray/SZ Galaxy Cluster Sample.* ApJ**768**, 177.

Schaye, J., Crain, R. A., Bower, R. G., Furlong, M., Schaller, M., Theuns, T., Dalla Vecchia, C., Frenk, C. S., McCarthy, I. G., Helly, J. C., Jenkins, A., Rosas-Guevara, Y. M., White, S. D. M., Baes, M., Booth, C. M., Camps, P., Navarro, J. F., Qu, Y., Rahmati, A., Sawala, T., Thomas, P. A. & Trayford, J. (2015). *The EAGLE project: simulating the evolution and assembly of galaxies and their environments.* MNRAS**446**, 521–554.

Schneider, M. D., Frenk, C. S. & Cole, S. (2012). *The shapes and alignments of dark matter halos.* Journal of Cosmology and Astroparticle Physics, **5**, 030.

Schombert, J. M. (1986). *The Structure of Brightest Cluster Members. I. Surface Photometry.* ApJS**60**, 603.

Schombert, J. M. (1987). *The Structure of Brightest Cluster Members. II. Mergers.* ApJS**64**, 643.

Schombert, J. M. (1988). *The Structure of Brightest Cluster Members. III. cD Envelopes.* ApJ**328**, 475.

Scoville, N., Abraham, R. G., Aussel, H., Barnes, J. E., Benson, A., Blain, A. W., Calzetti, D., Comastri, A., Capak, P., Carilli, C., Carlstrom, J. E., Carollo, C. M., Colbert, J., Daddi, E., Ellis, R. S., Elvis, M., Ewald, S. P., Fall, M., Franceschini, A., Giavalisco, M., Green, W., Griffiths, R. E.,

Guzzo, L., Hasinger, G., Impey, C., Kneib, J. P., Koda, J., Koekemoer, A., Lefevre, O., Lilly, S., Liu, C. T., McCracken, H. J., Massey, R., Mellier, Y., Miyazaki, S., Mobasher, B., Mould, J., Norman, C., Refregier, A., Renzini, A., Rhodes, J., Rich, M., Sanders, D. B., Schiminovich, D., Schinnerer, E., Scodeggio, M., Sheth, K., Shopbell, P. L., Taniguchi, Y., Tyson, N. D., Urry, C. M., Van Waerbeke, L., Vettolani, P., White, S. D. M. & Yan, L. (2007). *COSMOS: Hubble Space Telescope Observations.* ApJS**172**(1), 38–45.

Shakura, N. I. & Sunyaev, R. A. (1973). *Black holes in binary systems. Observational appearance.* A&A**24**, 337–355.

Sheldon, E. S., Cunha, C. E., Mandelbaum, R., Brinkmann, J. & Weaver, B. A. (2012). *Photometric Redshift Probability Distributions for Galaxies in the SDSS DR8.* ApJS**201**, 32.

Shin, T.-h., Clampitt, J., Jain, B., Bernstein, G., Neil, A., Rozo, E. & Rykoff, E. (2018). *The ellipticity of galaxy cluster haloes from satellite galaxies and weak lensing.* MNRAS**475**, 2421–2437.

Singh, S., Mandelbaum, R. & More, S. (2015). *Intrinsic alignments of SDSS-III BOSS LOWZ sample galaxies.* MNRAS**450**(2), 2195–2216.

Snowden, S. L., Mushotzky, R. F., Kuntz, K. D. & Davis, D. S. (2008). *A catalog of galaxy clusters observed by XMM-Newton.* A&A**478**, 615–658.

Song, H. & Lee, J. (2012). *Modeling the Alignment Profile of Satellite Galaxies in Clusters.* ApJ**748**, 98.

Soucail, G., Foëx, G., Pointecouteau, E., Arnaud, M. & Limousin, M. (2015). *The matter distribution in z ˜ 0.5 redshift clusters of galaxies. II. The link between dark and visible matter.* A&A**581**, A31.

Spergel, D. N. & Steinhardt, P. J. (2000). *Observational Evidence for Self-Interacting Cold Dark Matter.* Physical Review Letters **84**, 3760–3763.

Splinter, R. J., Melott, A. L., Linn, A. M., Buck, C. & Tinker, J. (1997). *The Ellipticity and Orientation of Clusters of Galaxies in N-Body Experiments.* ApJ**479**, 632–641.

Springel, V., White, S. D. M. & Hernquist, L. (2004). The shapes of simulated dark matter halos. In: *Dark Matter in Galaxies* (Ryder, S., Pisano, D., Walker, M. & Freeman, K., eds.), vol. 220 of *IAU Symposium.*

Strazzullo, V., Paolillo, M., Longo, G., Puddu, E., Djorgovski, S. G., De Carvalho, R. R. & Gal, R. R. (2005). *Morphology of low-redshift compact galaxy clusters - I. Shapes and radial profiles.* MNRAS**359**, 191–210.

Struble, M. F. (1990). *Position Angle Statistics of the First and Second Brightest Galaxies in a Sample of Coma-like Abell Clusters.* AJ**99**, 743.

Struble, M. F. & Peebles, P. J. E. (1985). *A new application of Binggeli's test for large-scale alignment of clusters of galaxies.* AJ**90**, 582–589.

Sunyaev, R. A. & Zeldovich, I. B. (1980). *The velocity of clusters of galaxies relative to the microwave background - The possibility of its measurement.* MNRAS**190**, 413–420.

Sunyaev, R. A. & Zeldovich, Y. B. (1972). *The Observations of Relic Radiation as a Test of the Nature of X-Ray Radiation from the Clusters of Galaxies.* Comments on Astrophysics and Space Physics **4**, 173.

Suto, D., Kitayama, T., Nishimichi, T., Sasaki, S. & Suto, Y. (2016). *Evolution and statistics of non-sphericity of dark matter halos from cosmological N-body simulation.* PASJ**68**, 97.

Suto, D., Peirani, S., Dubois, Y., Kitayama, T., Nishimichi, T., Sasaki, S. & Suto, Y. (2017). *Projected axis ratios of galaxy clusters in the Horizon-AGN simulation: Impact of baryon physics and comparison with observations.* PASJ**69**, 14.

Suwa, T., Habe, A., Yoshikawa, K. & Okamoto, T. (2003). *Cluster Morphology as a Test of Different Cosmological Models.* ApJ**588**, 7–17.

Tanimura, H., Hinshaw, G., McCarthy, I. G., Van Waerbeke, L., Aghanim, N., Ma, Y.-Z., Mead, A., Hojjati, A. & Tröster, T. (2019). *A search for warm/hot gas filaments between pairs of SDSS Luminous Red Galaxies.* MNRAS**483**(1), 223–234.

Tenneti, A., Mandelbaum, R., Di Matteo, T., Feng, Y. & Khandai, N. (2014). *Galaxy shapes and intrinsic alignments in the MassiveBlack-II simulation.* MNRAS**441**, 470–485.

Tenneti, A., Mandelbaum, R., Di Matteo, T., Kiessling, A. & Khandai, N. (2015). *Galaxy shapes and alignments in the MassiveBlack-II hydrodynamic and dark matter-only simulations.* MNRAS**453**, 469–482.

Teyssier, R. (2002). *Cosmological hydrodynamics with adaptive mesh refinement. A new high resolution code called RAMSES.* A&A**385**, 337–364.

Trevese, D., Cirimele, G. & Flin, P. (1992). *The Orientation of Galaxies in Clusters.* AJ**104**, 935.

Tucker, G. S. & Peterson, J. B. (1988). *The Alignment of Clusters With Brightest Member Galaxies.* AJ**95**, 298.

Tulin, S. & Yu, H.-B. (2018). *Dark matter self-interactions and small scale structure.* Phys. Rep.**730**, 1–57.

Tweed, D., Devriendt, J., Blaizot, J., Colombi, S. & Slyz, A. (2009). *Building merger trees from cosmological N-body simulations. Towards improving galaxy formation models using subhaloes.* A&A**506**, 647–660.

Ueda, S., Kitayama, T., Oguri, M., Komatsu, E., Akahori, T., Iono, D., Izumi, T., Kawabe, R., Kohno, K., Matsuo, H., Ota, N., Suto, Y., Takakuwa, S., Takizawa, M., Tsutsumi, T. & Yoshikawa, K. (2018). *A Cool Core Disturbed: Observational Evidence for the Coexistence of Subsonic Sloshing Gas and Stripped Shock-heated Gas around the Core of RX J1347.5-1145.* ApJ**866**(1), 48.

Umetsu, K., Sereno, M., Tam, S.-I., Chiu, I. N., Fan, Z., Ettori, S., Gruen, D., Okumura, T., Medezinski, E., Donahue, M., Meneghetti, M., Frye, B., Koekemoer, A., Broadhurst, T., Zitrin, A., Balestra, I., Benítez, N., Higuchi, Y., Melchior, P., Mercurio, A., Merten, J., Molino, A., Nonino, M., Postman, M., Rosati, P., Sayers, J. & Seitz, S. (2018). *The Projected Dark and Baryonic Ellipsoidal Structure of 20 CLASH Galaxy Clusters.* ApJ**860**(2), 104.

van Uitert, E., Hoekstra, H., Joachimi, B., Schneider, P., Bland-Hawthorn, J., Choi, A., Erben, T., Heymans, C., Hildebrandt, H., Hopkins, A. M., Klaes, D., Kuijken, K., Nakajima, R., Napolitano, N. R., Schrabback, T., Valentijn, E. & Viola, M. (2017). *Halo ellipticity of GAMA galaxy groups from KiDS weak lensing.* MNRAS**467**, 4131–4149.

Velliscig, M., Cacciato, M., Schaye, J., Crain, R. A., Bower, R. G., van Daalen, M. P., Dalla Vecchia, C., Frenk, C. S., Furlong, M., McCarthy, I. G., Schaller, M. & Theuns, T. (2015a). *The alignment and shape of dark matter, stellar, and hot gas distributions in the EAGLE and cosmo-OWLS simulations.* MNRAS**453**, 721–738.

Velliscig, M., Cacciato, M., Schaye, J., Hoekstra, H., Bower, R. G., Crain, R. A., van Daalen, M. P., Furlong, M., McCarthy, I. G., Schaller, M. & Theuns, T. (2015b). *Intrinsic alignments of galaxies in the EAGLE and cosmo-OWLS simulations.* MNRAS**454**, 3328–3340.

Vikhlinin, A., Kravtsov, A. V., Burenin, R. A., Ebeling, H., Forman, W. R., Hornstrup, A., Jones, C., Murray, S. S., Nagai, D., Quintana, H. & Voevodkin, A. (2009). *Chandra Cluster Cosmology Project III: Cosmological Parameter Constraints.* ApJ**692**, 1060–1074.

Volonteri, M., Dubois, Y., Pichon, C. & Devriendt, J. (2016). *The cosmic evolution of massive black holes in the Horizon-AGN simulation.* MNRAS**460**, 2979–2996.

Wang, Q. D. & Ulmer, M. P. (1997). *X-ray shapes of distant clusters and blue galaxy fractions.* MNRAS**292**, 920.

Wang, Y., Yang, X., Mo, H. J., Li, C., van den Bosch, F. C., Fan, Z. & Chen, X. (2008). *Probing the intrinsic shape and alignment of dark matter haloes using SDSS galaxy groups.* MNRAS**385**, 1511–1522.

Wang, Y. G. & Fan, Z. H. (2004). *The Distribution of Two-dimensional Eccentricity of Sunyaev-Zel'dovich Effect and X-Ray Surface Brightness Profiles.* ApJ**617**(2), 847–859.

Welker, C., Devriendt, J., Dubois, Y., Pichon, C. & Peirani, S. (2014). *Mergers drive spin swings along the cosmic web.* MNRAS**445**, L46–L50.

West, M. J. (1994). *Anisotropic Mergers at High Redshifts - the Formation of CD Galaxies and Powerful Radio Sources.* MNRAS**268**, 79.

West, M. J. & Blakeslee, J. P. (2000). *The Principal Axis of the Virgo Cluster.* ApJ**543**, L27–L30.

West, M. J., de Propris, R., Bremer, M. N. & Phillipps, S. (2017). *Ten billion years of brightest cluster galaxy alignments.* Nature Astronomy **1**, 0157.

West, M. J., Dekel, A. & Oemler, A., Jr. (1989). *Cosmological alignment of clusters of galaxies with their surroundings - A problem for cold dark matter?* ApJ**336**, 46–57.

West, M. J., Jones, C. & Forman, W. (1995). *Substructure: Clues to the Formation of Clusters of Galaxies.* ApJ**451**, L5.

Wittman, D., Foote, D. & Golovich, N. (2019). *Brightest Cluster Galaxy Alignments in Merging Clusters.* ApJ**874**(1), 84.

Xia, Q., Kang, X., Wang, P., Luo, Y., Yang, X., Jing, Y., Wang, H. & Mo, H. (2017). *Halo Intrinsic Alignment: Dependence on Mass, Formation Time, and Environment.* ApJ**848**(1), 22.

Yang, X., van den Bosch, F. C., Mo, H. J., Mao, S., Kang, X., Weinmann, S. M., Guo, Y. & Jing, Y. P. (2006). *The alignment between the distribution of satellites and the orientation of their central galaxy.* MNRAS**369**, 1293–1302.

Yoshida, N., Springel, V., White, S. D. M. & Tormen, G. (2000a). *Collisional Dark Matter and the Structure of Dark Halos.* ApJ**535**, L103–L106.

Yoshida, N., Springel, V., White, S. D. M. & Tormen, G. (2000b). *Weakly Self-interacting Dark Matter and the Structure of Dark Halos.* ApJ**544**(2), L87–L90.

Zel'Dovich, Y. B. (1970). *Reprint of 1970A&A.....5...84Z. Gravitational instability: an approximate theory for large density perturbations.* A&A**500**, 13–18.

Zhang, Y., Yang, X., Faltenbacher, A., Springel, V., Lin, W. & Wang, H. (2009). *The Spin and Orientation of Dark Matter Halos Within Cosmic Filaments.* ApJ**706**(1), 747–761.

Zhang, Y., Yang, X., Wang, H., Wang, L., Mo, H. J. & van den Bosch, F. C. (2013). *Alignments of Galaxies within Cosmic Filaments from SDSS DR7.* ApJ**779**(2), 160.

Zitrin, A., Broadhurst, T., Barkana, R., Rephaeli, Y. & Benítez, N. (2011). *Strong-lensing analysis of a complete sample of 12 MACS clusters at z > 0.5: mass models and Einstein radii.* MNRAS**410**(3), 1939–1956.

Zitrin, A., Fabris, A., Merten, J., Melchior, P., Meneghetti, M., Koekemoer, A., Coe, D., Maturi, M., Bartelmann, M., Postman, M., Umetsu, K., Seidel, G., Sendra, I., Broadhurst, T., Balestra, I., Biviano, A., Grillo, C., Mercurio, A., Nonino, M., Rosati, P., Bradley, L., Carrasco, M., Donahue, M., Ford, H., Frye, B. L. & Moustakas, J. (2015). *Hubble Space Telescope Combined Strong and Weak Lensing Analysis of the CLASH Sample: Mass and Magnification Models and Systematic Uncertainties.* ApJ**801**, 44.

Zitrin, A., Seitz, S., Monna, A., Koekemoer, A. M., Nonino, M., Gruen, D., Balestra, I., Girardi, M., Koppenhoefer, J. & Mercurio, A. (2017). *A Very Large ($\theta_E \gtrsim 40''$) Strong Gravitational Lens Selected with the Sunyaev-Zel'dovich Effect: PLCK G287.0+32.9 (z = 0.38).* ApJ**839**(1), L11.